ENERGY ANISOTROPIES OF PROTON-LIKE ULTRA-HIGH ENERGY COSMIC RAYS

by

Jon Paul Lundquist

A dissertation submitted to the faculty of
The University of Utah
in partial fulfillment of the requirements for the degree of

Doctor of Philosophy

in

Physics

Department of Physics and Astronomy

The University of Utah

December 2017

The University of Utah Graduate School

STATEMENT OF DISSERTATION APPROVAL

The dissertation of **Jon Paul Lundquist**
has been approved by the following supervisory committee members:

Pierre V. Sokolsky ,	Chair(s)	**25 Sept 2017** Date Approved
Douglas R. Bergman ,	Member	**25 Sept 2017** Date Approved
Christoph Boehme ,	Member	**25 Sept 2017** Date Approved
Mikhail E. Raikh ,	Member	**25 Sept 2017** Date Approved
Behrouz Farhang ,	Member	**25 Sept 2017** Date Approved

by **Benjamin Bromley** , Chair/Dean of
the Department/College/School of **Physics and Astronomy**
and by **David B. Kieda** , Dean of The Graduate School.

ABSTRACT

Evidence of a number of interrelated energy dependent intermediate-scale anisotropies have been found in the arrival directions of proton-like ultra-high energy cosmic rays (UHECR) using 7 years of Telescope Array (TA) data. These are found using analysis techniques that have been developed for this dissertation.

Using surface detector (SD) data the reported TA "Hotspot" excess, $E \geq 10^{19.75}$ eV, is found to correspond to a deficit, or "Coldspot," of events for $10^{19.1} \leq E < 10^{19.75}$ eV at 142° R.A., 40° Dec. The global posttrial significance of this Hot/Coldspot event density asymmetry is found to be 5.1σ ($p = 1.56 \times 10^{-7}$).

This Hot/Coldspot feature is the combination, at the same location, of an energy spectrum anisotropy with a 3.74σ significance for energies $E \geq 10^{19.2}$ eV and an energy-distance correlation with a 3.34σ significance for energies $E \geq 10^{19.3}$ eV. The UHECR Hotspot alone is analyzed using a new kernel density estimation (KDE) anisotropy method and found to have a 3.65σ significance ($E \geq 10^{19.75}$ eV). These features suggest energy dependent magnetic deflection of UHECR.

The composition of UHECR primary particles is also studied using a new "Quality Factor Analysis" pattern recognition event selection for fluorescence detectors (FD). This minimizes the energy dependence of the resolution of extensive air shower (EAS) X_{max} depth. Also, a new statistical method making use of all higher moments than the mean $\langle X_{max} \rangle$ shower depth distribution is developed – as there is large disagreement in $\langle X_{max} \rangle$ between all EAS simulation models. There is also an uncertainty, just as large, for any particular model, given uncertainties in particle interaction parameters extrapolated to much higher energies from Large Hadron Collider (LHC) data.

The TA hybrid FD/SD data is found to be statistically compatible with a pure proton composition, though not incompatible with a light mixed composition, for all models of EAS above $E \geq 10^{18.4}$ eV. There is also no statistically significant evidence of the composition getting heavier at the highest energies.

The combined information of a proton-like light composition, and anisotropy evidence suggestive of energy dependent magnetic deflection of UHECR, should be useful for informing future source searches and models of intergalactic propagation through magnetic fields.

“For once I wish to see the entity behind the voice.”

– Vegard Tveitan

CONTENTS

LIST OF FIGURES

ACKNOWLEDGMENTS

First, thanks go to my adviser Prof. Pierre V. Sokolsky for always allowing me to wander and giving great guidance when I got too lost. It would have been hard to choose a better boss. You can finally turn your hammer back around.

Much thanks to Stan Thomas for being my personal therapist and letting me swear out my problems while "getting" what I'm doing before others do.

And of course thanks to my friend Eric Hughes for his ridiculous breadth of knowledge and many years of drunken (me, not him) ruminations on physics, philosophy, and ephemera.

Thanks to Prof. Charlie Jui for all his on-point suggestions.

Thanks to Prof. Gordon Thompson for never taking it easy on me.

There is also the hard work of all the (too many to list) other TA members without which this thesis could not have been done (Dr. Tareq AbuZayyad, Dr. Monica Allen, Prof. John Belz, Prof. Douglas Bergman, Dr. Dmitri Ivanov, Dr. Kazumasa Kawata, Dr. John Matthews, etc...).

Also, thanks to Greg Engh for some editing help.

And last, but most of all, my long-suffering wife Brittni Lundquist, who has been with me the entire way. I honestly don't know what I'd do without you, Bat – probably be a homeless punk.

CHAPTER 1

INTRODUCTION

Even though the discovery of extragalactic cosmic rays, tens of EeV in energy, was over half a century ago there is no confirmed sources of origin and no consensus on their composition. Previous studies have heavily relied on various models where arbitrary analysis parameters must be chosen. The overarching goal of the work in this thesis is to remove these parameters and model dependencies where possible – to let the data lead. This requires the development of some new statistical methods. The second goal is to combine the three modes of ultra-high energy cosmic ray (UHECR) studies (energy, anisotropy, composition) into a single picture.

The search for extragalactic UHECR sources has almost exclusively used pointing direction location as the only relevant piece of data and their deflection by magnetic fields considered a confounding variable. At the intermediate scale, anisotropy searches look for a higher density of events than expected for a uniform distribution of sources (i.e the "on-off" problem). This requires the choice of an energy cut and a choice of scale by binning the sky. These choices are made by referring to deflection models and local supercluster matter models. For small scale anisotropy searches choices of magnetic field models and stellar object catalogs must be made.

Using 7 years of Telescope Array (TA) surface detector (SD), data Chapter 8 introduces a new solution to the so-called "on-off" problem, which removes the arbitrary choice of sky binning size parameter. The other three anisotropy chapters make use of the energy of events in new ways, and make use of magnetic deflection as an additional possible signature of a source (not a confounding variable).

A few searches for "multiplets" of events have attempted to find evidence of UHECR deflected by magnetic fields. These analyses have many arbitrary parameters chosen from certain models of sources and propagation – and no evidence for multiplets has

been found. Chapter 10 is an energy-distance correlation study with no assumptions regarding propagation models and has only the energy threshold as a single parameter. The energy spectrum anisotropy of Chapter 9 is a relative data comparison, so no fitting to the spectrum is done, though a bin size and energy cut must still be chosen.

The Hot/Coldspot analysis of Chapter 11 is another direct search for a source and magnetic deflection of the isotropic background. The idea being UHECR sources are more likely to be where matter is densest in the local universe and that is where there are likely magnetic fields. The result is the discovery of an event density asymmetry with a 5.1σ significance. This appears to be strong evidence of events being deflected away from a source.

The composition chapters use 7 years of hybrid fluorescence detector (FD) and SD reconstructed data. The most reliable composition dependent shower variable is X_{max} which is the depth of the extensive air shower (EAS) particle number maximum. The goal of the pattern recognition event selection of Chapter 12 is to have an efficient removal of events for which X_{max} is not seen by the FD – while being minimally dependent on the Gaisser-Hillas model (Equation 2.16) of EAS development.

The result is the generation of the probability that X_{max} is seen. In Chapter 13 the usual statistical methods are used to compare the data to the various models of EAS showers. The conclusion is that the data behave as a proton-like light composition – though the degree of purity is model dependent. These methods are heavily dependent on the first moment, $\langle X_{max} \rangle$, which is in turn heavily dependent on model assumptions. This is followed by the introduction of a new statistical method, which is fairly model independent, where all higher moments of the X_{max} distribution are compared. The result is that TA hybrid FD/SD data is found to be statistically compatible with a pure proton composition, though not incompatible with a light mixed composition, for all models of EAS above $E \geq 10^{18.4}$ eV.

The combination of a 5.1σ event density asymmetry anisotropy and a composition statistically compatible with pure proton should be useful for informing future source searches and models of UHECR creation, acceleration, and propagation.

PART I

COSMIC RAYS AND TELESCOPE ARRAY

CHAPTER 2

ULTRA-HIGH ENERGY COSMIC RAYS

2.1 Sources and Propagation

2.1.1 Sources

The electromagnetic force inside shock fronts is the most likely cause of the acceleration of charged particles to that status of ultra-high energy cosmic rays (UHECR). One limiting factor in the acceleration of UHECR is the geometrical consideration, for cases similar to Fermi acceleration, that the Larmor radius of the particle cannot exceed the size of its accelerator or it will escape [1]. This limitation relates energy, composition, and source properties into the simple Equation 2.1. Here E_{max} is the maximum attainable energy gain by the particle from the accelerator, $v = \beta c$ is the characteristic velocity of scattering centers (magnetic shock fronts), Z is the nuclei mass number, B is the magnetic field strength, and S is the size of the accelerator.

$$E < \frac{E_{max}}{10^{18} eV} \simeq \frac{1}{2}\beta \times Z \times \frac{B}{\mu G} \times \frac{S}{kpc} \tag{2.1}$$

Figure 2.1 shows the result of this relationship applied to the acceleration of proton primaries by astrophysical objects with shock speeds of $\beta = 1$. Objects above a dotted red line are able to accelerate protons to the energy of that energy spectrum feature. For smaller β the dotted red lines would move parallel toward the upper right corner ($\beta = 1/300$ intercepts at $\sim TT$ and $R{>}cH_0^{-1}$), for heavier primaries they move parallel toward the lower left (10^{20} eV iron intercepts at $\sim 0.5MT$ and $\sim 1Mpc$).

Another limit arises from synchrotron radiation lose inside the sources and energy loss by the Greisen-Zatsepin-Kuzmin (GZK) interaction with the cosmic microwave background (CMB) (discussed in Section 2.1.3). This is shown by the additional dotted gray line in Figure 2.1 – it can be seen that the possible sources are rather limited.

Inside a possible source there are two main acceleration processes that have been suggested. The first is known as "second order Fermi acceleration" which is a statistical accel-

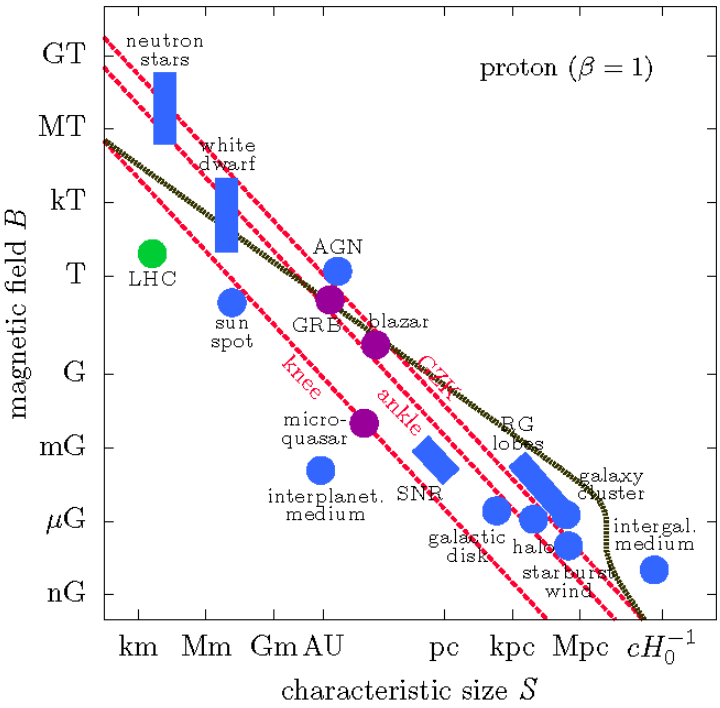

Figure 2.1: A "Hillas plot" that shows the geometric upper limits on ultra-high energy cosmic ray (UHECR) energy that is dependent on the acceleration region size and magnetic field strength. The red dashed lines are the limit of particle energies due to loss of confinement in the acceleration region for relativistic shock front velocities $\beta \simeq 1$ (lower β's move the lines parallel toward the upper right). The relevant limits being the "ankle" to the Greisen-Zatsepin-Kuzmin (GZK) limit – energy sources above these lines can possibly accelerate protons to those energies. The dotted gray line corresponds to another limit that arises from synchrotron radiation loss inside the sources and energy loss by the GZK interaction with the cosmic microwave background (CMB). Adapted from [2], used under CC BY 4.0.

eration process where the charged particles are scattered by magnetized charged particle clouds [3]. This acceleration mechanism has a number of drawbacks; depending on angle of impact the particle may lose energy and the process is very slow. The result is a power law ($E^{-\gamma}$) but with a spectral index, γ, that is too large in magnitude when taking into account energy losses ($\gamma \gtrsim 3$). It is also highly dependent on the local environment of the accelerator.

The second acceleration process is "first order Fermi acceleration" where the charged particles gain energy every time they pass through astrophysical shock fronts regardless of direction [4]. This process also only requires the presence of strong shocks and is

insensitive to details of the local environment. Though first order acceleration has more promise of reaching the correct γ, the energy of particles are still limited by Equation 2.1. The UHECR energy spectrum is discussed further in Section 2.2.2.

2.1.2 Extragalactic Magnetic Field

There has been direct confirmation of galaxy cluster intergalactic magnetic fields of a few μG by Faraday rotation [5]. These are considered to extend on the order of Mpc. From Equation 2.1 the deflection angle from moving a distance S through a uniform magnetic field with a perpendicular component B is shown in Equation 2.2 [6].

$$\delta \approx \frac{S}{R_{larmor}} \simeq 0.5^{\circ} Z \frac{S}{kpc} \frac{B}{\mu G} \frac{10^{20} eV}{E} \tag{2.2}$$

For a random walk through randomly oriented magnetic fields the root mean squared deflection is shown in Equation 2.3 where L_c is the mean coherence length of the magnetic fields [7].

$$\delta_{rms} \approx 0.1^{\circ} Z \frac{B_{rms}}{\mu G} \frac{10^{20} eV}{E} \sqrt{\frac{S}{kpc}} \sqrt{\frac{L_c}{100 pc}} \tag{2.3}$$

Assuming UHECR are deflected away by these fields the result could be large deflections even for protons of the highest energies.

On the other hand, particle confinement in supergalactic plane sheets, with magnetic fields up to 1 μG, have been discussed as a focusing mechanism for events E>50 EeV, and a deflector of background events E<50 EeV [8] [9] [10]. The dilution of particles within the sheet with distance becomes $1/D$ instead of $1/D^2$. It is shown that the Larmor radius is smaller than the thickness of the sheets even for particles of the highest energies. This appears to be consistent with the observations of the Hot/Coldspot in Chapters 9, and 11, where there is an excess of events E>50 EeV and a deficit of events E<50 EeV.

For nonfocusing fields over distances of $\sim$100 Mpc (if there are no supergalactic sheets) there is a large variance of theoretical upper limits to the magnetic field strengths of about 1-10nG [11]. This gives an upper bound deflection for a 10^{20} eV proton of $\delta \lesssim 50^{\circ}$ [6].

2.1.3 Cosmic Microwave Background

The "Greisen-Zatsepin-Kuzmin limit" or "GZK cutoff" was immediately surmised after the discovery of the cosmic microwave background radiation (CMB) [12] [13]. This particle creation (energy loss) mechanism is due to the fact that, when a proton is moving

at relativistic speeds through the low temperature CMB, from the proton's rest frame the photons are at high enough energies for the photo-pion production of Equation 2.4. The creates a sharp suppression of UHECR events greater than about 60 EeV in energy.

$$p + \gamma_{2.7K} \rightarrow \Delta^{+}(1232) \rightarrow \quad p + \pi^{0} \; or \; n + \pi^{+} \tag{2.4}$$

This mechanism was confirmed by the UHECR spectrum observations of the HiRes experiment [14]. Relatively new calculations, done for the interaction of nuclei with CMB, show that proton, and iron, have similar cosmological horizons as shown in Figure 2.2. Intermediate mass nuclei are photodissociated rather quickly and helium as a primary particle is entirely ruled out for distances larger than 10 Mpc [15].

2.1.4 Intragalactic Magnetic Field

Deflection maps for 60 EeV protons are shown for three galactic uniform magnetic field models in Figure 2.3 [17]. The largest deflections are expected by the left model where the average deflection is 5.2° (a quarter of the sky map is less than 2.2°). A 10 EeV proton would be deflected by a factor ∼6 greater than a 60 EeV proton.

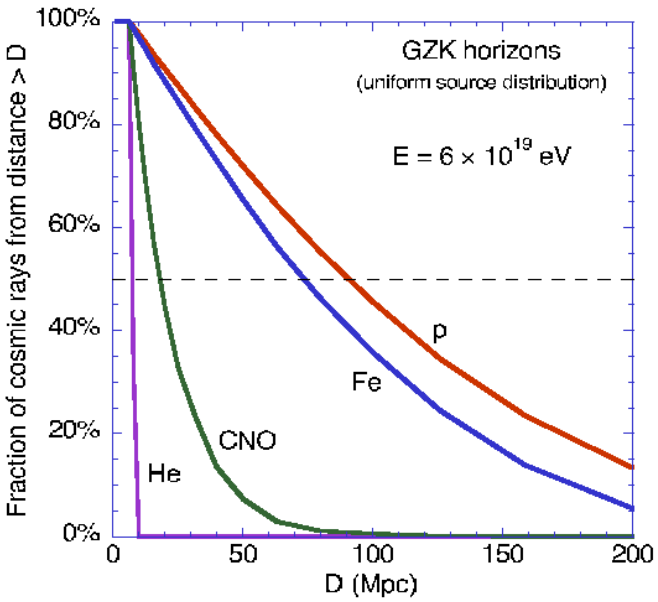

Figure 2.2: Attenuation by the Greisen-Zatsepin-Kuzmin (GZK) interaction of various UHECR primary compositions versus distance. Nuclei of intermediate masses are disintegrated over short propagation distances, D. Taken from [16], used under CC BY 3.0.

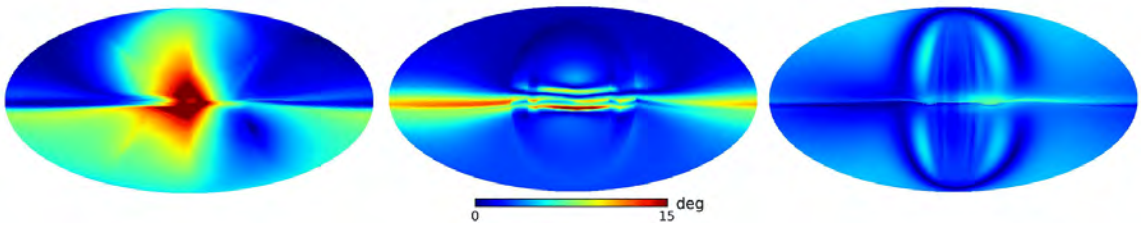

Figure 2.3: Three galactic magnetic field models predicted deflection angles, with propagation transverse to the magnetic field, for 60 EeV proton. For the left model the average deflection is 5.2° and a quarter of the sky is less than 2.2°. A 10 EeV proton would be deflected by a factor ∼6 greater. These are in the Mollweide projection with galactic longitude increasing to the left. Adapted from [17].

The additional contribution from random magnetic fields is expected to be 3 to 30% that of uniform galactic fields [7]. Taking into account the possible range of magnetic deflections by extragalactic and intragalactic fields within the GZK horizon it is reasonable to assume that the most promising avenues of anisotropy studies are on the intermediate to large scales $\delta \gtrsim 20^\circ$, though smaller scale studies cannot be ruled out.

2.2 Phenomenology

2.2.1 Anisotropy

For cosmic ray events just below the energies of interest in this thesis, $E<10^{18.4}$ eV, some evidence for large scale anisotropies associated with our galaxy have been found – such as a report of some galactic plane enhancement by Fly's Eye for $\sim 10^{17.6} \leq E < 10^{18}$ eV [18]. There has been no corroborated statistically significant evidence, by various experiments using a range of techniques (including Telescope Array), for any galactic enhancements associated with the galactic plane or center, nor for a galactic dipole for $E \geq 10^{18}$ eV [19] [20] [21] [22]. It appears that UHECR may not be strongly affected on large scales by galactic fields for events $E \geq 10^{18}$ eV.

Though the signatures of galactic structure have not been present in the pointing directions of extragalactic energy UHECR, that does not mean their sources are not obscured by these fields. No statistically significant evidence ($\sim\sigma>3$) for a correlation between events and extragalactic objects, or a localized excess of events, has stood up to scrutiny or additional data taking for $\sim 10^{18} \leq E < 10^{19.75}$ eV [23] [24] [25]. However, there are new results from the Pierre Auger Observatory (PAO) that suggest there may be a dipole not

associated with galactic structure for events $E \geq 10^{18.9}$ eV [26].

Another relatively new development is the Telescope Array (TA) "Hotspot" excess of events for $E \geq 10^{19.75}$ eV, reported with a 3.4σ significance in the vicinity of Ursa Major $\sim 19^{\circ}$ from the supergalactic plane [27] [28]. This Hotspot contributes events to all the evident anisotropy features studied in this thesis and is discussed in detail in Chapter 8. It has been reported that the most likely source of these events is the closest starburst galaxy M82 only 3.4 Mpc away [29] [30]. This idea may be bolstered by a recent PAO result suggesting a UHECR correlation with starburst galaxies for energies $E \geq 10^{19.59}$ eV [31].

There are also possibly indications of a "Warmspot," that is a not yet significant excess, of events in the vicinity of Centaurus A reported by PAO for $E \geq 10^{19.74}$ eV [32].

2.2.2 Energy Spectrum

The ultra-high energy cosmic ray energy spectrum is a fairly smooth power law function over the entire energy range of interest, $E \geq 10^{18.4}$ eV (and much lower). There is a general consensus on the features of this spectrum and the overall power law function having a "spectral index," $\langle \gamma \rangle \approx 2.7$ [33]. Figure 2.4 shows the energy spectrum, multiplied by a factor of E^{-3} so that smaller features are visible. This includes a spectrum from 3 years of Middle Drum (MD) fluorescence detector (FD) hybrid FD/surface detector (SD) data compared to the HiRes results [34]. These both use the same detectors as the composition analysis in Chapter 13 and the same reconstruction as described in Chapter 5.

Figure 2.4 also compares the recent TA results using the Black Rock (BR) and Long Ridge (LR) FD detectors in stereo to a number of other experiments [33]. This shows very good agreement, within the statistical and systematic uncertainties, for all experiments. The salient features are the "ankle," visible as a dip at $\sim 10^{18.6}$ eV, and the GZK cutoff at $\sim 10^{19.7}$ eV. The power law, $E^{-\gamma}$, was fit to a spectral-index of $\gamma_1 = 3.26$ before the ankle and $\gamma_2 = 2.63$ up to the GZK cutoff. The GZK cutoff behaves approximately as $\gamma_3 \approx 5$.

The "ankle" is generally considered to be the completion of the transition from galactic cosmic rays to extragalactic sources. This transition starts with the leaking of intergalactic particles at the "knee" with $E \simeq 10^{15.5}$ eV and the galactic composition getting heavier beyond this energy [35]. This is either due to the Larmor radius being larger than any uniform fields in the galaxy or the energy cutoff of sources [36]. Some have argued that

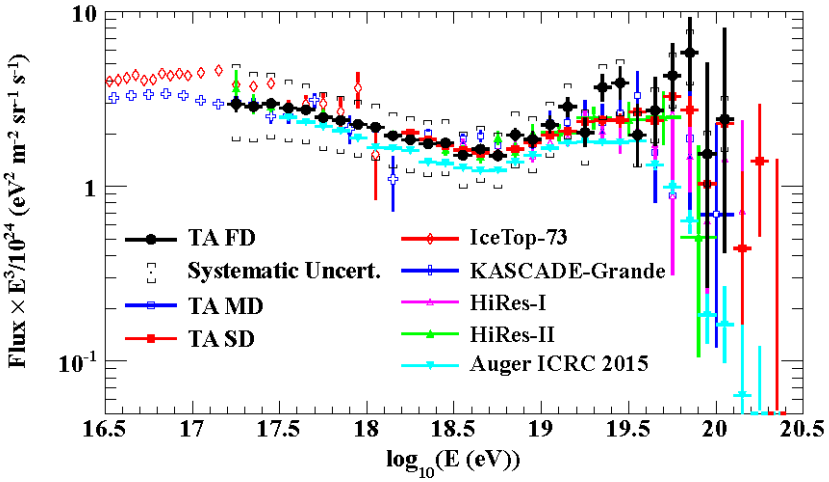

Figure 2.4: UHECR energy spectrum comparisons, between different Telescope Array (TA) detectors, and different experiments. The TA Black Rock (BR) and Long Ridge (LR) FD stereo combined result compared to TA hybrid FD/SD Middle Drum (MD), TA SD mono, IceTop-73, KASCADE-Grande, HiRes, Pierre Auger Observatory (PAO). These show good agreement within the statistical and systematic uncertainties. Adapted from [33].

the cutoff of galactic iron could be all the way up to E = $10^{19.3}$ eV [37].

2.2.3 Composition

At the energies considered here direct ultra-high energy cosmic ray (UHECR) composition measurements are not possible as the fluxes of UHECR are far too small – from 1 particle per km^2 per *year* (E$\geq 10^{18.4}$ eV) to less than one particle per km^2 per *century* (E$\gtrsim 10^{19.3}$ eV). The most common composition studies are done by statistical analysis of the extensive air shower (EAS) particle maximum X_{max} measured by large ground arrays in coincidence with fluorescence detectors. This has been found to be the variable most reliably correlated with composition by simulation.

The latest published results by TA are based on 5 years of hybrid reconstructed FD/SD data, as described in Chapter 5, using the pattern recognition analysis (Binary PRA) event selection described in Section 12.2 [38]. Figure 2.5 shows the elongation rate plot from that paper. The conclusion is a fairly constant proton dominant composition, though with the extreme models it could be heavy enough to be Nitrogen dominated. These results are in agreement with the conclusion of the HiRes experiment [39].

The Pierre Auger Observatory (PAO), on the other hand, reports for their X_{max} studies

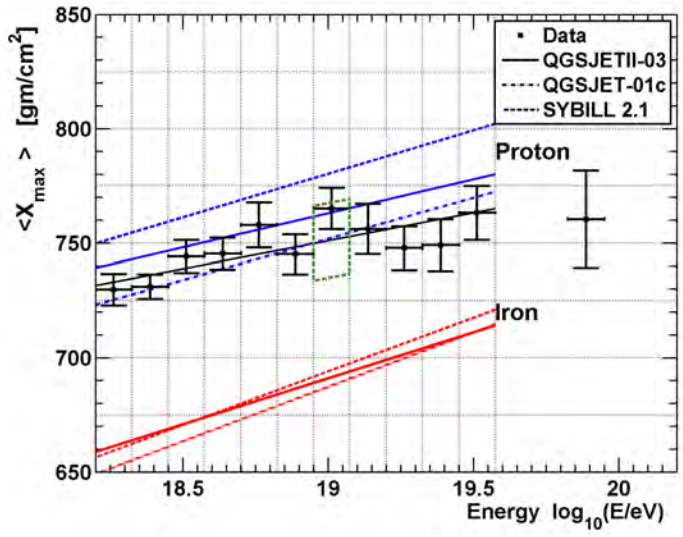

Figure 2.5: $\langle X_{max} \rangle$ elongation plot of the 5-year MD hybrid FD/SD composition result using geometry and pattern recognition analysis (PRA) cuts (described in Chapter 12), for QGSJET-01c, QGSJETII-03, and SIBYLL 2.1 hadronic models. Data are the black points with error bars. The solid black line is a fit to the data. Blue is proton and red is iron. Taken from [38].

a light proton dominated composition that is increasing to a heavier composition. This is mainly based on different treatment of EAS models and the measurements of the next higher moment (the RMS) of the distribution. It is decreasing with energy as expected of heavier compositions [40]. This is discussed further in Chapter 13 where it is shown that while TA data demonstrates similar behavior, it is still compatible with a light composition when compared to simulation. Other PAO analyses, using different methods, show a heavier composition for even lower energies [41].

These disagreements could be a result of a combination of the statistical and unknown systematic uncertainties or a hint of a North-South source composition anisotropy. Though there are disagreements in interpretation, direct comparison of 5 years of TA data from this thesis work (Figure 2.5), and PAO data have been shown to be in good agreement [42].

2.3 Extensive Air Showers

The best way to directly determine the energy, mass, and charge of a particle is to have it pass directly through a controlled magnetic field, emulsion, or scintillator. Since only one primary particle, in the energy range of interest E$\geq 10^{18.4}$ eV, is expected to arrive in

the area of a square kilometer once in a century this is not practicable. Fortunately, we are already in the possession of a scintillator in the form of Earth's atmosphere.

The UHECR primary particle interaction with the atmosphere creates what is called the extensive air shower (EAS) consisting of trillions of secondary particles that spread over tens of square kilometers. EAS are simply described as the superposition of three different components: the hadronic component, the muonic component, and the electromagnetic (EM) cascade. Figure 2.6 shows a pictograph of this process. Observation of the EAS, by "fluorescence" detectors (FD) and surface detectors (SD), give measurements related to the primary particle's energy, composition, and arrival direction.

Only the most common particle interactions and decays are mentioned in the following sections. Many of the less-common processes are taken into account in the simulation of EAS. The EAS simulations are discussed in Section 2.3.6.

2.3.1 Hadronic Component

Equation 2.5a is the unknown initial primary particle ($?_{CR}$) interaction with an atmospheric nucleus, most likely nitrogen or oxygen, that begins the recursive process of Equa-

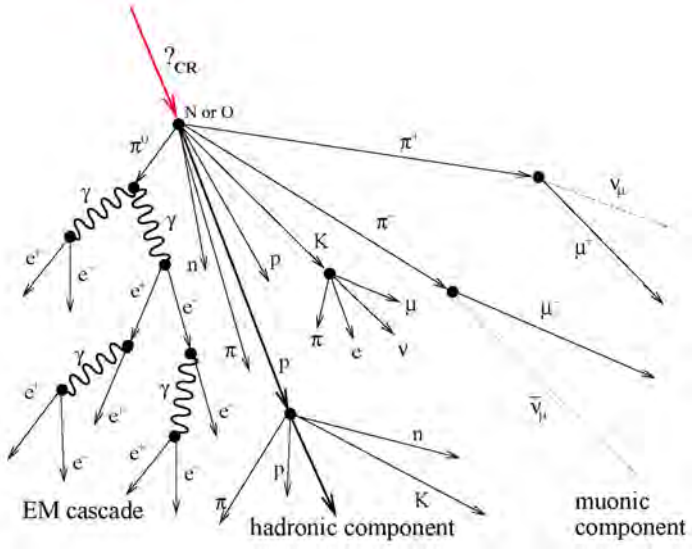

Figure 2.6: Pictograph of the extensive air shower (EAS) initiated by the unknown cosmic ray primary, symbolized by $?_{CR}$, interacting with an atmospheric nuclei. The hadronic component is the EAS core that feeds the other two components by particle decays. The muonic component is weakly interacting and is measured by the SD array. The electromagnetic cascade is a self-regenerative component that scintillates nitrogen in the air, which creates the light observed by the fluorescence detectors (FD). Adapted from [43].

tion 2.5b that feeds the other two components also shown in Figure 2.6. The creation of new particles, by nuclear collision, in the hadronic component continue until the hadrons have only about 1 GeV in energy.

$$?_{CR} \; + \; N \; or \; O \; \rightarrow \; \pi^{\pm,0} + K^{\pm,0} + Hadrons \tag{2.5a}$$

$$Hadron \; + \; N \; or \; O \; \rightarrow \; \pi^{\pm,0} + K^{\pm,0} + Hadrons \tag{2.5b}$$

The kaon decay products of Equation 2.6 feed the two other shower components – the muonic component and the electromagnetic (EM) cascade. Other kaon decay components directly feed only one component.

$$K^{\pm} \rightarrow \pi^{\pm} + \pi^{0} \tag{2.6a}$$

$$K^{-} \rightarrow \pi^{0} + \mu^{-} + \bar{\nu}_{\mu} \tag{2.6b}$$

$$K^{0} \rightarrow \pi^{+} + \pi^{-} + \pi^{0} \tag{2.6c}$$

If the primary particle is a nucleus heavier than a proton, with mass number A, then it will breakup on this initial interaction. The result will be a superposition of a number of smaller energy hadronic showers that each contribute to the muonic component and EM cascade with an energy of E_0 / A.

2.3.2 Muonic Component

In addition to Equation 2.6, the muon component of the shower is also fed by the particle decays shown in Equation 2.7 – π^0 decay is $\sim 10^8$ times slower than the $\pi^{\pm}$ decay that feeds the electromagnetic component.

$$K^{0} \rightarrow \pi^{+} + \pi^{-} \tag{2.7a}$$

$$\pi^{\pm} \rightarrow \mu^{\pm} + \bar{\nu}_{\mu} \tag{2.7b}$$

$$K^{\pm} \; \rightarrow \mu^{\pm} + (\nu_{\mu}, \bar{\nu}_{\mu}) \tag{2.7c}$$

Muons mainly lose energy through ionization as many of them are able to reach the ground before decaying. These can be detected in addition to other particles by the TA SD array.

2.3.3 Electromagnetic Cascade

The electromagnetic (EM) cascade is the largest component of the EAS as the decays that feed it have the largest multiplicity and it is self-sustaining. For each interaction length of atmosphere passed through ($\sim$35 g/cm^2) within the EAS, 1/3 of the hadronic core decays into EM cascade particles. The primary decays from the hadronic core that contribute to the EM cascade are shown in Equation 2.8.

$$K^0 \rightarrow 2\pi^0 \; or \; 3\pi^0 \tag{2.8a}$$

$$\pi^0 \rightarrow 2\gamma \; or \; e^+ + e^- + \gamma \tag{2.8b}$$

Neutral pions decay in about 8.4×10^{-17} seconds into gamma rays each of which initiate another EM cascade. The cascade (Equation 2.9) is the recursion of pair production, Equation 2.9a, to bremsstrahlung, Equation 2.9b, back to pair production. In Equation 2.9 A is a molecule of Nitrogen or Oxygen.

$$\gamma + A \rightarrow e^+ + e^- + A \tag{2.9a}$$

$$e^\pm + A \rightarrow e^\pm + \gamma + A \tag{2.9b}$$

Some lower energy muons, with a Lorentz factor $\gamma<20$, contribute to the EM cascade by decaying before reaching the ground. This decay is shown in Equation 2.10a. Muons can also emit bremsstrahlung radiation shown in Equation 2.10b.

$$\mu^\pm \rightarrow e^\pm + (\nu_e, \bar{\nu}_e) + (\bar{\nu}_\mu, \nu_\mu) \tag{2.10a}$$

$$\mu^\pm + A \rightarrow \mu^\pm + \gamma + A \tag{2.10b}$$

2.3.4 Heitler Model

After a few interaction lengths the EAS shower becomes dominated by the EM component, in both number of particles and energy. At shower maximum, X_{max}, the number of electrons is $\sim$100 times greater than the number of muons for incident protons with E$\geq10^{18.4}$ [44]. The EAS can therefore be well described by the simple heuristic picture of the "Heitler model" shown in Figure 2.7.

The radiation length for bremsstrahlung, $\lambda = -\frac{E}{dE/dx}$, is 37 g/cm^2 in air (standard temperature and pressure) and is approximately the same for pair production ($7/9\lambda$) [44].

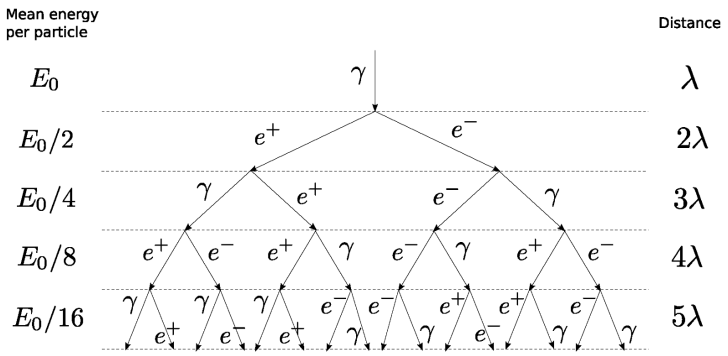

Figure 2.7: The "Heitler branching model" of an EAS electromagnetic (EM) cascade. In a recursive process photons pair produce, and the $e^{\pm}$ emit bremsstrahlung radiation, until the average particle energy is below the critical energy for particle production (E_c = 85 MeV). The average particle energy is halved after each interaction length, $\lambda \approx 35 \mathrm{g/cm^2}$, and the number of particles is doubled. Taken from [43].

This means that in the electromagnetic cascade of Figure 2.7 the number of particles is doubled, and the energy of each particle is halved, every radiation length. This occurs until the average particle energy is below the critical energy, E_c = 85 MeV, when other energy loss mechanisms dominate [44]. For low energy photons the energy loss is through Compton scattering ($\gamma + A \rightarrow \gamma + e^- + A^+$) and the photo-electric effect. The principle energy loss for low energy electrons is by ionization.

At a depth X from the first interaction depth, the number of interactions is $n = X/\lambda$, therefore the number of particles is given by Equation 2.11a. The energy of a particle is given by Equation 2.11b. At the critical energy the number of particles ($N(X)$) is at its maximum and starts to decrease. The shower depth where this occurs is called X_{max} and the number of particles is given by Equation 2.11c.

$$N(X) = 2^{x/\lambda} \tag{2.11a}$$

$$E(X) = E_0/N(X) \tag{2.11b}$$

$$N(X_{max}) = E_0/E_c \tag{2.11c}$$

If the primary cosmic ray particle was a nucleus then there is a superposition of showers where the energy in each subshower is $E_s = E_0/A$. This results in a composition dependent X_{max} value Equation 2.12. This means that by determining the longitudinal

development of the shower, and the initial UHECR energy, we should be able to determine the UHECR primary particle composition.

$$X_{max} = \lambda \frac{\log\left(E_0/(AE_c)\right)}{\log 2} \tag{2.12}$$

Though it is expected that proton to iron primary particles will have different X_{max} there is a large amount of statistical fluctuation and event reconstruction uncertainty. The composition of a single data event cannot be determined. Therefore, statistical methods comparing moments of the entire data distribution to simulated primary compositions must be done. This composition analysis is done in Chapter 13.

2.3.5 Light Emission

2.3.5.1 Cherenkov Radiation

Cherenkov radiation is emitted by the many charged particles in the EAS as they are traveling at speeds greater than that of light in air. The maximum angle of emission for a single particle is shown in Equation 2.13 where $\beta = v/c$ and $n(h)$ is the index of refraction in air which is a function of height. For an ultra-relativistic charged particle in air this angle is about 1.4°.

$$\theta = \cos^{-1}\left(\frac{1}{\beta n}\right) \tag{2.13}$$

Due to the lateral spread of the particles, resulting from many radiation lengths of particle creation and decay, the total angle of emission of Cherenkov photons is wider. The energy dependent number of photons produced by a particle per meter is shown in Equation 2.14a. The number of photons emitted by all particles is shown in Equation 2.14b and the total resulting emission angular distribution is proportional to Equation 2.14c.

$$\frac{dN_{\gamma,e}}{dl} = 4\pi\alpha\left[1 - \left(\frac{E_{min}}{E}\right)^2\right]\int \frac{n-1}{\lambda^2} d\lambda \tag{2.14a}$$

$$\frac{dN_\gamma(X)}{dl} = \int_{E_{min}}^{\infty} N_e(X) f(E, X) \frac{dN_{\gamma,e}}{dl} dE \tag{2.14b}$$

$$\frac{dN_\gamma}{d\Omega} \propto \frac{\exp^{\theta/(0.83E_{min}^{-0.67})}}{\sin\theta} \tag{2.14c}$$

In Equation 2.14 α is the fine structure constant and $E_{min} = m_e c^2/\sqrt{2(n-1)}$ is the energy at which an electron is moving faster than the speed of light in the medium – since ∼90% of the particles are electrons this is a reasonable estimation. $N_e(X)$ is the number of

electrons and f(E,X) is their energy distribution. The result is that most photons are emitted within 6° of the direction of the initiating UHECR though with atmospheric scattering this is as much as 25° [45].

Since Cherenkov radiation is highly direction dependent its contribution to the shower light is estimated and subtracted before calculating the energy of the incident UHECR. Cherenkov radiation cannot simply be blocked by filters as its spectrum overlaps with the nitrogen scintillation light discussed in the following section.

2.3.5.2 Fluorescence

Nitrogen molecules in the atmosphere are excited by the EM cascade. The excited nitrogen molecules release this energy in ∼15 nanoseconds by "scintillation" and emit light isotropically [45]. This is the light, in addition to Cherenkov, that cosmic ray "fluorescence" detectors (FD) such as the Middle Drum (MD) FD at TA measure.

The fluorescence yield, shown in Figure 2.8a, is the number of photons emitted by nitrogen excited by an ionizing particle per unit path length of the particle (Equation 2.15). Around 90% of the ionizing particles are electrons and positrons with energies less than 10^{12} eV. Therefore, the average particle will produce ∼5 photons [45].

$$Y = \frac{4\pi}{N_e}\frac{d^2N_\gamma}{dld\Omega} \tag{2.15}$$

Most of the nitrogen fluorescence is emitted in the Ultraviolet 310-390 nm range as can be seen in Figure 2.8b. The vertical attenuation length at these frequencies is ∼15 km so this light can travel far through the atmosphere.

2.3.6 Simulation

The Monte Carlo (MC) method of simulation uses random draws from probability distributions to emulate the various steps in complex models. MC simulated showers are generated by the CORSIKA (COsmic Ray SImulations for KAscade) program that generates EAS using various available models [46]. High energy secondary particles, E>80 GeV, are modeled by the hadronic models: QGSJET-01c [47], QGSJETII-03 and 04, SYBILL 2.1 [48], and EPOS [49]. At lower energies the FLUKA model is used [50]. The electromagnetic component of the shower is modeled with EGS4 [51]. All branches of particle decays down to the 1% probability level are taken into account along with more

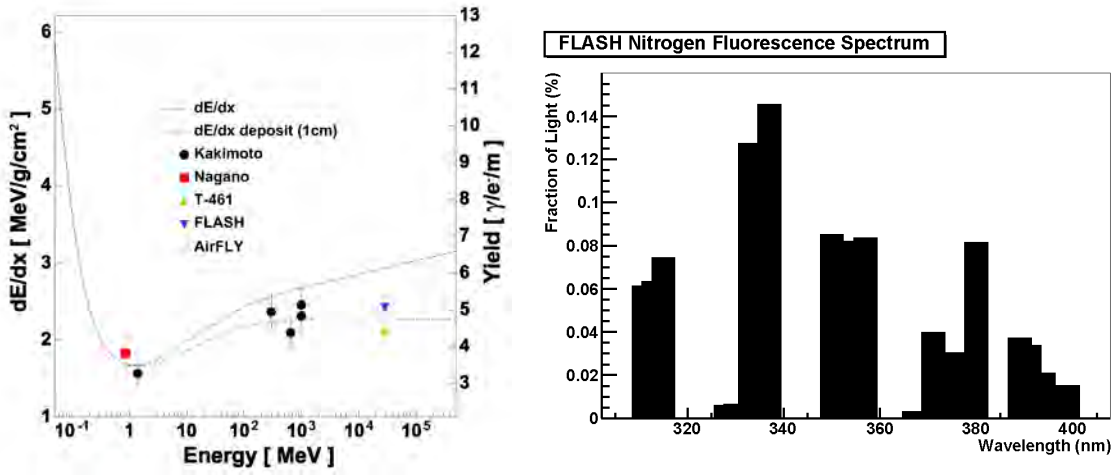

(a) (b)

Figure 2.8: Nitrogen fluorescence spectrum, and yield, measurements. (a) Measurements of the nitrogen fluorescence yield. (b) Measurement of the nitrogen fluorescence spectrum by the FLASH collaboration. Taken from [45].

complicated scattering processes.

CORSIKA simulations of vertical showers for a primary proton and iron with E=10^{15} eV are shown in Figure 2.9. It can be seen that the proton shower has a maximum number of particles deeper than iron. Also, iron appears to be wider at lower slant depths. This is consistent with the conclusion of Section 2.3.3, based on a much simpler model.

2.3.6.1 Thinning and Dethinning

Even with modern supercomputer power it is not possible to create thousands of showers each tracking the trillions of secondary particles in a shower. Data storage is also an issue, with ∼100 GB for each 10^{19} eV event. These issues are circumvented by shower "thinning" where groups of secondary particles, below an energy threshold, close to each other in phase space are reduced to a single particle with a higher weight [52].

The thinning process creates issues with the SD array where the RMS of the simulated signal is artificially inflated due to the clumping of the energy deposit at the ground. This is caused by the missing particles, and weighted particles at large distances from the shower core. This is fixed by the "dethinning" method where the weighted particles are smeared by a Gaussian around its trajectory [52]. Comparisons of the mean and RMS energy deposits, with distance from the shower core show, very good agreement between

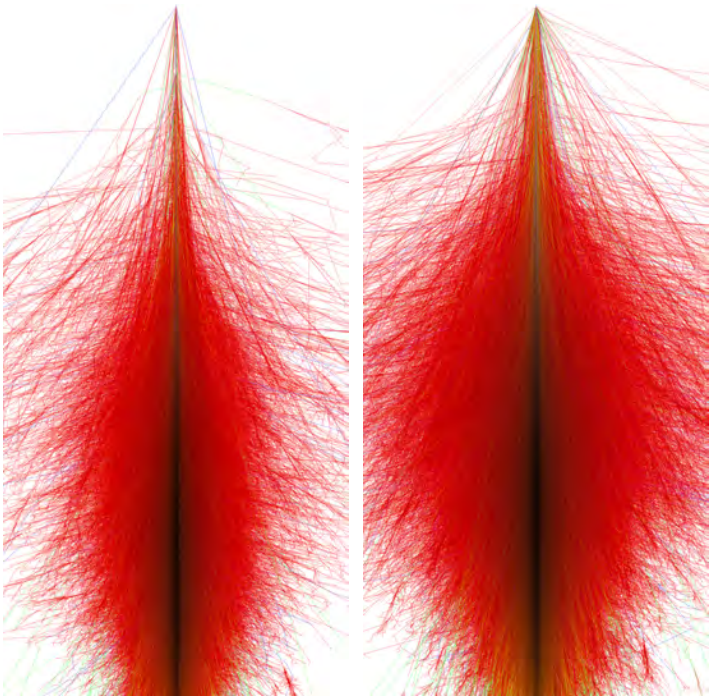

(a) (b)

Figure 2.9: CORSIKA simulated vertical EAS at E = 10^{14} eV. The lines show the particle tracks – red = $e^{\pm}$, γ; green = $\mu^{\pm}$; blue = hadrons. (a) Proton primary. (b) Iron primary. Figures made by Fabian Schmidt and taken from `https://www.ikp.kit.edu/corsika/`

a shower that was not thinned and a dethinned shower [53]. Dethinning allows the use of simulated showers for both FD and SD.

2.3.6.2 Shower Library

A "shower library" of over 16,000 dethinned showers (for each model and composition), with a thinning threshold of E = $10^{-6} \times E_0$, and energies from $10^{16.75}$ to $10^{20.55}$ eV is used by TA.

To save further storage space only the ground incident particles and the Gaisser-Hillas function fit (Equation 2.16) to the longitudinal development of the charged particles is kept (a thinned shower is ∼100 MB). The Gaisser-Hillas function parametrizes the number of charged particles, N, versus slant depth (from the top of the atmosphere in g/cm^2), X. λ is a scaling constant, X_0 is the depth of first interaction, and X_{max} is the depth where the maximum number of particles, N_{max}, occurs. Slant depth is the line integral of density and measures the amount of material passed through.

$$N(X) = N_{max} \left(\frac{X - X_0}{X_{max} - x_0} \right)^{\frac{X_{max} - X_0}{\lambda}} \exp\left(\frac{X_{max} - X}{\lambda} \right) \tag{2.16}$$

These shower library sets are made into very large sets of events by resampling and the detector response is simulated as discussed in Chapter 3.3.

CHAPTER 3

TELESCOPE ARRAY

The Telescope Array (TA) experiment began in 2003 and is the largest ultra-high energy cosmic ray (UHECR) detector in the northern hemisphere. It is located in the desert near Delta, Utah at 39.3° N. -112.9° W. which is 1382 m above sea level. It consists of three fluorescence detectors (FD) at positions along a 35 km triangle, with 38 mirrors total, facing in over an array of 507 surface detectors (SD) with a spacing of 1.2 km between them. The configuration of the FD and SD at TA is shown in Figure 3.1.

The resulting array has a total detecting area of $\sim$700 km^2 (roughly 3 times the size of Chicago). The SD array is operational 24 hours a day, every day, while the FD can only

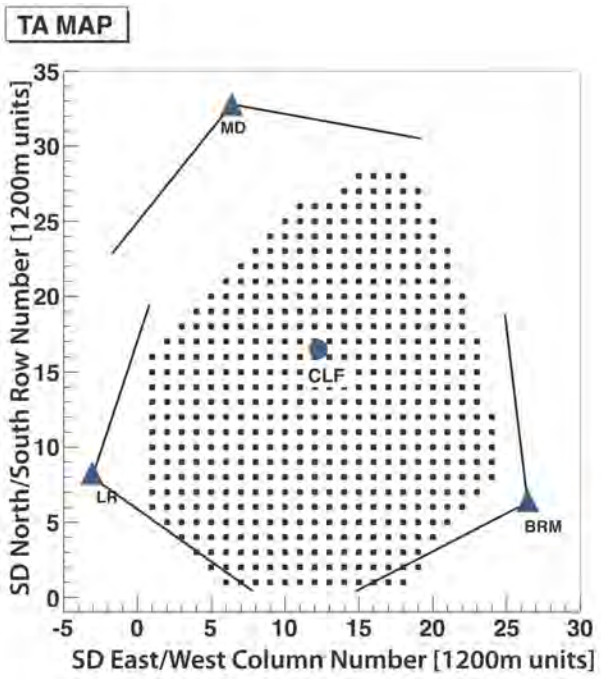

Figure 3.1: Telescope Array (TA) surface detector (SD) and fluorescence detector (FD) configuration. Blue triangles are the three FD sites. The top triangle labeled MD is the site used in this thesis. The black squares are the SD. The central circle is the Central Laser Facility (CLF). Taken from [34].

be run on clear moonless nights. Both detectors use the Earth's atmosphere as part of a calorimeter used to measure the energy of UHECR. The efficiency (probability that an incident particle will be detected by the SD array) is a constant 100% for incident particles with energies above $\sim 10^{19}$ eV – the acceptance begins to rise quickly above $\sim 10^{18}$ eV.

3.1 Surface Detector (SD)

The TA SD is used for the anisotropy analysis in Part 2 of this thesis due to the large statistics and accurate pointing direction reconstruction. TA SDs are composed of two 3 m^2 layers of 1.2 cm thick plastic scintillator. As ionizing particles pass through the detector photons emitted are collected by wavelength shifting fibers in the scintillator focused towards the photomultiplier tube in each layer. Very detailed information on SD electronics can be found in [54].

Two fits are done to reconstruct the pointing direction and energy of each cosmic ray event and are described in Chapter 4. To reconstruct the pointing direction and core position within the array the trigger times of the detectors are fitted to the modified Linsley shower shape function [55]. The details of this fit are described in Section 4.1.3.

The event energy is reconstructed by fitting the pulse heights of triggered detectors to a lateral distribution with the same form used by the AGASA experiment [56]. The resulting fit is used to calculate S(800) (the density of shower particles at a lateral distance of 800 m from the core position). Energy is then estimated by a 2d histogram of S(800) and zenith angle determined from a large set of Monte Carlo (MC) simulations described in Section 2.3.6. The result is recalibrated as there are direct calorimetric measurements by fluorescence detectors described below. The energy reconstruction is further described in Section 4.1.4.

3.1.1 SD Calibration

The full description of both the SD calibration and electronics are available in [53] for which the following is a short summary. Calibration finds the correspondence between the counter Flash Analog-to-Digital Converter (FADC) output from the PMTs and the particle energy deposition. The SD detectors are calibrated by atmospheric muons. By simulation it is found that a vertical muon of 300 MeV has the minimum ionization en-

ergy when interacting with an SD. The most probable energy deposition for a 300 MeV muon is 2.05 MeV which defines the vertical-equivalent muon (VEM) unit of energy – 1 VEM≡2.05 MeV. Single atmospheric background muons pass through each detector at a count rate of ∼700 Hz. This signal dominates the histogram of pulse heights, when the detector is triggered by both layers, collected in 10 minute intervals. The scintillators are calibrated to the pulse height of a minimum ionizing particle (MIP) with ∼1% accuracy using these 10 minute histograms (taking into account the low level electronic noise called the "pedestal") [53] .

The SD array as a whole is triggered when least three adjacent counters have pulse heights over 3 MIP within 8 μs of each other. A 50 MHz flash ADC readout system saves the signals for all counters in the array with more than 0.3 MIP [53].

3.2 Fluorescence Detector (FD)

The fluorescence detector (FD) site used for the hybrid FD/SD composition analysis in Part 3 of this thesis is the northern most site located near Middle Drum (MD) mountain shown in Figure 3.1. It was constructed with 14 refurbished telescopes taken from the HiRes-1 site of the previous High-Resolution Fly's Eye (HiRes) experiment and is placed ∼10 km from the northern SD array boundary. The use of these telescopes allows a direct comparison between Telescope Array and HiRes by sharing of their energy scale. The southern sites (Black Rock (BR) and Longridge (LR)) each consist of 12 new telescopes built by the Japanese TA collaborators and are not used here.

Each of the 14 telescopes has a 5.1 m^2 spherical mirror composed of four segments in a cloverleaf shape. These mirrors image the luminous air showers onto a camera with a cluster of 256 photomultiplier tubes (PMT). The telescopes are paired so that seven of them view 3°-17° in elevation, and seven view 17°-31°, in the same azimuthal directions. The triggering (and calibration) of an FD is more complicated than the SD array and involves adjacent subclusters of a camera triggering the telescope that can in turn trigger adjacent telescopes. As of 2010 when a detector is triggered data is also recorded by the SD array using the hybrid trigger for use in hybrid event reconstruction, for earlier events simple time matching is done to find events coincident with the FD and SD. Details of the FD electronics, triggering, and calibration can be found in [57].

The FD image the light emitted (mainly) by Nitrogen due the passage of charged UHECR shower particles (so actually "luminescence" or "scintillation" detectors as "fluorescence" usually refers to reemission of light). This is used to measure the size of secondary shower particles as a function of slant depth (a measure of the amount of material passed through or the line integral of air density). The slant depth at maximum shower size, called X_{max}, is used in statistical tests as a measure of chemical composition of UHECR. This fluorescence measurement also gives a calorimetric measure of shower energy that is used to recalibrate SD event energies.

The FD data used in this thesis analysis is reconstructed using a hybrid FD/SD method. First, data coincident between the FD and SD's are reconstructed by the SD method mentioned above in Section 3.1 and further described in Chapter 4. The resulting shower core location along with the events SD trigger times are used along with FD PMT tube times to constrain the events geometry. The events PMT tube signals are used to calculate X_{max} and the incident particle energy using an inverse Monte Carlo (MC) method. The hybrid reconstruction method is further described in Chapter 5.

3.2.1 FD Calibration

The full description of both the Middle Drum (MD) site FD calibration and electronics are available in [57] for which the following is a short summary. The estimation of the energy of events by FD is done in three steps: the digitized Charge to Digital Converter (QDC) counts from the photomultiplier tubes (PMT) are converted to the number of incident photons, then the number of photons emitted by the shower is calculated by accounting for transmission through the atmosphere, and lastly the number of charged particles is calculated from the total number of photons (the "fluorescence yield") [57]. The fluorescence yield is discussed in Section 2.3.5.2 as it is a function of the shower itself and not the detector.

Once the atmosphere is characterized with a known source the detector response is known. This allows the calculation of the number of photons emitted by the source EAS. Given the known fluorescence yield this allows determination of the energy of the shower and where the number of particles reach their maximum (X_{max}). Energy and X_{max} reconstruction are discussed further in Chapter 5 [57].

3.2.1.1 Photometric Calibration

Converting the PMT QDC signal to number of photons is done mainly by the Roving Xenon Flasher (RXF). This is placed at the center of each FD mirror twice a month and has a known signal and this is compared to the QDC output. Real time tracking of the ratio of photons to QDC signal (the PMT gain) is also done using the Ultra Violet Light Emitting Diode (UVLED), placed in the center of the mirrors, that has a known photon output dependent on temperature. This is run before, during, and after each night of data taking.

3.2.1.2 Atmospheric Calibration

Atmospheric calibration is necessary for calculating how the shower develops, as the shower light propagation to the detector depends on atmospheric conditions, and must be modeled. This involves estimating the density of air versus elevation, the amount of aerosols (dust) in the air, and monitoring the weather for hazy conditions or clouds within the field-of-view (FOV).

The atmospheric profile is the atmospheric pressure versus elevation above sea level. Previously, in [57], and [38], the atmospheric profile was taken daily from radiosonde data from the National Weather Service site near Delta, Utah combined with the US 1976 atmospheric pressure model for the highest altitudes [58]. In the analysis of [59], that was done for this thesis and expanded upon in Chapter 13, the Global Data Assimilation System (GDAS) atmospheric profile is used. This is used by the National Center for Environmental Prediction (NCEP) Global Forecast System (GFS) and is updated every three hours (instead of once a day) and is a more accurate estimation of the atmospheric profile [60].

Aerosol scattering of light can vary widely each night of running the FD. The amount of aerosols, and their distribution in the air, is estimated by the LIght Detection And Ranging (LIDAR) technique using yttrium aluminum garnet (YAG) lasers with a known photon output. A vertical YAG is placed at the CLF (Figure 3.1) roughly equidistant from all three FD and a second YAG laser is pointed diagonally over the array. This allows accurate estimation of the Vertical Aerosol Optical Depth (VAOD) that defines the transmission factor of light through the aerosol load in the atmosphere ($T_{aerosol} = e^{-\tau}$) [57]. A yearly

average constant value of τ = 0.04 was used for this analysis and the nightly variation was shown to cause a $\sim$3% uncertainty in the final energy determination after weather monitoring cuts to the data [57].

The weather is monitored by collaboration members at the site of each FD every 40 minutes during a run of the detector. Times with significant clouds are removed from the data set. This improves estimation of the detector aperture, energy and X_{max} resolutions.

3.3 Simulation

For each "shower library" set of over 16,000 dethinned showers, simulated as described in Section 2.3.6, a set of over a million simulated events is created by resampling. Each shower library event was created with an energy and a zenith angle – more shower events are made by assigning a random shower library event a random shower core location, trigger time, and azimuthal angle.

The shower library is sampled from so that the larger resampled set follows the energy distribution piece-wise power law that was fitted to HiRes data shown in Figure 2.4 [14] [53]. The energy distribution spectral indices, $E^{-\gamma}$, are – γ=3.25 for $10^{18.4} \leq E < 10^{18.65}$ eV, γ=2.81 for $10^{18.65} \leq E < 10^{18.75}$ eV, and γ=5.1 for $E \geq 10^{19.75}$ eV.

3.3.1 SD Response

Surface detector (SD) response simulation is discussed in detail in [53] for which this is a short summary. The zenith angle distribution assigned to MC shower library events is $g(\theta) = \sin(\theta)\cos(\theta)$ due to the geometry of a uniform spherical pointing direction distribution sampled by a flat detector. $\sin(\theta)$ is a spherically isotropic distribution and $\cos(\theta)$ is the projection of the distribution on the flat SD array. The MC azimuthal angle distribution is uniform – at ultra-high energies little bias results from assuming there is no preferred orientation with respect to cardinal directions of the Earth's sphere due to magnetic field effects. The MC event core impact position distribution is a uniform circle 25 km in radius centered at the CLF. The trigger time is a uniform distribution within the total run time of the detector [53].

The SD response is simulated by the GEometry ANd Tracking (GEANT4) program [61]. The GEANT4 simulation takes as input the dethinned CORSIKA shower simulated par-

ticles at ground level (Section 2.3.6) and outputs a simulated FADC output and timing for each SD. This takes into account the SD geometry, composition, and temperature at the simulated time. These simulated FADC outputs are used to reconstruct the simulated shower in the same manner as data as described in Chapter 4 [53].

3.3.2 FD Response

Fluorescence detector (FD) response simulation is discussed in detail in [57] for which this is a short summary. For the hybrid FD/SD reconstruction used in this thesis the geometry distributions of the showers are limited by the SD geometry and the fact that the FD only run on moonless nights with good weather. So the first step is to take the large set of MC simulated through the SD response and remove those MC events that fall outside the FD run times [57].

Next, the number of charged particles at all slant depths is found by the MC events Gaisser-Hillas (Equation 2.16) fit and this is converted to fluorescence photons as described in Section 2.3.5.2.

3.3.2.1 Atmospheric Scattering

The fluorescence photons, during their propagation towards the FD, are affected by Rayleigh scattering, aerosol scattering, and ozone absorption. Rayleigh molecular scattering depends on atmospheric density. Mie aerosol scattering is dependent on density and size of the non-atmospheric matter suspended in the air (dust, pollution, moisture, etc.). Ozone absorption is the attenuation of UV light due to ozone. The effects of these processes on fluorescence light propagation are discussed in detail in [57].

Taking into account these effects the amount of light produced in a shower segment is tracked back to the amount of light that reaches the FD mirrors. Then the calibrated quantum efficiency of the PMTs converts photons into photoelectrons. Then the mirror reflectivity and PMT filter UV transmission is applied to determine whether a photoelectron contributes to the signal. Then the photoelectrons are ray-traced (treating them like photons again) to find which PMT (if any) they hit. This order of simulation saves an order of magnitude processing time [57].

Then the number of photoelectrons hitting each PMT is converted by electronics simulation into Charge to Digital Converter (QDC) counts, from the photomultiplier tubes

(PMT), and tube timing information from Time to Digital Converters (TDC). These simulated detector outputs are then used to reconstruct the simulated shower in the same manner as data as described in Chapter 5 [57].

CHAPTER 4

SD RECONSTRUCTION AND DATA

For the anisotropy analyses in Part 2, Telescope Array (TA) surface detector (SD) data is reconstructed using the event reconstruction that was used for the first TA "Hotspot" analysis [27], and the updated Hotspot analysis [28]. SD data is used for ultra-high energy cosmic ray (UHECR) anisotropy analyses, rather than fluorescence detector (FD) hybrid FD/SD data, due to a more uniform sky exposure and the much higher number of reconstructed events. The hybrid FD/SD reconstruction, based in part on the mono SD reconstruction described in this chapter, is used for the composition analysis of Part 3, and is described in Chapter 5.

A description of the TA SD electronics can be found in [54]. The full description of both SD electronics and data event reconstruction are available in [53] for which this is a summary. There is a difference in the reconstruction used here, from that in [53], because of the treatment of the Linsley function (Equation 4.8) as it is dependent on the zenith angle and is not a free fitting parameter.

4.1 Event Reconstruction

4.1.1 Definitions

The coordinate system for shower reconstruction is centered at the Central Laser Facility (CLF) (Figure 3.1). The SD plane (the ground) is the x-y plane.

Figure 4.1 shows the extensive air shower (EAS) geometry variables required to reconstruct an events zenith and azimuth angles (these are needed to find where in the sky an event arrived from). Zenith angle, θ, is the angle between the z-axis (perpendicular to the SD plane) and the event arrival direction unit vector is $\hat{\mathbf{n}}(\theta, \phi)$. Azimuthal angle, ϕ, is the angle counter-clockwise from cardinal east (x-axis) of the SD plane projection of $\hat{\mathbf{n}}$.

The time, T_0, is when the shower core crosses the SD plane. $\vec{\mathbf{R}}_{SD} = x\hat{\mathbf{i}} + y\hat{\mathbf{j}}$ is an SD plane vector of the position where the shower crosses the SD plane, at T_0, whose origin is

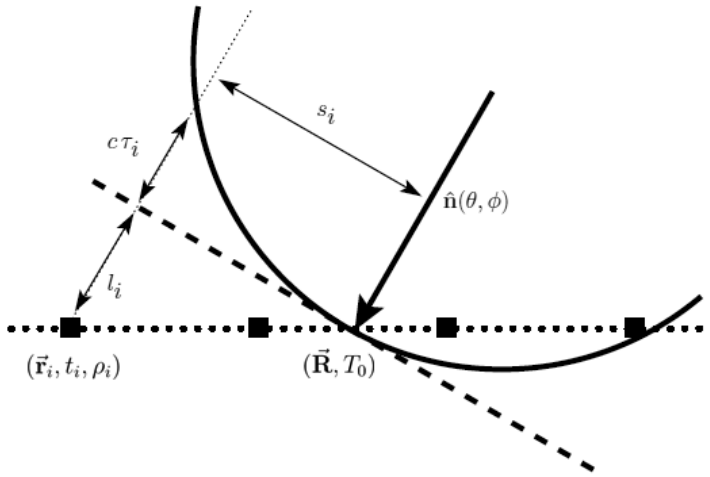

Figure 4.1: EAS front schematic at the time, T_0, that the shower core crosses the SD plane. The black squares are SDs. $\vec{\mathbf{R}}_{SD}$ is the shower crossing position, and the shower core axis unit vector (opposite the arrival direction) is $\hat{\mathbf{n}}(\theta, \phi)$. The SD counter positions are $\vec{\mathbf{r}}_i$, each triggered time is t_i, and ρ_i is the pulse height per unit area of the signal (VEM/m^2). The lateral distance of counter i from the shower axis is s_i, and l_i is the minimum distance between the plane perpendicular to the propagation axis (dashed line) $\hat{\mathbf{n}}$ and the counter. The distance $c\tau_i$ is the effect of the shower front curvature where τ_i is the time delay for counter i's part of the shower to reach the plane perpendicular to $\hat{\mathbf{n}}$. Adapted from [53].

at the CLF. The position for each SD counter, i, in the event is $\vec{\mathbf{r}}_i$.

For each counter in the event t_i is its triggered time, and ρ_i is the signal pulse height per unit area (VEM/m^2, VEM is the vertical equivalent muon, the average pulse height produced by vertically penetrating muons in the detector, described in Chapter 3.1.1). The lateral distance of counter i from the shower axis is s_i, and l_i is the minimum distance between the plane perpendicular to the propagation axis $\hat{\mathbf{n}}$ and the counter. The distance $c\tau_i$ is the effect of the shower front curvature where τ_i is the time delay for the counter i's part of the shower to reach the plane perpendicular to $\hat{\mathbf{n}}$.

The shower core axis unit vector is $\hat{\mathbf{n}}(\theta, \phi)$ and is given in terms of θ and ϕ in Equation 4.1a. Its projection on the SD plane, $\hat{\mathbf{u}}(\phi)$, is shown in Equation 4.1b.

$$\hat{\mathbf{n}}(\theta,\phi) = -[\sin(\theta)\cos(\phi)\hat{\mathbf{i}} + \sin(\theta)\sin(\phi)\hat{\mathbf{j}} + \cos(\theta)\hat{\mathbf{k}}] \tag{4.1a}$$

$$\hat{\mathbf{u}}(\phi) = -[\cos(\phi)\hat{\mathbf{i}} + \sin(\phi)\hat{\mathbf{j}} + 0\hat{\mathbf{k}}] \tag{4.1b}$$

4.1.2 Initial Values

To better reconstruct the event geometry when minimizing χ^2 functions, involving $\vec{\mathbf{R}}_{SD}$, θ, ϕ, and T_0 from Section 4.1.1, initial values are found using the individual detector information. The raw SD data are a list of scintillator photomultiplier tube (PMT) waveforms and their beginning times. First, the corrected event trigger time is found from the Flash Analog to Digital Converter (FADC) trace and the signal is calibrated using the 1 MIP (Minimum Ionizing Particle) and VEM (Vertical Equivalent Muon) calibration described in Section 3.1.1.

If an event has at least 3 adjacent counters with at least 3 MIPs the event is reconstructed. "Adjacent" means contiguous in space (closest detector in any direction) and time (time difference less than or equal to light travel time between them). SDs that are not adjacent are removed from the event and considered electronic noise or random atmospheric muons.

The initial value for the shower core position vector, $\vec{\mathbf{R}}_{SD}$, is simply the "center-of-gravity", $\vec{\mathbf{R}}_{COG}$, of the triggered detectors. This is the average of detector positions, $\vec{\mathbf{r}}_i$, weighted by pulse height, ρ_i, and is shown in Equation 4.2 for each orthogonal direction.

$$(R_{COG})_k = \frac{\sum_{i=1}^{N} \rho_i r_{ik}}{\sum_{i=1}^{N} \rho_i},\ k = x, y \tag{4.2}$$

The azimuthal angle, ϕ, is determined by $\hat{\mathbf{u}}(\phi)$ as shown in Equation 4.1b. The initial value for $\hat{\mathbf{u}}$ is found from the symmetric, ρ_i weighted, second-moment matrix of $\vec{\mathbf{r}}_i$. This is shown in Equation 4.3. This initial $\hat{\mathbf{u}}$ is defined, up to its sign, by the eigenvector of the larger of the two eigenvalues. The sign is later determined from timing.

$$M_{jk} = \frac{\sum_{i=1}^{N} \rho_i [r_{ij} - (R_{COG})_j][r_{ik} - (R_{COG})_k]}{\sum_{i=1}^{N} \rho_i},\ \begin{cases} j = x, y \\ k = x, y \end{cases} \tag{4.3}$$

The starting values for the remaining two variables, T_0 and θ, can be found by a linear fit to Equation 4.4a. This is a flat shower approximation so the shower curvature delay $\tau = 0$. t_i is each event counters trigger time and u_i, in Equation 4.4b, is the counter's distance from the initial core, $\vec{\mathbf{R}}_{COG}$ (along the $\hat{\mathbf{u}}$ axis). The intercept of the fit, at the minimum u_i, is the initial T_0 and the slope is $\sin(\theta)/c$. This gives the initial zenith angle, θ. If the resulting

slope is negative then the sign chosen for the initial $\hat{\mathbf{u}}$ is corrected and the linear fit redone.

$$t_i = \frac{l_i}{c} + T_0 = \frac{\sin(\theta)}{c} u_i + T_0 \tag{4.4a}$$

$$u_i = (\vec{\mathbf{r}}_i - \vec{\mathbf{R}}_{COG}) \cdot \hat{\mathbf{u}}(\phi) \tag{4.4b}$$

4.1.3 Pointing Direction Reconstruction

In order to calculate an event's origin (the pointing direction) accurate values of θ, ϕ and T_0 are needed. The χ^2 function minimized while varying T_0, θ, ϕ, and $\vec{\mathbf{R}}_{SD}$ is shown in Equation 4.5.

$$\chi^2_{Geom}(T_0, \vec{\mathbf{R}}_{SD}, \theta, \phi) = \sum_{i=1}^{N} \frac{(t_i - t_i^{Fit})^2}{\sigma^2_{t_i}} + \frac{||\vec{\mathbf{R}}_{COG} - \vec{\mathbf{R}}_{SD}||^2}{\sigma^2_{\vec{\mathbf{R}}_{COG}}} \tag{4.5}$$

The predicted trigger time of the i^{th} counter, t_i^{Fit}, is Equation 4.6. This is dependent on the perpendicular distance from the shower front plane to the detector, $l_i(\theta, \phi)$ (Equation 4.7), this distance is shown in Figure 4.1.

$$t_i^{Fit}(\theta, \phi) = T_0 + \frac{l_i(\theta, \phi)}{c} + \tau_i(\theta) \tag{4.6}$$

$$l_i(\theta, \phi) = (\vec{\mathbf{r}}_i - \vec{\mathbf{R}}_{SD}) \cdot \hat{\mathbf{n}}(\theta, \phi) \tag{4.7}$$

Each detector's t_i^{Fit} is also dependent on a modified Linsley function [55], $\tau_i(\theta)$, shown in Equation 4.8. This characterizes the signal delay time caused by the shower front curvature and is different than that used in [53]. In Equation 4.8 s_i is the perpendicular distance from the shower axis, $\hat{\mathbf{n}}(\theta, \phi)$, the pulse height per unit area is ρ_i, and "a" is the Linsley curvature parameter [62].

$$\tau_i(\theta) = a(\theta) \left(1 + \frac{s_i}{30m}\right)^{1.5} \rho_i^{-0.5}\ ns \tag{4.8a}$$

$$a(\theta) = 2.2 \cos(1.1\theta) \tag{4.8b}$$

The curvature parameter "a" was a free parameter in some previous analyses [53] [63]. In this analysis, and others [27] [28] [64], the "a" parameter shown in Equation 4.8b. It is dependent on zenith angle and was optimized from MC simulations to reduce the number of incorrect reconstructions. This reduces the number of free parameters in the χ^2_{Geom} minimization.

The σ uncertainties used in Equation 4.5 are listed in Equation 4.9. The uncertainty on each detector's trigger time, σ_{t_i}, is the uncertainty due to the FADC electronics 50 MHz sampling rate (σ_e=20 ns), and the uncertainty of the Linsley time delay (Equation 4.9b) added in quadrature. The "a" curvature parameter in the uncertainty is not changed from [53] and is a three part conditional function of zenith angle shown in Equation 4.9c. The uncertainty of the center-of-gravity core position, $\sigma_{\vec{\mathbf{R}}_{COG}}$=170 m, is an average calculated from the distribution of pulse heights in data [53].

$$\sigma_{t_i}(\theta) = \sqrt{\sigma_e^2 + \sigma_{\tau_i}^2} \tag{4.9a}$$

$$\sigma_{\tau_i}(\theta) = (7 \times 10^{-4}\mu s)a(\theta)\left(1 + \frac{s_i}{30m}\right)^{1.5}\rho_i^{-0.3} \tag{4.9b}$$

$$a(\theta) = \begin{cases} 3.3836 - 0.01848\theta & \theta < 25^\circ \\ 6.51 \times 10^{-5}\theta^3 - 0.00879\theta^2 + 0.299\theta - 0.0776 & 25^\circ \leq \theta < 35^\circ \\ exp(-3.2 \times 10^{-2}\theta + 2.0) & \theta \geq 35^\circ \end{cases} \tag{4.9c}$$

$$\sigma_e^2 = 20ns \tag{4.9d}$$

$$\sigma_{\vec{\mathbf{R}}_{COG}}^2 = 170m \tag{4.9e}$$

Once the minimum value of χ^2_{Geom} is found the events shower arrival time (T_0), zenith angle (θ), azimuth angle (ϕ), and SD core position ($\vec{\mathbf{R}}_{SD}$) are known. The values of T_0, θ, and ϕ are then used to find the events pointing direction, as shown in the following section, that is necessary for anisotropy studies.

4.1.3.1 Equatorial Coordinates

The equatorial coordinates used for ultra-high energy cosmic ray (UHECR) anisotropy studies are a spherical coordinate system defined by an origin at Earth's center and a plane through the equator with its normal vector pointing towards the vernal equinox. Once the local zenith (θ), azimuth (ϕ), and trigger time (t) are reconstructed for an event the pointing direction can be calculated. Right ascension (R.A.), α, is shown in Equation 4.10. Declination (Dec.), δ, is found from Equation 4.11. Azimuth (ϕ) is 0° with respect to cardinal North, altitude angle $a = 90^\circ - \theta$, t = Local Sidereal Time, and H is just an

intermediate variable [65]. The latitude and longitude are defined as the center of the TA SD at 39.3 Long., -112.9 Lat.

$$\sin(H) = -\sin(\phi)\cos(a)/\cos(\delta) \tag{4.10a}$$

$$\cos(H) = [\sin(a) - \sin(\delta)\sin(lat)]/\cos(\delta)\cos(lat) \tag{4.10b}$$

$$\alpha = t - H \tag{4.10c}$$

$$\sin(\delta) = \sin(a)\sin(lat) + \cos(a)\cos(lat)\cos(\phi) \tag{4.11}$$

4.1.4 Energy Reconstruction

In order to reconstruct an EAS event's incident particle energy the reconstructed geometry and signal size at some distance from the shower core are needed [66].

To reconstruct the signal lateral profile on the ground, a fit to the AGASA lateral distribution function (LDF) [56], Equation 4.12, is done by minimizing the χ^2 of Equation 4.13.

$$\rho_i^{Fit}(A) = A\left(\frac{s_i}{r_M}\right)^{-1.2}\left(1+\frac{s_i}{r_M}\right)^{-(\eta(\theta)-1.2)}\left(1+\left[\frac{s_i}{1000m}\right]^2\right)^{-0.6} \tag{4.12a}$$

$$\eta(\theta) = 3.97 - 1.79[\sec(\theta) - 1] \tag{4.12b}$$

$$\chi^2_{LDF}(A,\vec{\mathbf{R}}) = \sum_{i=1}^{N}\frac{(\rho_i - \rho_i^{Fit})^2}{\sigma^2_{\rho_i}} + \frac{||\vec{\mathbf{R}}_{COG} - \vec{\mathbf{R}}||^2}{\sigma^2_{\vec{\mathbf{R}}_{COG}}} \tag{4.13}$$

In Equation 4.12 $r_M = 91.6$ m is the Moliere multiple scattering length. The fit parameters are the core position $\vec{\mathbf{R}}$ and LDF scaling factor A. The resulting $\vec{\mathbf{R}}$ is not used in updating the geometry fit and s_i and θ are not varied from the final result of the geometry fit. The functional form of the uncertainties on the pulse height density were found empirically from TA SD data and are shown in Equation 4.14.

$$\sigma_{\rho_i} = \sqrt{6.3\times10^{-3}\rho_i^2 + 0.56\rho_i} \tag{4.14a}$$

$$\sigma^2_{\vec{\mathbf{R}}_{COG}} = 170m \tag{4.14b}$$

Detectors with saturated photomultiplier tubes, $\rho_i \geq \sim 50$ VEM within 20 ns, are removed from the lateral distribution fit (not from the geometry fit). There are $\sim$1 of these per event.

Once the χ^2_{LDF} has been minimized, and the scaling factor "A" determined, the density of particles at a lateral distance perpendicular to the shower core is found using the LDF Equation 4.12, for any distance "r." A distance of 800 meters from the shower core has been determined to be a stable indication of shower energy for an array with detectors of this size (3 m^2) and separation (1.2 km) in [53] following the method of [66].

The density of particles at this point is $\rho(800m) \equiv S(800)$. Once $S(800)$ is found, a "rainbow plot" is used to determine the energy. This table, shown in Figure 4.2, is populated by a large number of CORSIKA generated Monte Carlo (MC) simulated through the detector response (as described in Section 3.3) and reconstructed using the same method outlined for data above. The "thrown" or generated energies are shown in 2-d bins of the reconstructed $\log_{10}(S(800))$ and $\sec(\theta)$. The assigned reconstructed energy of an event is the energy at the intersection of these two values.

Once the initial energy of a reconstructed event is found it is renormalized to match the calorimetrically determined energy scale of the TA FD [63]. The initial SD energy has been compared to the TA FD for events that were successfully reconstructed by both methods. It was found that to minimize the average difference between these energies the SD energy should be reduced by a factor of $1/1.27$ for the final energy determination.

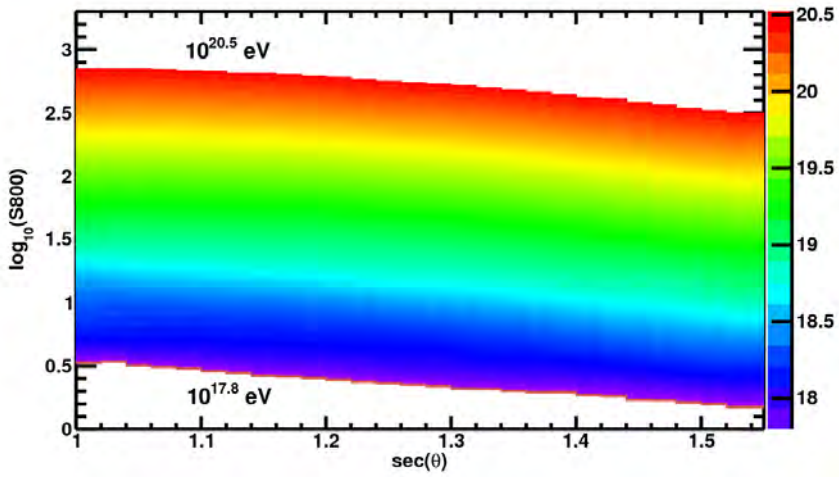

Figure 4.2: TA SD energy estimation table – the "rainbow plot." Populated by CORSIKA MC simulated through the detector response and reconstructed using the same method as data. The average "thrown," or generated energies, are in 2-d bins of reconstructed $\log_{10}(S(800))$ and $\sec(\theta)$. The assigned reconstructed energy of an event is given by the color, in $\log_{10}$(E/eV), at the intersection of these two values. Taken from [53]

4.2 Event Selection

Poorly reconstructed events must be removed from the data set before analysis. The cuts applied to the SD data for the following anisotropy analyses of Part 2 are listed below. These cuts are optimized for energy resolution, zenith angle resolution, and agreement between data and MC for the expected zenith angle distribution (see Section 7.3).

1. Energy E $\geq$ 10 EeV.
2. Each event includes at least four surface detectors.
3. Event arrival direction zenith angle, θ, is limited to 55°.
4. Reconstructed event pointing direction uncertainty less than 5°.
5. Event core distance from array boundary $>$ 1.2 km.
6. Lateral distribution goodness of fit $\chi^2/\text{dof} < 10$.

4.2.1 Energy Cut

Above energies of 10^{19} eV the detection efficiency is $\sim$100%. This is the minimum energy threshold considered for all anisotropy analysis of Part 2 so that efficiency corrections are unnecessary.

4.2.2 N Counters Cut

Low energy events that trigger few counters, and have smaller numbers of particles, can be reconstructed with much higher apparent energy due to a less equally dispersed energy deposit (large fluctuations) in the SDs. These low energy low # of SD events can contaminate the highest energy spectrum features so a minimum of four triggered SDs are required. This cut also improves the zenith angle resolution as there are more data points for the reconstruction described in Section 4.1.3.

4.2.3 Zenith Angle Cut

Events with zenith angles θ>60° are difficult to reconstruct as the resulting slant depth can be very large. This results in the same problem as for low N counter events where there are large fluctuations in signal due to the unequal dispersion of energy. The actual cut is for events with θ>55° as these zenith angles are not well described by the TA MC simulation.

4.2.4 Pointing Direction Uncertainty Cut

The uncertainties on the zenith angle, θ, and azimuthal angle, ϕ, are reported by the minimization of the geometry fit χ^2_{geom} of Equation 4.5. These two uncertainties are combined into the pointing direction uncertainty according to Equation 4.15.

$$\sigma_p = \sqrt{\sigma_\theta + (\sigma_\phi \sin\theta)^2} \tag{4.15}$$

Removing events with large σ_p is important for anisotropy studies as these two variables are necessary to find the pointing direction. Events with $\sigma_p \leq 5^\circ$ are found to be well reconstructed from MC simulation and better follow the expected zenith angle distribution. This cut also improves the energy resolution of events as zenith angle is used in the energy determination as described in Section 4.1.4.

4.2.5 Boundary Cut

A boundary distance cut of events with $D_{border} < 1.2$ km is made as this is the distance between SDs. Therefore, at least one SD counter is expected between the core position, $\vec{\mathbf{R}}$, and the array boundary. This helps ensure that the triggered SDs are closer to the expected conic section shape – this removes some underestimated energy events and improves the zenith angle resolution. It also improves the agreement between the expected zenith angle distribution and data.

4.2.6 Lateral Fit Cut

Cutting events with a lateral distribution fit $\chi^2_{LDF}/dof > 10$ is done mainly to improve the zenith angle resolution and the agreement between the expected zenith angle distribution and the data. This also slightly improves the energy resolution.

4.3 Summary

After cuts, there are 3027 events in the data set. A scatter plot of events colored by energy is shown in Figure 4.3.

These cuts are tighter than the "Hotspot" paper [27] and are necessary for the lower energy threshold of E$\geq$10 EeV. The additional cuts are made to improve the zenith angle distribution agreement between data and MC. The energy, and zenith angle, resolutions are also improved at lower energies; these range from $\sim$10 to 15%, and $\sim 1.0^\circ$ to 1.5°,

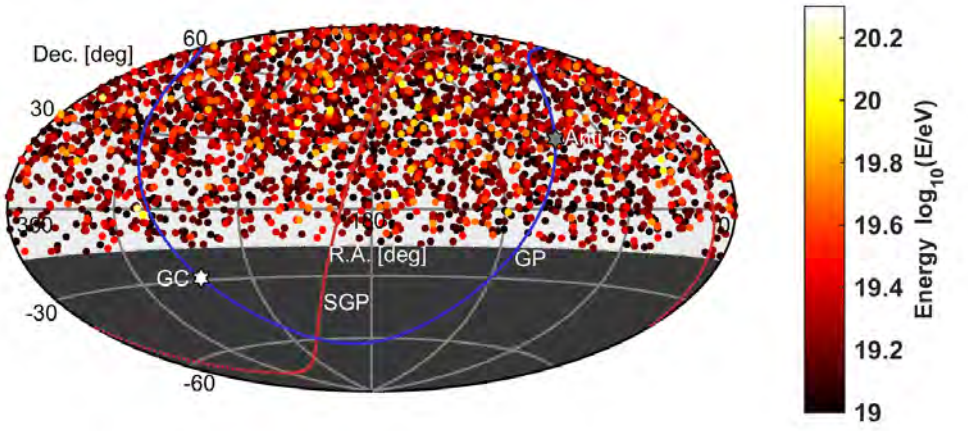

Figure 4.3: Equatorial coordinate Hammer-Aitoff projection of UHECR events in the data set with energies E≥10 EeV. The colors are energy in $\log_{10}$(E/EeV). The dashed curve at Dec. = -16° defines the Field-of-View (FoV). Solid curves indicate the galactic plane (GP) and supergalactic plane (SGP). White and grey hexagrams indicate the galactic center (GC) and galactic anticenter (Anti-GC).

depending on core distance from the array boundary. Both resolutions improve with increasing energy [53].

In Chapter 7 the azimuthal angle distribution is shown to be in agreement with a flat distribution. The energy spectrum is also in agreement with the published spectrum [63] [34]. Distributions of the SD data trigger time and equatorial coordinates are also compared and are shown to be in agreement.

CHAPTER 5

HYBRID FD/SD RECONSTRUCTION AND DATA

For the following composition analysis in Part 3, approximately 7 years of Telescope Array (TA) hybrid reconstructed fluorescence detector (FD) and surface detector (SD) data recorded between 2008 May 27 and 2015 April 24 was used. As described in Chapter 4 (with changes listed in Section 5.1) the initial geometry, arrival time, and core location calculation of the shower is performed using the trigger times of the SDs. A lateral distribution function is used to fit the particle densities perpendicular to the shower core location, generating a more accurate geometrical reconstruction of the shower.

This initial geometry is used for the hybrid reconstruction where particle density and timing from SDs are combined with FD tube timing and geometry to generate a longitudinal profile, from which X_{max} is calculated. Each PMTs view of the shower is converted into slant depth (g/cm^2) and compared to a library of Monte Carlo (MC) simulated showers generated by CORSIKA [46]. This gives the value of X_{max} and energy for the event.

The mono Middle Drum (MD) FD (Section 3.2) reconstruction is based on the HiRes reconstruction [67] and uses much of the same code [45]. The hybrid reconstruction method, which makes use of the mono MD method, is described in further detail in [68] [57] and [34], though the analysis in this thesis uses different starting parameters in the X_{max} reconstruction and a different atmospheric model. These differences are discussed in Section 5.2.4 and were used in [59].

5.1 SD Reconstruction Difference

In the mono SD reconstruction used for the anisotropy studies in Part 2 the Linsley curvature parameter "a" was dependent on zenith angle as described in Chapter 4.1.3 and shown in Equation 4.8. In the SD part of the hybrid reconstruction used here two versions are used in an iterative process, this is the same SD reconstruction used in [53], and [63].

For the first iteration of the timing fit of Equation 4.6, the Linsley curvature parameter "a," is dependent on zenith angle with the form shown in Equation 4.9c, and the τ_i is shown in Equation 5.1. The τ_i's uncertainty σ_{τ_i} is the same as Equation 4.9b. The χ^2_{Geom} function minimized is unchanged from Equation 4.5. The minimization gives the preliminary value of the events shower arrival time (T_0), zenith angle (θ), azimuth angle (ϕ), and SD core position ($\vec{\mathbf{R}}_{SD}$) to be used as the starting values for the next iteration.

$$\tau_i = (8 \times 10^{-4} \mu s) a(\theta) \left(1 + \frac{s_i}{30m}\right)^{1.5} \rho_i^{-0.5} \; ns \tag{5.1}$$

In the next iteration the Linsley curvature parameter "a" is a free parameter. The equation for the curvature delay τ_i, which is used in the minimization of the χ^2_{Geom} (Equation 4.5), is shown in Equation 5.2. The factor $1 - \frac{l_i}{1.2 \times 10^4 m}$ is an additional "curvature development" factor calculated from preliminary data analysis [53].

$$\tau_i = a \left(1 - \frac{l_i}{1.2 \times 10^4 m}\right)^{1.05} \left(1 + \frac{s_i}{30m}\right)^{1.35} \rho_i^{-0.5} \; ns \tag{5.2a}$$

$$\sigma_{\tau_i} = (1.56 \times 10^{-3} \mu s) \left(1 - \frac{l_i}{1.2 \times 10^4 m}\right)^{1.05} \left(1 + \frac{s_i}{30m}\right)^{1.5} \rho_i^{-0.3} \tag{5.2b}$$

Once χ^2_{Geom} is again minimized the resulting $\vec{\mathbf{R}}_{SD}$ can be used in the hybrid FD/SD reconstruction described in the next section. The resulting arrival time, T_o, is used for combining into hybrid events the FD, and SD, events with times that are within 2 μs of each other.

5.2 Event Reconstruction

5.2.1 Definitions

As with the surface detector reconstruction of Chapter 4 the coordinate system for the shower core is centered at the Central Laser Facility (CLF) (3.1). The other relevant parameters in the hybrid reconstruction are centered on the fluorescence detector within the Shower Detector Plane (SDP). The SDP is the intersection of the shower axis $\hat{\mathbf{n}}$ (Equation 4.1a) and the location of the FD. A schematic of the SDP and the reconstruction variables within it are shown in Figure 5.1.

The SDP normal vector is $\hat{\mathbf{N}}$. The in-plane angle, ψ, is the angle between the SD plane and the event arrival direction unit vector $\hat{\mathbf{n}}$ within the SDP. The trigger time of each triggered PMT tube is t_i, the number of photoelectrons seen by the tube is w_i, and it's

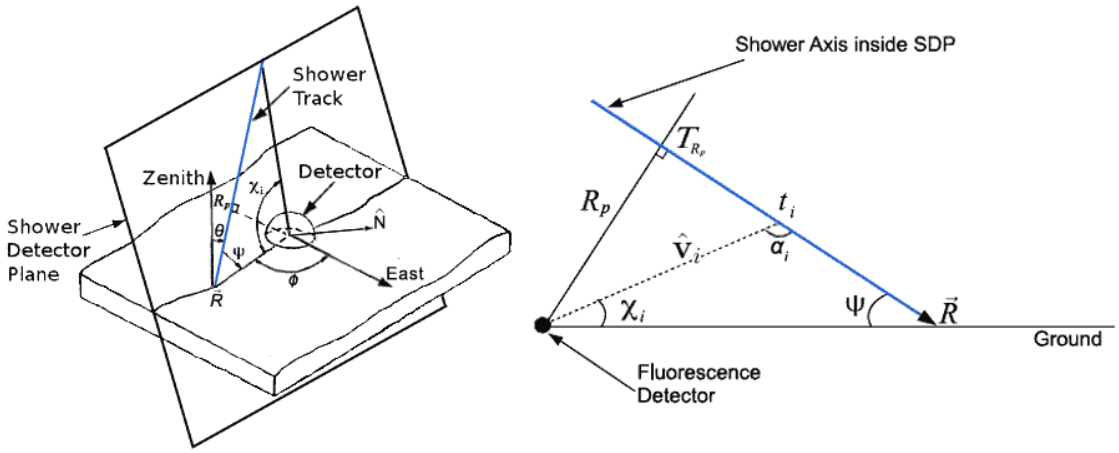

Figure 5.1: Fluorescence detector (FD) extended air shower (EAS) geometry: The shower detector plane (SDP) is the intersection of the shower core axis with the FD location. The five fitted parameters are the SDP normal vector, $\hat{\mathbf{N}}$, impact parameter (distance of closest approach), R_p, time of closest approach, T_{R_p}, in-plane angle, ψ, and shower core, $\vec{\mathbf{R}}_{hybrid}$. The zenith and azimuthal angles are derived from these values. The zenith angle, θ, is between the zenith arrow and the shower axis (zero angle is parallel to the zenith arrow). The azimuthal angle, ϕ, is the core's anticlockwise angle from the East. The trigger time, t_i, viewing direction, $\hat{\mathbf{v}}_i$, number of photoelectrons, w_i, and tube center angle, χ_i, for each tube are the values used in the fitting.

viewing angle χ_i is the angle between the SD plane and the tubes viewing direction $\hat{\mathbf{v}}_i$. The impact parameter, R_p, is the distance of closest approach between the shower axis $\hat{\mathbf{n}}$ and the FD. T_{R_p} is the time that the shower reaches the R_p distance. $\vec{\mathbf{R}}_{hybrid}$ is the hybrid reconstructed shower core position vector.

The zenith angle, θ, and azimuthal angle (the angle of the core measured anticlockwise from East) are calculated from the above reconstructed variables and are also shown in Figure 3.1.

5.2.2 Middle Drum (MD) Reconstruction

The raw MD data is a list of GPS time-stamp trigger times, Charge to Digital Converter (QDC) counts from photomultiplier tubes (PMT), and tube timing information from Time to Digital Converters (TDC). The first step in reconstruction is to build events by combining telescopes with trigger GPS time-stamps within 100 μs of each other.

The TDC values of each PMT are next converted into microseconds relative to the first telescope trigger time and the PMT QDC values are converted into the number of photoelectrons using the calibration method of Section 3.2.1. Also, nonevents such as the 1

Hz UVLED signals and 30 minute CLF laser shots used for calibration, described in Section 3.2.1, are removed from the event list.

5.2.2.1 Rayleigh Event Filter

The Rayleigh filter determines the probability that the events pattern of triggered PMTs in the camera appears to be a random walk, as opposed to "track-like," using the Rayleigh probability distribution. The Rayleigh distribution is the distribution of the magnitude of a vector with component directions that are uncorrelated and normally distributed (centered on zero) with equal variances. Extended Air Shower (EAS) tracks across the face of the camera are not expected to follow this distribution.

A unit vector, $\hat{\mathbf{z}}_\mathbf{i}$, is drawn between each triggered tube in an event and all its nearest-neighbor triggered tubes that occur later in time $t_i < t_j$. Later time nearest-neighbor tubes are triggered 0.02 to 8.00 μs after the origin tube and up to 1.5° away (tube separation within a cluster is 1.0°, nearest tubes in viewing angle can be up to 1.5° apart in adjacent mirrors). The magnitude of the vector sum of these segments, $|\vec{\mathbf{Z}}| = Z$, is used to determine the probability that the event is not an EAS track.

In the Rayleigh distribution Equation 5.3, $z = |\vec{\mathbf{z}}| = |\sum_{i=0}^{N} \hat{\mathbf{z}}_\mathbf{i}|$, and is the magnitude of the resultant vector of the sum of independent random unit vectors.

$$f(z) = \frac{z}{\sigma^2} exp\left(-\frac{z^2}{2\sigma^2}\right) \tag{5.3}$$

In this case $\sigma^2 = N/2$, where N is the total number of drawn unit vectors on the triggered tubes of the event. Integrating Equation 5.3 from Z to ∞ gives the probability that Z is the result of a random walk process. This is shown in Equation 5.4.

$$Prob(z > Z) = \int_Z^\infty p(z)dr = exp\left(-\frac{Z^2}{2\sigma^2}\right) \tag{5.4}$$

For convenience the base-10 logarithm is used for the probability threshold. This is shown in Equation 5.5 with σ substituted.

$$plog = \frac{Z^2}{Nln(10)} \tag{5.5}$$

Events with $plog \geq 2.0$, corresponding to a probability $\leq$ 1% of being noise, are not removed. This threshold on the probability reduces the number of triggered events by about ∼99.6%, from hundreds of millions to tens of millions. Most triggers from night sky

fluctuations, airplanes, and even car headlights, are removed in this step. The majority of events not yet removed are from the Xenon flashers and atmospheric monitoring YAG laser shots described in Section 3.2.1.

The vector $\vec{\mathbf{Z}}$ is further used to determine whether an event is downward-going toward the ground, horizontal, or upward-going. Xenon flashers and YAG laser shots are upward-going and are flagged for calibration use. Events are flagged as horizontal if they have an $\vec{\mathbf{Z}}$ vector $\pm 20^\circ$ from horizontal (less than 10% of these are EAS events and only a percentage of these EAS would be reconstructable).

5.2.2.2 Shower Plane Reconstruction

The shower detector plane (SDP) shown in Figure 5.1 is found using the pointing directions, $\hat{\mathbf{v}}_i$, and photoelectrons, w_i, of the triggered PMTs. The SDP is defined by its normal unit vector $\hat{\mathbf{N}}$ and this is found by an iterative minimization of the χ_{SDP} function in Equation 5.6. For this fit the shower is treated as a line source so its lateral extent is ignored. Also, the mirror positions are ignored and are assumed to lie at a single point at the origin.

$$\chi^2_{SDP} = \sum_i \frac{w_i(\hat{\mathbf{N}} \cdot \hat{\mathbf{v}}_i)^2}{\sigma^2} \tag{5.6}$$

The sum is over triggered tubes, $\hat{\mathbf{v}}_i$ is the tube viewing direction vector, and w_i is the number of photoelectrons. The σ error is the 1.0° size of the PMT and can be ignored as it's the same for every tube. The weighting by the number of photoelectrons makes this an amplitude weighted plane fit.

Usually EAS events contain a number of noise triggered tubes, "bad tubes," in addition to the "good tubes." To remove bad tubes the fit is iterated. Once the initial SDP is found a quadratic function is fit to the SDP tube angle, χ_i, and it's trigger time, t_i. Then χ_{SDP} is minimized again using only tubes less than 3 RMS deviations away from the quadratic fit. This process is repeated until no more tubes are removed. If less than three tubes remain then the event is rejected.

5.2.2.3 Artificial Source Removal

There are a number of laser triggered events that may not be removed by the Rayleigh filter. The next step is looking for events that are similar in time, core location, amount of

light seen, and SDP vectors.

Events are removed if they are triggered within 9 seconds of each other, they share 3 or more good tubes, the number of photoelectrons for the top six tubes are within 30% of each other, and their SDP normal vectors are within 10° of each other.

5.2.3 Hybrid Geometry Reconstruction

The remaining four shower geometry parameters to be found, after the SDP unit vector ($\hat{\mathbf{N}}$), are the impact parameter (closest approach distance), R_p, time of closest approach (T_{R_p}), in-plane angle (ψ), and shower core vector ($\vec{\mathbf{R}}_{hybrid}$). These are all shown in Figure 5.1. From these and the SDP normal unit vector ($\hat{\mathbf{N}}$), the zenith angle (θ), and azimuth angle (ϕ), can be calculated.

The hybrid shower geometry is found by the minimization of the χ^2 shown in Equation 5.7. This takes into account FD and SD timing as well as the surface detector signals.

$$\chi^2_{hybrid} = \chi^2_{t_{MD}} + \chi^2_{t_{SD}} + \chi^2_{Core} \tag{5.7}$$

5.2.3.1 Middle Drum Geometry χ^2

Given that the tube trigger times are known the $\chi^2_{t_{MD}}$ component of Equation 5.7 is shown in Equation 5.8a. The uncertainty is $\sigma_{t_i} = 500/\sqrt{w_i}\ ns$ where w_i is the tube signal in number of photoelectrons [67]. Equation 5.8b relates the time that each tube triggered, t_i, and the tube viewing angle, χ_i, to the SDP in-plane variables to be reconstructed (simplifying with the EAS traveling at the speed of light).

$$\chi^2_{t_{MD}} = \sum_{i=1}^{N} \frac{1}{\sigma^2_{t_i}} \left\{ t_i - \left(T_{R_P} + \frac{R_P}{c} \tan\left(\frac{\pi - \psi - \chi_i}{2} \right) \right) \right\} \tag{5.8a}$$

$$t_i = \left(T_{R_P} - \frac{R_P}{c \tan(\alpha_i)} \right) + \frac{R_P}{c \sin(\alpha_i)} = T_{R_P} + \frac{R_P}{c} \tan\left(\frac{\pi - \psi - \chi_i}{2} \right) \tag{5.8b}$$

5.2.3.2 Virtual PMTs from SDs χ^2

In the next component, $\chi^2_{t_{SD}}$, of Equation 5.7 considers each triggered SD as a "virtual PMT" located at MD and is shown in Equation 5.9a – it has the same form as Equation 5.8a. The virtual PMT geometry used is shown in Figure 5.2, where the t_{SD_i} are the virtual PMT trigger times, which are the coincident SD trigger times plus the time of light delay due to the distance between the individual SDs and the MD detector, D_i (Equation 5.9b). The

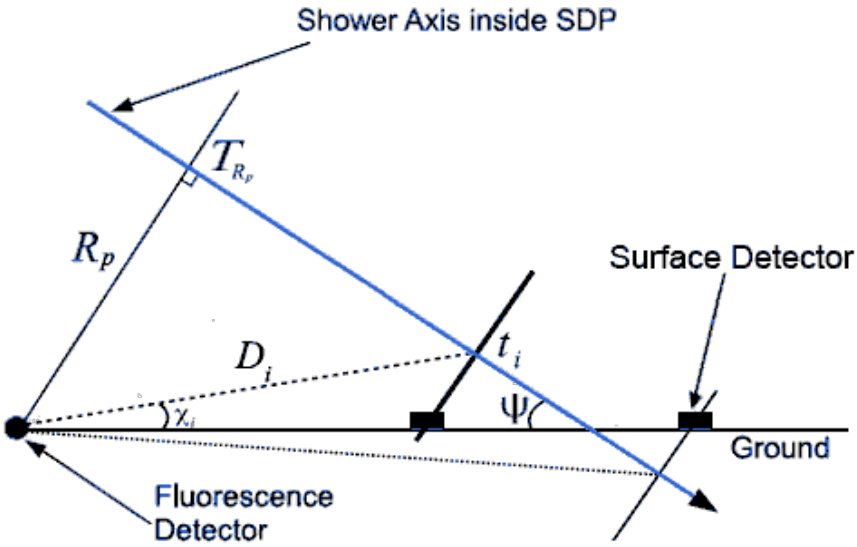

Figure 5.2: Virtual Middle Drum (MD) FD photomultiplier tube (PMT) from FD/SD geometry within the SDP. The "virtual PMT" trigger time, t_{SD_i}, is the SD trigger time, t_i, plus time of light travel delay D_i/c. The virtual PMT viewing angle is χ_i. The dotted line shows this angle can be negative for SD sufficiently far away from the MD FD.

virtual PMT viewing angle is the angle between MD and the shower core point within the shower that triggers the SD (if the SD is far enough away from MD this angle can be negative).

$$\chi^2_{t_{SD}} = \sum_{i=1}^{N} \frac{1}{\sigma^2_{t_i}} \left\{ t_{SD_i} - \left(T_{R_P} + \frac{R_P}{c} \tan\left(\frac{\pi - \psi - \chi_i}{2} \right) \right) \right\} \tag{5.9a}$$

$$t_{SD_i} = t_i + \frac{D_i}{c} \tag{5.9b}$$

This virtual PMT extension adds a significant number of data points to the geometry fit and results in a significant improvement to the resulting χ^2/dof.

5.2.3.3 Shower Core χ^2

The last component of the hybrid geometry χ^2_{hybrid} minimization fit, χ^2_{Core}, is the hybrid core constraint shown in Equation 5.10. Here $\vec{\mathbf{R}}_{COG}$ is the SD "center-of-gravity" result of Equation 4.2 and $\vec{\mathbf{R}}_{hybrid}$ (x-y component vector) is the varied hybrid core location ($\sigma^2_{\vec{\mathbf{R}}_{COG}}$=170 m as before).

$$\chi^2_{Core} = \frac{||\vec{\mathbf{R}}_{hybrid} - \vec{\mathbf{R}}_{COG}||^2}{\sigma^2_{\vec{\mathbf{R}}_{COG}}} \tag{5.10}$$

5.2.3.4 Geometry Fit Summary

In the minimization of χ^2_{hybrid}, Equation 5.7, five parameters are found (ϕ, θ, R_p, R_x, and R_y) by their variation using known values from both the MD FD and the SDs. The end result is the hybrid geometry reconstruction of the UHECR event.

5.2.4 X_{max} Reconstruction

The X_{max} reconstruction uses the fitted hybrid geometry and converts the viewing angles of the "good" PMTs into the slant depth in g/cm^2. This is done using the same GDAS atmospheric profile discussed in Section 3.2.1. This results in a "shower profile" of signal (photoelectrons) versus slant depth that is fit to the Gaisser-Hillas profile shown in Equation 5.11. Examples of shower profiles can be found in Chapter 12.

$$N(X) = N_{max}\left(\frac{X - X_0}{X_{max} - x_0}\right)^{(X_{max}-X_0)/\lambda} \exp\left(\frac{X_{max} - X}{\lambda}\right) \tag{5.11}$$

In the reconstruction used in this thesis the scaling factor is a fixed value, λ = 70 g/cm^2, and the initial first interaction depth is X_0 = -60 g/cm^2 but is allowed to vary. The values of N_{max}, and X_{max}, are also varied. The best fit gives the value of X_{max}.

Previously, in [38], and [57], the first interaction depth was fixed at X_0 = 40 g/cm^2. This was changed to match with the analyses used by the other FD sites and resulted in minor improvement to the X_{max} resolution and its variation with energy. X_{max} resolution is measured by the RMS of the MC thrown X_{max} value before reconstruction minus the X_{max} value after reconstruction (RMS[$X_{max}{}^{thrown}$-$X_{max}{}^{reconstructed}$]).

5.2.5 Energy Reconstruction

The event energy is reconstructed by an inverse Monte Carlo method. The data event shower profile is compared to the profiles of reconstructed Monte Carlo simulations (described in Chapter 3.3). The data event energy is taken from the reconstructed simulation's energy with a shower profile that minimizes Equation 5.12 (S_i are the shower profile bins signal values). Example shower profiles can be found in Chapter 12

$$\chi^2_{profile} = \sum_i \frac{1}{\sigma_i^2}\left(S_i^{data} - S_i^{MC}\right)^2 \tag{5.12}$$

5.3 Event Selection

Resolution energy dependence comes from events that do not show a pronounced shower maximum (X_{max}) in the detector the field-of-view (FOV). Since UHECR particle composition could be energy dependent (PAO results indicate an energy dependent narrowing of the X_{max} distribution [40]) a set of cuts is needed to minimize the energy dependence of the X_{max} resolution. Typically these are lower energy events. χ^2 cuts on the Gaisser-Hillas profile fits (Equation 5.11) are not sufficient to reject most events that have poorly defined X_{max}.

In this thesis an updated version of the pattern recognition analysis (Binary PRA) method (as described in [68] and Chapter 12), that selects events that have a clear rise and fall in shower profile signal, is used. This Quality Factor Analysis (QFA) applies logistic regression to the output of the PRA to set a scale of "quality" for each event on the data set. This is described in Section 12.3.

Events with X_{max} in the FOV of the detector could still be incorrectly reconstructed, therefore, cuts that take into account the geometry of the events need to be applied in addition to the QFA threshold. The geometry cuts were optimized by a systematic iterative process for further minimizing the energy dependence of the X_{max} resolution. Also, taken into account was the overall resolution (and bias) for both X_{max} and energy while maximizing the total number of events accepted. The resulting set of optimized geometry cuts are looser than previous analysis and are listed below. Events that satisfy the inequalities are not removed from the data set.

1. Quality Factor QF$\geq$ 19.6% – probability of being a good event (Chapter 12).
2. Weather cut: Clouds not limiting the FD FOV.
3. Failmode: Profile reconstruction failures are removed.
4. Energy $\geq 10^{18.4}$ eV
5. Zenith angle $\leq 58^{\circ}$
6. Boundary Distance ≥ -500 m (negative values are outside the array)
7. Hybrid/Surface Core Difference ≤ 1600 m
8. Geometry Fit χ^2/DOF ≤ 5
9. Start X_{max} Bracket: (X_{max} - X_{start}) ≥ 0 g/cm^2
10. End X_{max} Bracket: (X_{end} - X_{max}) ≥ 0 g/cm^2

5.3.1 Weather Cut

The scattering of light through clouds cannot be accurately estimated by the shower track reconstruction. Therefore, a cloud cover removal of events is required. The weather at Middle Drum is checked by eye every 40 minutes during the run time. If the overhead cloud cover is less than 50% and if there are no clouds below 25° (from the horizon) towards the South or East (but not both) then the events are passed. If there are clouds below 25° in both the South and East then the overhead cloud cover must be less than 25% for the events to pass.

Events that are missing shower profile information due to smaller thicker clouds are also removed by the pattern recognition QF cut.

5.3.2 Energy Cut

Low energy events emit less light and due to the hybrid requirement and the distance between the MD FD and the SD array edge events reconstructed with energies less than $10^{18.4}$ eV are removed from the data set. This improves both energy and X_{max} resolutions and biases and the detection efficiency is fairly constant above this energy.

5.3.3 Zenith Angle Cut

The Monte Carlo simulations do not simulate showers with zenith angles greater than 60° so data events must be cut below this value. Taking into account the zenith angle resolution this limit is reduced to 58°. Previously, the limit for MD was 56° but the pattern recognition QF cut improves the zenith angle resolution.

5.3.4 Boundary Cut

Showers with cores that fall far outside the border of the array are missing detector information for the core determination and virtual PMTs used in the geometry reconstruction. The previous requirement was that the core must be at least 100 m away from the array boundary. This was loosened to -500 m outside the array due to the fact that events which pass the QF cut generally have longer track lengths, and higher signal, both of which improve the geometry reconstruction

5.3.5 Hybrid SD Core Difference Cut

If the difference between the SD determined shower core, and the hybrid determined core, is too large it is likely that the signals are the combination of more than one shower.

5.3.6 Geometry Fit Cut

This is a limit on the resulting fit from the minimization of χ^2_{hybrid} from Section 5.7. If the χ^2_{hybrid}/dof is greater than 5 then the geometry of the shower, and therefore energy and X_{max} are likely not well determined.

5.3.7 X_{max} Bracketing Cut

Events with the Gaisser-Hillas model X_{max} determined to be outside the FOV are removed. This improves the energy and X_{max} resolutions.

5.4 Data Compared to Simulation

The resulting shower geometry variable comparisons (ϕ, ψ, R_p, and θ) show good agreement between data, and reconstructed MC, as shown by Figure 5.3. All distributions have a CvM-test (Chapter B) p value greater than 13% indicating that data, and proton MC, belong to the same parent distribution. The energy is also in very good agreement with the reconstructed MC HiRes energy spectrum [63] as shown by Figure 5.3e.

5.5 X_{max} Systematics

Systematic errors in the reconstruction will result in uncertainties (and bias) on the mean X_{max}. Direct and scattered Cherenkov light must be subtracted to determine X_{max}. The systematic effects of uncertainties in this subtraction have been previously studied and have been found to be negligible [69]. This effect is further minimized as the hybrid trigger requirement reduces the signal seen at small angles to the shower axis and therefore reduces the amount of direct Cherenkov light.

Mirror alignments are another source of systematic uncertainty. Mirror surveys done using star alignments were compared to theodolite based measurements and it is estimated that mirror pointing directions are known to $\pm 0.05^\circ$. For an average shower, at average core distance, and mean zenith angle, the resulting uncertainty in mean X_{max} is 2.6 g/cm^2.

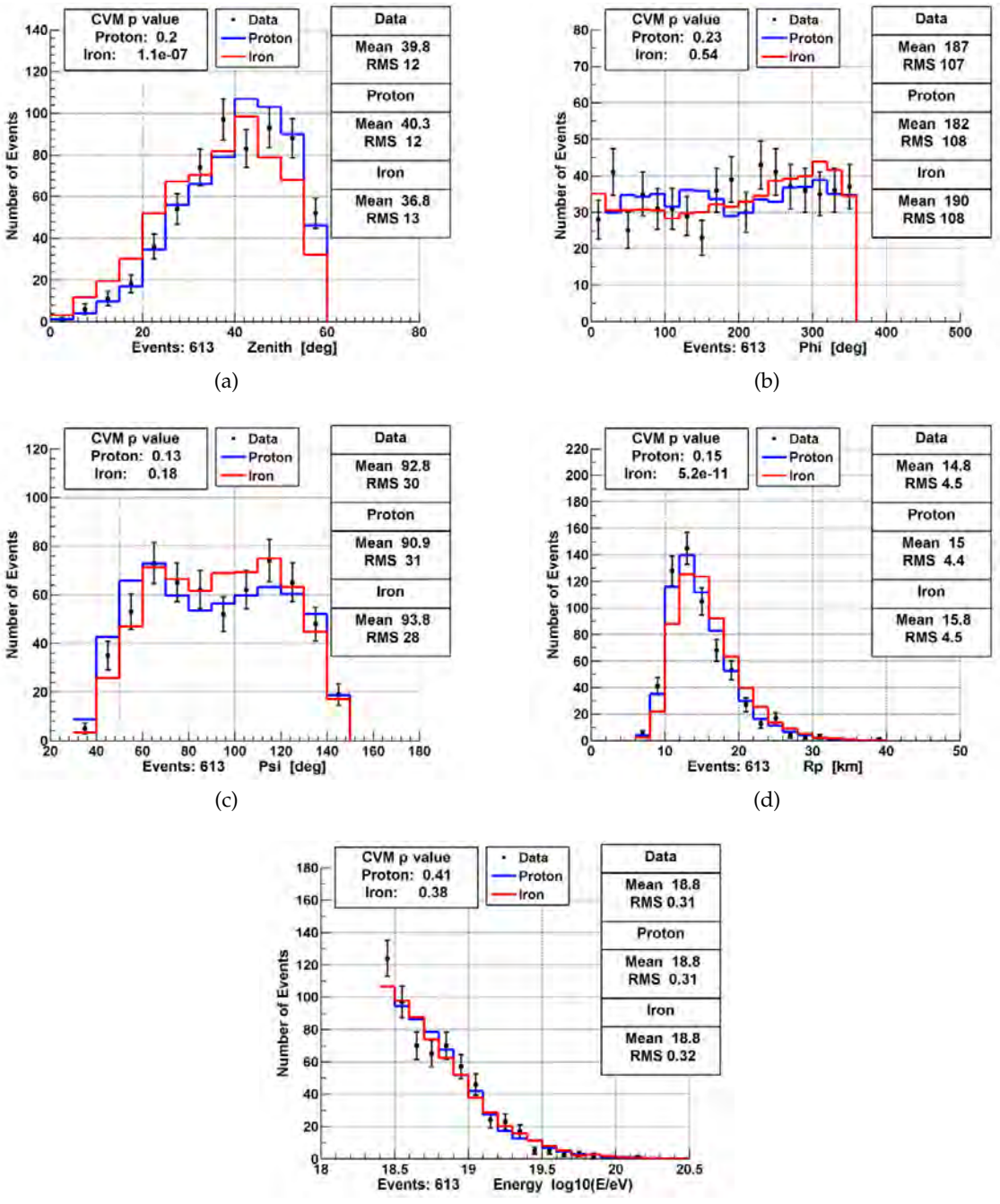

Figure 5.3: Resulting hybrid FD/SD reconstruction shower variable (ϕ, ψ, R_p, θ, and energy) distribution data/MC comparisons. Data (black points with error bars), QGSJETII-03 proton MC (blue histogram), and iron MC (red histogram). The MC has been normalized to the area of the data. The CvM-test p-values show much better agreement between data and proton for the two composition dependent variables (zenith angle and R_p). (a) Zenith angle distributions. (b) Azimuthal angle distributions. (c) SDP angle distribution. (d) R_p distance distributions. (e) Energy distributions.

The atmospheric density profile uncertainty is estimated by comparing the GDAS atmosphere [60] used in this analysis with the US 1976 Standard Atmosphere [58]. This contributes an additional mean X_{max} uncertainty of 11.7 g/cm^2 and the resulting systematic error on the elongation rate is 3.8 g/cm^2 per energy decade.

The aerosols contribution to atmospheric attenuation in the distance between EAS, and the FD, is assumed to be constant and corresponds to a vertical aerosol optical depth (VAOD) of 0.04. This is the same value used in the HiRes analysis. The effect of nightly VAOD variations (as determined by LIDAR) has been previously studied [70]. For the clear night weather cut it is estimated to contribute a systematic error of 2.0 g/cm^2 on X_{max}, and a net shift in the elongation rate of 2.2 g/cm^2 per energy decade.

Therefore, the total systematic error on mean X_{max}, not accounted for by the reconstruction, is 16.3 g/cm^2. The total systematic error on the elongation rate, not accounted for by the reconstruction, is 3.8 g/cm^2 per energy decade.

5.6 Summary

After 7 years of operation 1367 events passed the weather, failmode, and energy cuts. The number of data events that pass all cuts is 613. Comparisons of distributions of shower variables show very good agreement between data and reconstructed MC.

The systematic error on mean X_{max} is 16.3 g/cm^2 at 10^{19} eV. Figure 5.4a shows the overall X_{max} resolution (the bias is the mean of this distribution). The X_{max} resolution measured by proton MC is 22.5 g/cm^2, with a bias of 1.48 g/cm^2 (for iron it is 21.3 g/cm^2 with a bias of 0.98 g/cm^2). Figure 5.4b shows that the energy dependence of the resolution is fairly flat for both primaries.

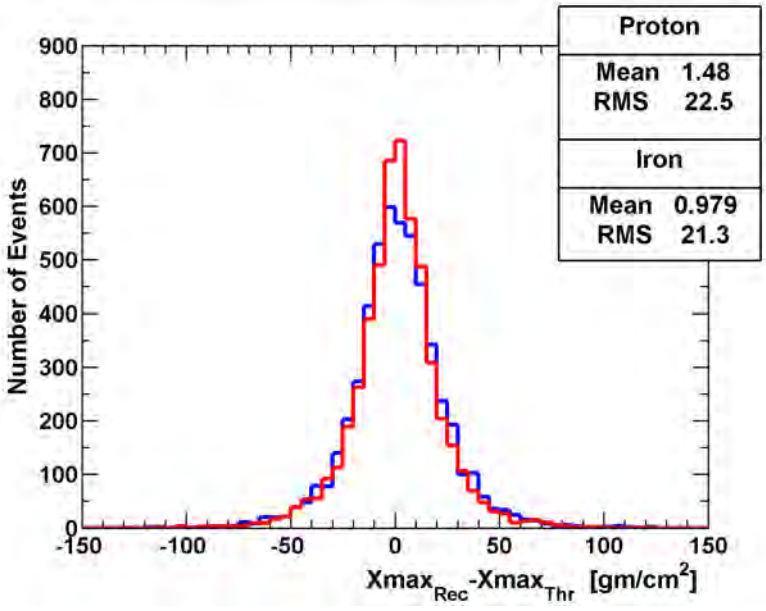

(a)

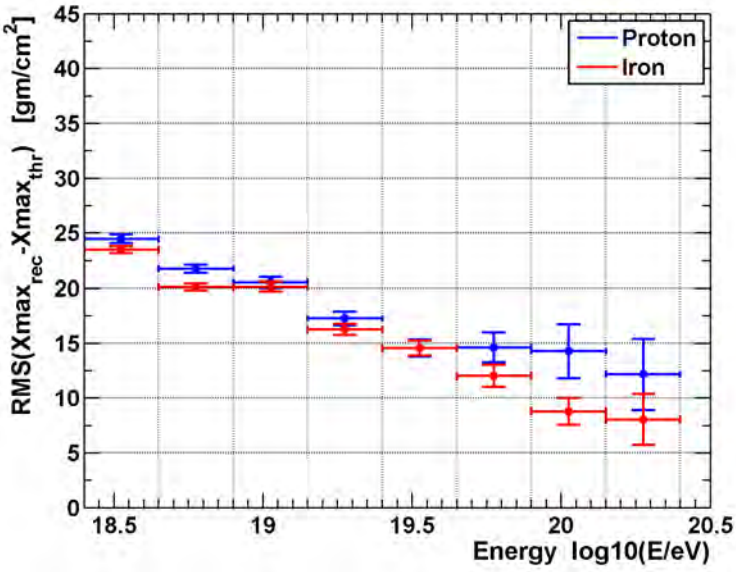

(b)

Figure 5.4: MD hybrid X_{max} resolution, above E>$10^{18.4}$ eV, for the Monte Carlo (MC) simulation sets. The resolution is the RMS difference between the reconstructed, and thrown X_{max} values, for QGSJETII-03 MC proton induced showers (blue), and iron induced showers (red). (a) Overall resolution. (b) Resolution change with energy.

PART II

ANISOTROPIES – DENSITY AND ENERGY

CHAPTER 6

ANISOTROPY INTRODUCTION

Ultra-high energy cosmic ray (UHECR) sources are still unknown, though the lack of any strong anisotropy largely rules out galactic origin ($E \geq 10^{19.0}$ eV). The probable distances of UHECR sources are composition dependent. They're likely to be $<$100 Mpc for protons and iron while intermediate mass nuclei (helium to nitrogen) are limited to $\sim$20 Mpc due to the GZK interaction [71]. Energy density within this volume limits the possible accelerators to magnetars, gamma-ray bursts, active galactic nuclei (AGN), starburst galaxies, and galaxy clusters.

Nearby AGNs are clustered around large scale structures (LSS) with a typical clustering length of 5–15 Mpc. The "supergalactic plane" is based upon the local averaged distribution of LSS. The typical density of these AGN concentrations is estimated to be a few hundred percent of the averaged density within 20° spherical cap radius circles around them [72]. This suggests that intermediate-scale anisotropy could have a similar angular scale.

This is supported by the Telescope Array (TA) 3.4σ evidence for a "Hotspot" near Ursa Major ($E \geq 57$ EeV). This study used 5 years of data and a 20° radius spherical cap sky binning [27]. The 7-year update was reported with an unchanged 3.4σ significance and used the same 20° spherical cap bin size [28]. In Chapter 8 it will be shown that the TA Hotspot now has a scale of $\sim$25°.

This thesis is an extension to lower energies and is a search for spacial differences in the energy distribution of events ($E \geq 10^{19.0}$ eV). In particular, the magnitude of possible magnetic deflection of charged particles is energy dependent and this may be exploited in the search for anisotropy. A previous attempt by PAO was a search for small-scale correlations between energy ($E>20$ EeV) and position in the sky [73]. No significant energy-distance correlations of multiplets was found.

For the anisotropy analysis in Part 2, Telescope Array (TA) surface detector (SD) data recorded between 2008 May 11 and 2015 May 11 was used. The same event reconstruction, described in Section 4, was used for the first TA "Hotspot" analysis [27], and is the same seven year time frame used for the updated Hotspot analysis [28]. SD data is used for anisotropy analyses, rather than fluorescence (FD) Hybrid FD/SD data, due to the much higher statistics of successfully reconstructed events and the larger and more uniform field-of-view (FOV).

6.1 Oversampling Anisotropy

Oversampling in regards to anisotropy analysis means that the data is binned in some manner within the FOV sky, and those bins have a large amount of overlap so that every data event is used many times, to calculate the chosen test statistic. The test statistics significance is found by applying the same method to isotropic Monte Carlo (MC) event sets made as described in Chapter 7.

A number of the oversampling methods used in this analysis are additions, or modifications, to the type of analysis that was developed by the AGASA collaboration to search for large scale anisotropy [74] [75], namely to use oversampling with a spherical cap binning on the sky exposure and estimated expected backgrounds [76] [77]. The TA and HiRes collaborations (among many others) have used similar methods previously [22] [27] [78].

6.1.1 σ Significance

The σ significances reported in this thesis are calculated using the p value, the p value being the probability of getting a result appearing as anisotropic with a sky that is actually isotropic (uniform distribution of sources). The σ significance is the area under a Gaussian distribution, with a mean of zero and standard deviation of one, for $f(x > p_{data})$ in the case of a one-sided test (if only one of two possibilities are of interest) and the integral under $f(|x| > p_{data})$ for a two-sided significance. σ is calculated using the inverse cumulative distribution function of the Gaussian $\Phi(p_{data})^{-1} = \sqrt{2}\,\mathrm{erf}^{-1}(1 - 2 \times p_{data})$ (one-sided) or $\sqrt{2}\,\mathrm{erf}^{-1}(1 - 4 \times p_{data})$ (two-sided).

The posttrial p values are found by applying the chosen oversampling method to data sized sets of isotropic MC events made as described in Chapter 7 and counting the number

that have a greater test statistic – $p_{data} = \frac{1}{N_{MC}} \sum_i^{N_{MC}} [t_i \geq t_{data}]$.

6.1.2 Declination Bias

A declination bias of the σ significance is a concern due to the fact that in an isotropic (uniform distribution) sky the expected number of events seen by the surface detector array is not in fact uniform as shown in Sections 7.5 and 8.3. The average posttrial σ significance calculated for MC trial sets should be uniform everywhere within the FOV i.e. the probability of a false positive should be the same anywhere in an isotropic sky and the probability of a false negative should be the same for any position that an anisotropy might be located at.

Therefore, the test statistics, sky binning, and oversampling grids must be chosen to account for the non-uniform detector dependence. This results in a flat histogram (divided by solid angle) of the declination positions of maximum σ_{local} significance in the MC trials used to calculate the posttrial σ significance (see Section 8.4.2).

6.1.3 Distance on a Sphere

The great circle distance (opening angle) defines the oversampling grid, the spherical cap radius for the sky binnings of Chapters 8, 9, and 11, and the distance used in Chapter 10. In terms of normal vectors this is $\Delta d_i = \arctan \frac{|n_t \times n_i|}{n_t \cdot n_i}$. This is calculated by Equation 6.1 where RA_i is the right ascension of each point and Dec_i is the declination as explained in Section 4.1.3.1.

$$\Delta d = \arccos \left[\sin Dec_1 \sin Dec_2 + \cos Dec_1 \cos Dec_2 \cos \left(RA_1 - RA_2 \right) \right] \tag{6.1}$$

6.1.4 Grid

For the Kernel Density Estimation (KDE) Hotspot of Chapter 8, the energy spectrum anisotropy of Chapter 9, and the Hot/Coldspot analysis of Chapter 11 the event sampling is done on a grid of points with a median equal opening angle spacing of $0.5 \pm 0.04^\circ$. The grid points are shown in Figure 6.1 and are found from tessellating the sphere by dividing spherical icosahedrons to minimize the variation in distances to the closest adjacent point [79]. The grid spacing was chosen as it is 1/2, to 1/3, the pointing direction uncertainty.

Previously, for TA and HiRes analyses grids of $0.1^\circ \times 0.1^\circ$ in declination and right ascen-

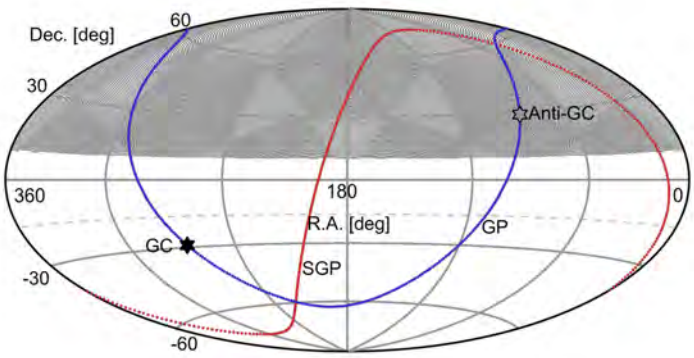

Figure 6.1: Equatorial Hammer-Aitoff projection of the equal opening angle oversampling grid. This is a grid of points with a median spacing of 0.5±0.04°. Triangle shapes visible by eye are the result of small deviations from perfect equal angles (and image aliasing) as a sphere cannot be perfectly divided into an equal grid. The dashed curve at Dec. = -16° defines the FoV.

sion were used [28]. The equal opening angle spacing ensures equal sampling of the area in the sky, instead of the sampling rate increasing with declination. This equal sampling removes one type of declination bias in MC trials maximum significance.

The equal opening angle grid spacing also allows statistical measurements to be made on the test statistic itself due to the uniform sampling (e.g. mean, RMS, etc.). These kinds of statistics are used in Section 11.3.1 for the Hot/Coldspot Summary analysis.

Though the TA field-of-view extends to -16° in declination the grid is cut at +10 declination for Chapters 9 and 11 for three primary reasons – lack of statistics, minimizing cutoff of oversampled spherical caps, and zenith angle agreement between different energies of data is improved.

6.2 Hotspot – Kernel Density Estimation

In Chapter 8 the previously reported event density Hotspot intermediate-scale anisotropy of ultra-high energy cosmic rays [28] is studied using a different method. This search is done with a new solution to the "on-off problem" of UHECR source searches using a KDE method that avoids the issue of choosing an oversampling spherical cap bin size. Chronologically, this was the last anisotropy study done in this thesis.

6.3 Energy Spectrum Anisotropy

Evidence for an energy dependent intermediate-scale anisotropy has been found in the arrival directions of ultra-high energy cosmic rays of energies above $10^{19.2}$ eV as shown in Chapter 9. In this new method the energy spectrum inside oversampled spherical cap bins of equal exposure are compared to that outside using the Poisson likelihood ratio test. Chronologically, this was the third anisotropy study done in this thesis.

The energy distribution within the center of maximum significance shows that the Hotspot excess for $E \geq 10^{19.75}$ eV is found to correspond at the same location to a lower energy deficit, or "Coldspot," of events for $10^{19.2} \leq E < 10^{19.75}$ eV. This Hot/Coldspot feature is suggestive of energy dependent magnetic deflection of the isotropic background and cosmic-rays from a source.

6.4 Energy-Distance Correlation

Evidence for an energy-distance correlation anisotropy has been found in the arrival directions of ultra-high energy cosmic rays of energies above 20 EeV. This is done using a new method described in Chapter 10. An unbinned ranked correlation is done at the location of each event; measuring monotonic trend of distance versus energy for all events with greater energy. Chronologically, this was the first anisotropy study done in this thesis.

6.5 Hot/Coldspot Summary

The combined effect of energy spectrum and energy-distance correlation anisotropies results in the discovery of the event density asymmetry anisotropy of a Hot/Coldspot shown in Chapter 11. The significance of this density asymmetry is found by applying the Li-Ma method, using oversampling bins of equal exposure ratio (used in Chapter 9), to two energy bins. Chronologically, this was the second anisotropy study done in this thesis with prior knowledge of the Hotspot and energy-distance correlation anisotropies.

CHAPTER 7

ISOTROPIC MONTE CARLO

Isotropic Monte Carlo (MC) sets, where there is no preferred direction for events to appear, are used for calculating expected backgrounds, assuming a sky with a completely uniform distribution of sources. They are also used in calculating a posttrial significance, by applying to them the same analysis as data and counting the number of sets which have a significance greater than or equal to the data.

The direction of arrival of individual MC and data events are defined by unique values of three variables – zenith angle (θ), azimuthal angle (ϕ), and detector trigger time (t). The remaining two variables, latitude and longitude, are defined as the center of the Telescope Array (TA) surface detector (SD) at 39.3 Long., -112.9 Lat. These five variables, the horizontal coordinates, are used to calculate the right ascension (R.A.) and declination (Dec.) in equatorial coordinates for each event by Equation 4.10 [65].

Energies E$\geq$10 EeV were tested (the minimum energy for which the detection efficiency is flat) for the energy spectrum anisotropy and Hot/Coldspot analyses so all the figures in this chapter use this minimum cutoff. All cuts are listed in Chapter 4.

7.1 Time

To properly take into account the exposure the detector on-time is simulated by empirical Inverse-Transform sampling. This is done by nearest-neighbor interpolation of the trigger times of 246,499 SD data events of E$\geq$0.5 EeV, with zenith angle $\theta \leq 55^{\circ}$, and that triggered at least four SDs. The ordered data trigger times are considered as an empirical cumulative distribution function (CDF) of the fraction of total events 0 to 1. A uniform distributed random number $\{n \in \Re \mid [0,1]\}$ is generated and the closest fraction is chosen – then $t_{mc} = ECDF^{-1}(nearest(n))$.

The distribution of data, E$\geq$10 EeV, trigger times compared to a set of 2×10^7 MC is in Figure 7.1. Data and MC are shown to be in agreement using the Cramér-von Mises (CvM)

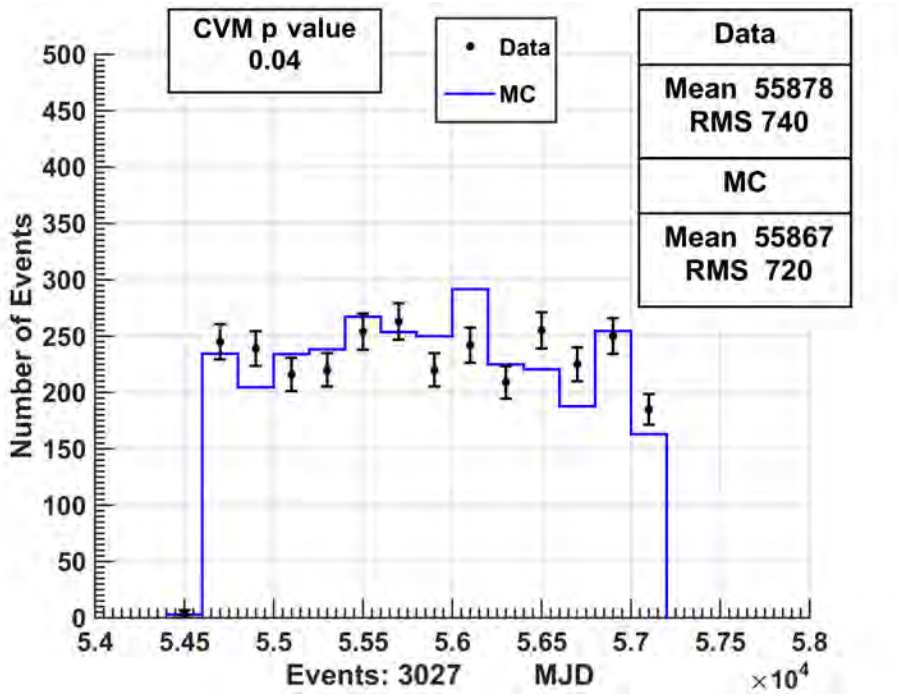

Figure 7.1: Modified Julian Date (MJD) trigger time distribution of surface detector (SD) data, with E≥10 EeV, compared to a set of 2×10^7 MC (from sampled data trigger times) are shown to be in agreement using the Cramér-von Mises (CvM) goodness of fit (GOF) test. The probability of these distributions having the same parent distribution is 4%. For E≥20 EeV it is 17%.

goodness of fit (GOF) test which is described in some detail in Appendix B. The CvM-test is an unbinned GOF test which weights equally the entire distribution [80].

It can be seen in Section 7.6 that the resulting MC R.A. equatorial coordinate, which is dependent on trigger time according to Equation 4.11 of Section 4.1.3.1, is in good agreement with data.

7.2 Azimuth

Even in the case of a significant anisotropy there should be no preferred orientation with respect to cardinal directions of the Earth's sphere, therefore the theoretical azimuthal angle distribution is a uniform distribution with a range of 0° to 360°, $\{U \in \Re \mid (0, 360]\}$. This is generated by a uniform distribution random number n from 0 to 1 – then $\phi = 0.001 + n(360 - 0.001)$.

The azimuth distribution of data, E≥10 EeV, compared to a 2×10^7 event MC set is in Figure 7.2a. They are in very good agreement according to the CvM-test.

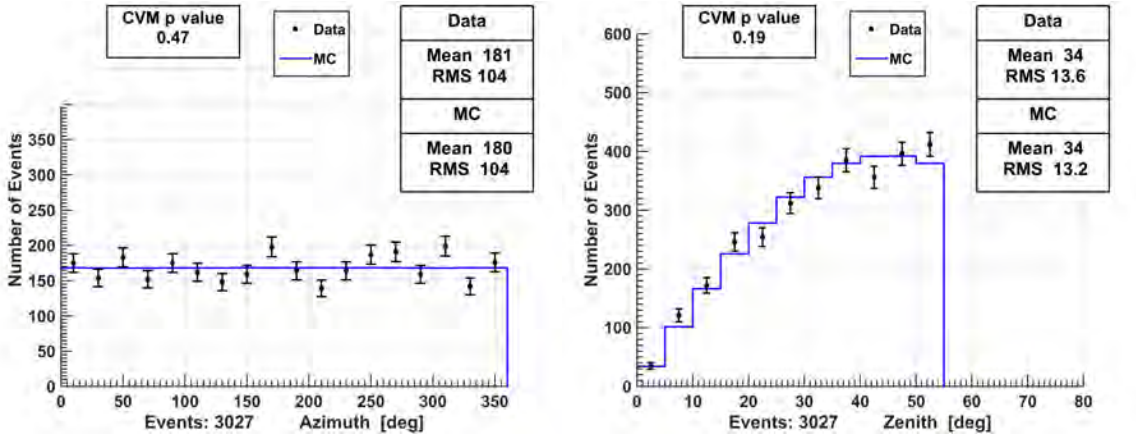

(a) (b)

Figure 7.2: Azimuthal, and zenith, angle distributions of SD data (with E≥10 EeV), compared to sets of 2×10^7 isotropic MC, are shown to be in very good agreement using the CvM-test. (a) Azimuthal angle, ϕ, distribution compared to the uniform MC distribution. The probability of these distributions having the same parent distribution is 47%, for E≥20 EeV it is 75%. (b) Zenith angle, θ, distribution compared to the MC with a g(θ) = $\sin(\theta)\cos(\theta)$ distribution. The probability of these two distributions having the same parent distribution is 19%, for E≥20 EeV it is 28%.

7.3 Zenith

The zenith angle, θ, distribution of events is g(θ) = $\sin(\theta)\cos(\theta)$ due to the geometry of a uniform spherical pointing direction distribution sampled by a flat detector. $\sin(\theta)$ is a spherically isotropic distribution and $\cos(\theta)$ is the projection of the distribution on the flat SD array.

The Inverse-Transform Sampling method is used to create this distribution for angles from 0° to 55°, as this is the range of the data cuts. The CDF is $CDF(\theta) = 1.49\sin(\frac{\pi}{180}\theta)^2$, $0°\leq\theta\leq55°$. A uniform distribution random number n from 0 to 1 is generated – then $\theta_{MC} = \frac{180}{\pi}\sin^{-1}(0.819\sqrt{n})$.

The zenith distribution of data, E≥10 EeV, and a 2×10^7 event MC set, are shown to agree very well in Figure 7.2b.

7.4 Energy

Detector acceptances and biases in the energy spectrum are taken into account by using a large set of MC events reconstructed, as in Chapter 4 with the changes of Section 5.1, through the surface detector simulation generated with the fitted HiRes spectrum as de-

scribed in Chapter 2.3.6 [14] [53].

The same cuts applied to the data are applied to these simulated MC events. The piece-wise power law used is $E^{-2.81}$ for $E<10^{19.75}$ eV and $E^{-5.1}$ for $E\geq10^{19.75}$ eV. There are 386,125 MC events with $E\geq10^{19.0}$ eV, 250,742 $E\geq10^{19.1}$ eV, 112,405 $E\geq10^{19.2}$ eV, and 103,912 $E\geq10^{19.3}$ eV. These are sufficient sample sizes for accurate linear interpolation to generate all intermediate energies.

The empirical Inverse-Transform sampling method is used by linear interpolation of the sorted energies as a function of the fraction of total events. A uniform random number n from 0 to 1 is generated and the linear interpolation approximates what the energy would be at that fraction if there were an infinite number of MC. Therefore, the energy is $E_{mc} = interp(CDF^{-1}(n))$. Any resulting energies of $E\geq10^{20.35}$ eV are re-thrown, as the highest energy in the data set is 20.32 $\log_{10}(E/eV)$.

In Figure 7.3 the energy distribution of data, E≥10 EeV, is compared to a 2×10^7 event MC set and is shown to be in very good agreement.

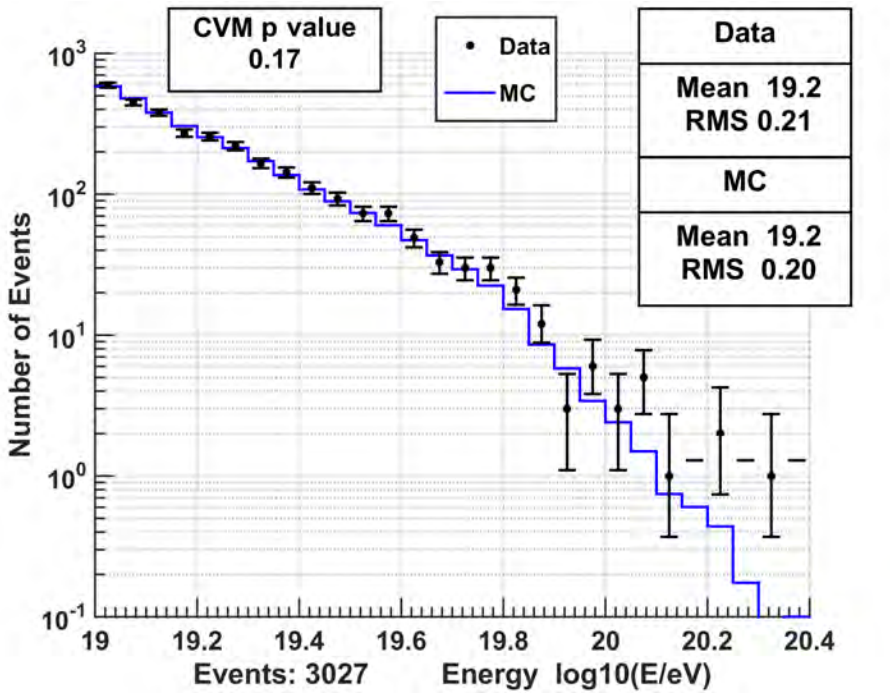

Figure 7.3: Energy distribution of SD data, E≥10 EeV, compared to a set of 2×10^7 isotropic MC with the SD reconstructed HiRes spectrum distribution, are shown to be in very good agreement using the CvM-test. The probability of these distributions having the same parent distribution is 17%. For E≥20 EeV it is 19%.

7.5 Declination

The MC declination distribution is calculated, by Equation 4.11, using the zenith, and azimuth, angles above. Figure 7.4a shows that the declination (Dec.) equatorial coordinate of SD data, E≥10 EeV, compared to a 2×10^7 event MC set are in very good agreement.

The peak of the distribution is due to the center of the TA SD location of 39.3 Latitude. The shape of the decrease of events on either side is due to the zenith $\sin(\theta)\cos(\theta)$ distribution rotated around the uniform azimuth distribution as the field of view rotates through the RA coordinate.

7.6 Right Ascension

The MC right ascension (R.A.) distribution is calculated, by Equation 4.10, using the declination, zenith, azimuth, and trigger time distributions above. The R.A. distribution shown in Figure 7.4b should be fairly uniform, except for nonuniformities cause by detector on-time, or anisotropies in the data.

Anisotropies are most likely to appear in the R.A. distribution as each bin is averaged over 110 degrees of declination whereas the Dec. distribution is averaged over 360 degrees of R.A. for each bin. This may be demonstrated by Figure 7.4b where the probability of the

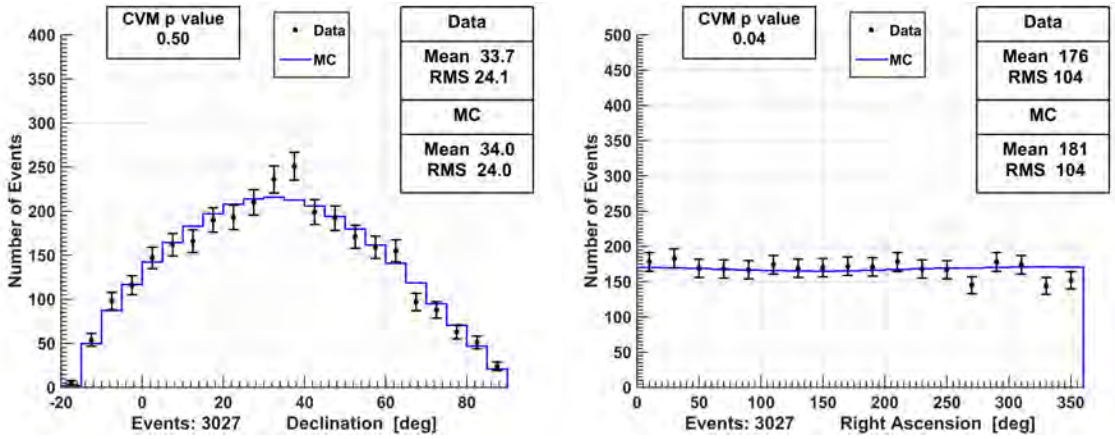

(a) (b)

Figure 7.4: Equatorial declination (Dec.), and right ascension (R.A.), coordinate distributions of SD data (with E≥10 EeV), compared to sets of 2×10^7 isotropic MC, are shown to be in very good agreement using the CvM-test. (a) Dec. coordinate distribution comparison. The probability of these distributions having the same parent distribution is 50%, for E≥20 EeV it is 64%. (b) R.A. coordinate distribution comparison. The probability of these distributions having the same parent distribution is 4%. For E≥20 EeV it is 48%.

data and the MC coming from the same parent distribution is 4%. A 4% p-value agreement between R.A. of data and MC could also simply be a random fluctuation that should be expected when doing a lot of comparisons

To be confident there is not any large flaw in the MC R.A. generation Figure 7.5 shows a representative MC the size of data compared to a completely uniform distribution. The CvM-test p value of 0.5 shows they are in very good agreement.

7.7 Summary

Each set of three variables (energy, R.A., and Dec.), either the same sample size as data for posttrial significance calculation, or much larger sets of events for background estimation – is an isotropic MC set that simulates the expected data given the detector configuration, and on-time, with the assumption of no anisotropies. Distributions of these variables have been shown to agree with SD data and the expected distributions.

The resulting geometrical exposure, which is the number of events expected inside a spherical cap sky binning, increases with declination. This is due to the declination distribution of Figure 7.4a, and the fact that as declination increases the differential area around the R.A. decreases. This is discussed further in Chapter 8.

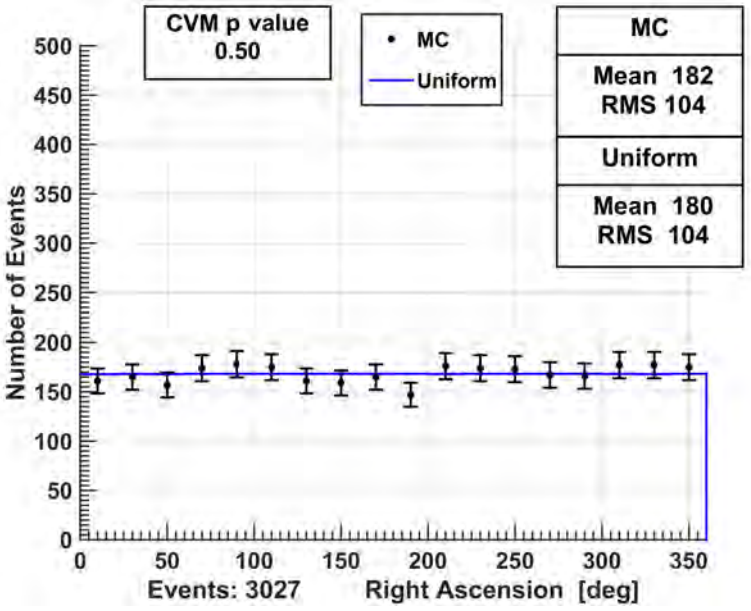

Figure 7.5: R.A. distribution of an example MC, same size as the data set, compared to a uniform distribution are in very good agreement using the CvM-test. The probability of these distributions having the same parent distribution is 50%.

CHAPTER 8

HOTSPOT – KERNEL DENSITY ESTIMATION

An event excess ("Hotspot") search is done using a new Kernel Density Estimation (KDE) method. The resulting center of maximum significance is at 149° R.A. 44° Dec. The global posttrial one-sided probability of the measured excess, appearing by chance anywhere on an isotropic sky, is found by Monte Carlo simulation to be 1.3×10^{-4} (3.65σ).

Studies of intermediate scale cosmic ray or gamma ray anisotropy are normally done using statistics defined by the "on-off problem." It is a counting problem that is a search for a particle source, where there is a background signal, and the total counts expected are only a fraction of the background plus possible source signal events. The question being: Is there a source signal in the presence of a random background when accounting for detector bias?

Instead of counting possible signal events, at a single point in the sky and immediately calculating its final significance, intermediate scale UHECR anisotropy studies have generally used the statistical methods of gamma ray astronomy and applied them to a grid covering all points within the particular detectors field-of-view (FOV). This oversampling method changes any pretrial statistical significance to a "test statistic" which requires the use of Monte Carlo (MC) methods to calculate a final true significance of the measurement. The different statistical methods available are rated for accuracy by MC calculation so this produces good results [81]. Since this is the case it is not crucially important that a pretrial test statistic (the significance given to a point in the sky by any particular statistical method) be a true Gaussian significance – what matters is whether the statistic is unbiased in regards to the exposure of the detector and is sensitive to a signal.

The downside to these statistical methods is that the size of the sky binning, in which counting events is done, must be scanned to maximize the chosen test statistic and the resulting penalty factor accounted for in the MC trials. This is in addition to the penalties

caused by other necessary cuts such as an energy threshold.

The new method suggested in this chapter avoids the bin size problem by *a priori* reasoning. The goal is to accurately estimate the underlying population probability density function (PDF) using the given sample of events – not to maximize a pretrial significance. This is done by kernel density estimation (KDE) which is a non-parametric smoothing method that makes inferences about the population [82]. The final posttrial significance is found by applying the same method to isotropic MC sets.

It is shown that the KDE method is relatively detector exposure unbiased compared to the very common Li-Ma statistic (discussed further in Section 8.4) while avoiding the *a posteriori* choosing of oversampling bin size to maximize the pretrial test statistic. It is also more robust with regard to low statistics and to different cuts on the data.

8.1 Energy Threshold

An energy threshold of 57 EeV is used to avoid a free parameter as this was used for the TA "Hotspot" analysis and corresponds to the lower energy threshold determined by the AGN correlation results from PAO [25] [27] [28].

The event reconstruction and other cuts are described in full in Chapter 4. After cuts, there are 84 events with E$\geq$57 EeV. This is fewer events than the previously presented 7 year Hotspot result due to the tighter cuts used for all analysis in this thesis [28]. An equatorial coordinate sky map of the events is shown in Figure 8.1. For calculating posttrial significances isotropic Monte Carlo (MC) sets are created, as described in Chapter 7, with 84 events.

8.2 Method

8.2.1 Spherical KDE

A kernel density estimation (KDE) is essentially a normalized weighted histogram where the events are weighted by their distance from the bin center. It is normalized so that the result integrates to one as it is an approximation to the population PDF. The general form of a KDE for spherical data is shown in Equation 8.1 [83]. It is a superposition of PDF's originating at each bin center, in this case the grid described in Section 6.1.4.

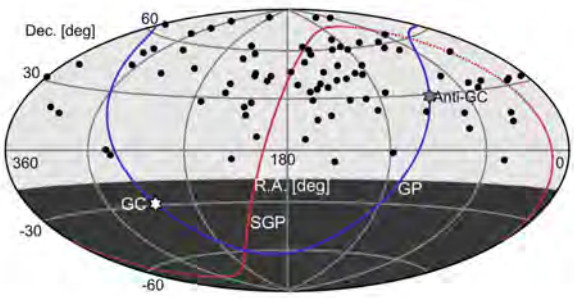

Figure 8.1: Equatorial Hammer-Aitoff projection of the 84 UHECR events in the data set with E≥57 EeV observed by the TA SD array. There is a visible excess of events near the location of the previously reported "Hotspot" 147° R.A., 43° Dec. The dashed curve at Dec. = -16° defines the FoV. Solid curves indicate the galactic plane (GP) and supergalactic plane (SGP). White and grey hexagrams indicate the galactic center (GC) and galactic anticenter (Anti-GC).

$$\hat{f}_L(\vec{\mathbf{x}}, \lambda) = \frac{d_0(\lambda)}{N} \sum_{i=1}^{N} L\left(\lambda(1 - \vec{\mathbf{x}}^{\mathsf{T}}\vec{\mathbf{x}}_i)\right) \tag{8.1}$$

Here L is the kernel function, λ is the smoothing parameter, N is the total number of events in the data set, $\vec{\mathbf{x}}$ is the grid point bin center, $\vec{\mathbf{x}}_i$ is the position of the i_{th} data point, d_0 is a normalization chosen so that $\hat{f}_L$ integrates to one. In the 1-d case a common choice for the kernel function is a Gaussian, and as anisotropy studies take place on the surface of a sphere, the 2-sphere Gaussian analog is used. This is the von Mises-Fisher probability distribution and is shown in Equation 8.2 for the 2-sphere case.

$$L = \frac{\kappa}{4\pi \sinh(\kappa)} \exp(\kappa \vec{\boldsymbol{\mu}}^{\mathsf{T}}\vec{\mathbf{x}}_i) \tag{8.2}$$

κ is the concentration parameter (how concentrated the distribution is), μ is the mean direction, and x_i is the sample point [84]. The resulting KDE is shown in Equation 8.3. The integral of this function is normalized, by a, to one which is simply approximated on the sampling grid within the field-of-view by summing the prenormalized value at all grid points.

$$\hat{f}(\vec{\mathbf{x}}, \kappa) = \frac{1}{a} \sum_{i=1}^{N} exp\left(\kappa(\vec{\mathbf{x}}^{\mathsf{T}} \vec{\mathbf{x}}_i) - 1\right) \tag{8.3}$$

This changes the question of the spherical cap bin size in the case of the "on-off problem" to a choice of the smoothing parameter, κ. The function to calculate the optimal value to get the best approximation to the population PDF was found by minimizing the asymptotic mean integrated squared error (AMISE) and is a function of a first estimate of κ, that is $\hat{\kappa}$ [85] [86]. This is the minimization of $\int E(\hat{f} - f)$ for $N \to \infty$ where f is the true population probability density function. Equation 8.4a shows this result, where the ν_j are modified Bessel functions of the first kind.

Since the exposure of the surface detector is not uniform in declination, as shown in Figure 7.4a, but is fairly uniform in R.A., as shown in Figure 7.4b, the initial estimate $\hat{\kappa}$ is made using the circular wrapped Gaussian distribution case (for which the circular von Mises distribution is a very good approximation). Equation 8.4b is this first estimate where S is the circular angular deviation [87].

$$\kappa = \frac{N\hat{\kappa}^2[3\nu_2(2\hat{\kappa})\nu_0(2\hat{\kappa}) + \nu_1(2\hat{\kappa})^2]}{(4\sqrt{\pi}\nu_0(\hat{\kappa})^4)^{1/3}} \tag{8.4a}$$

$$\hat{\kappa} = \left(\frac{3}{4}N\right)^{2/5} S^{-2} \tag{8.4b}$$

Applying Equation 8.3 to data (and isotropic MC) calculates the estimated population PDF of the data (and population background PDF of uniform sources). These two PDFs are used to calculate a test statistic at each grid point, for which MC trials the size of data are tested, to find the posttrial global significance of data event clustering. Calculating the background can be done in two ways – by finding the average κ of data sized MC sets and applying that smoothing parameter to a very large MC set (2×10^7) or using the κ found for each data sized MC set and taking the average of many PDFs. The scale of smoothing should be on the same order as the data. The resulting posttrial significance has been calculated by both methods and found to be the same.

8.2.2 Test Statistic

A proper test statistic should result in a declination unbiased result. This is a concern as due to detector geometry the detector itself is declination biased. To create an unbiased test

statistic the data PDF and background PDF are converted to a pretrial "instantaneous σ" significance at every grid point using the binomial proportion test (aka Wald's Test). This is shown in Equation 8.5 [88]. This treats each grid point as a small bin where the proportion of events expected inside has been approximated by the KDE for both the data and expected background (all sample sizes are set to N=1). This gives the two-sided test statistic of $p \neq p_{bg}$. Grid points with $p < p_{bg}$ are set equal to zero as only excess events are of interest.

$$Z = \frac{\hat{p} - p_{bg}}{\sqrt{\hat{p}(1-\hat{p})}} \tag{8.5a}$$

$$\hat{p} = \frac{p + p_{bg}}{2} \tag{8.5b}$$

Alternatives such as the Score test (which is usually considered superior to Wald's [89]), log-likelihood ratio $-2\log p/p_{bg}$, simple ratios, subtraction, $p/\sqrt{p_{bg}}$ etc., all resulted in a more biased declination dependence. The declinations of the MC sets maximum "instantaneous σ" test statistic are shown in Section 8.4.2 and compared to the bias of the Li-Ma significance [76] [77]. Li-Ma significance is explained further in Section 8.4.

8.3 Result

The isotropic background PDF, p_{bg}, calculated with 2×10^7 MC events is shown in Figure 8.2a. This shows the estimated probability to find an event at every grid point in Figure 6.1 assuming an isotropic sky. The smoothing parameter found from the average of Equation 8.4 is $\kappa = 9.8$.

By also applying the method in Section 8.2 to the data events shown in Figure 8.1 the estimated population probability density function (PDF), p, of the data is calculated. The smoothing parameter found from Equation 8.4 is $\kappa = 16.6$. This data PDF shown in Figure 8.2b.

The resulting binomial proportion test statistic, "instantaneous σ", found by applying Equation 8.5 to p_{bg} (Figure 8.2a) and p (Figure 8.2b) is shown in Figure 8.3. This is proportional to the final posttrial significance found from MC trials. The Hotspot at 149° R.A., 44° Dec. is clearly visible.

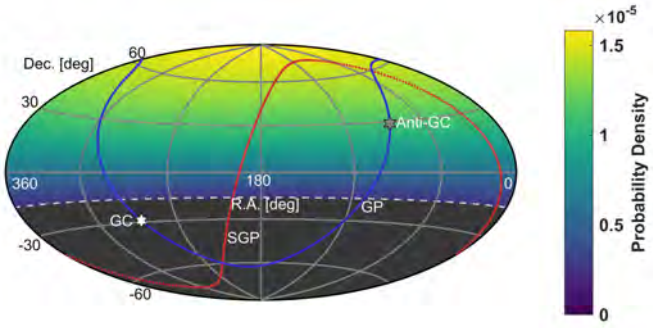

(a)

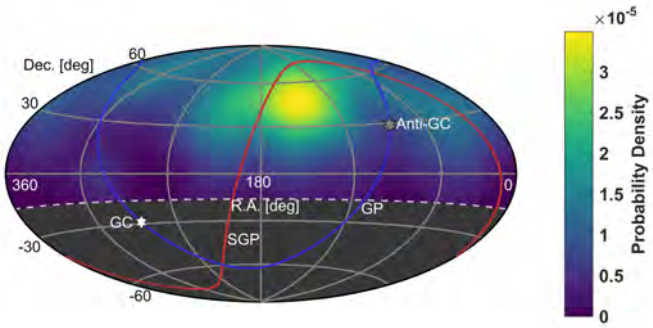

(b)

Figure 8.2: Projection of the UHECR isotropic expected background, and data, probability density functions (PDFs) given by kernel density estimation (KDE). (a) Estimated probability to find an event at every grid point assuming an isotropic sky. (b) Estimated probability to find an event at every grid point given the distribution of the actual data.

8.3.1 Global Significance

To calculate the global posttrial significance the method of Section 8.2 is applied to 2.5×10^6 sets of isotropic Monte Carlo simulations, as described in Chapter 7, with 84 events like the data. Each MC set has its own smoothing parameter, κ, calculated by Equation 8.4b. Then the "instantaneous σ" is calculated using the same background PDF, p_{bg}, by Equation 8.5. The maximum σ_{inst} at any grid point is considered for counting MC sets which have a higher value than the data, $\sigma_{inst}\geq0.00226$.

These 2.5×10^6 sets of maps are used to calculate the posttrial global significance and the empirical probability distribution function of these isotropic MC maximum σ_{inst}'s is shown in Figure 8.4a.

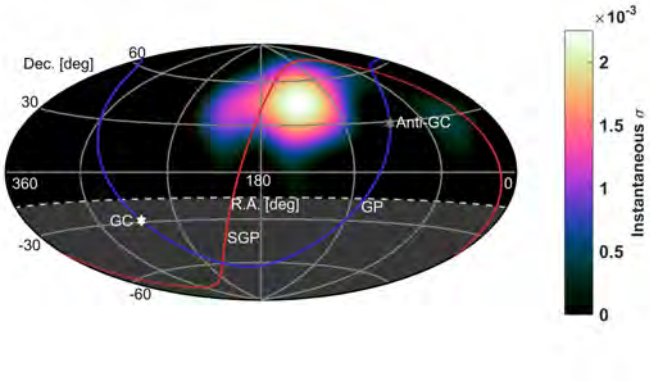

Figure 8.3: Projection of the UHECR data "instantaneous σ" test statistic from the Wald binomial proportion test applied to the data PDF and the expected background PDF. This is proportional to the final posttrial significance found from MC trials. The Hotspot at 149° R.A. 44° Dec. is clearly visible and has a maximum $\sigma_{inst} = 0.00226$.

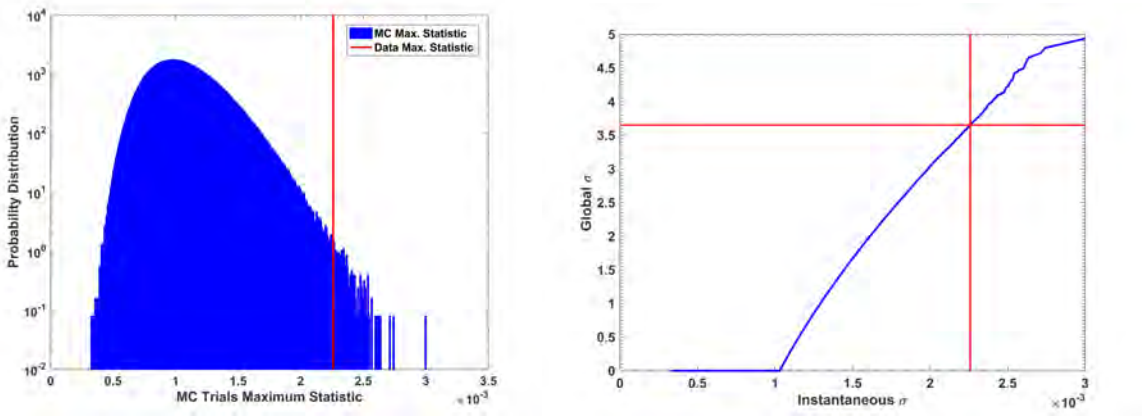

(a) (b)

Figure 8.4: MC trial maximum "instantaneous σ" distribution and the conversion to posttrial significance. (a) Maximum "instanteous σ" PDF for 2.5×10^6 MC trials. The area above the data, $0.00226\sigma_{inst}$, gives a 3.65σ global posttrial one-sided significance for the Hotspot excess. (b) Resulting significance survival function calculated, from (a), that returns the global posttrial significance, σ, given a test statistic, σ_{inst}. Red lines are the data result.

Figure 8.4a allows the derivation of a function which returns the posttrial global significance for any given local pretrial σ_{inst} from the one-sided p value of the empirical complementary cumulative distribution (or survival function). This function is shown in Figure 8.4b. This local pretrial to global posttrial conversion can be applied to every point on the grid and is shown in Figure 8.5. This shows that the area of significance is roughly $\sim$15° in radius.

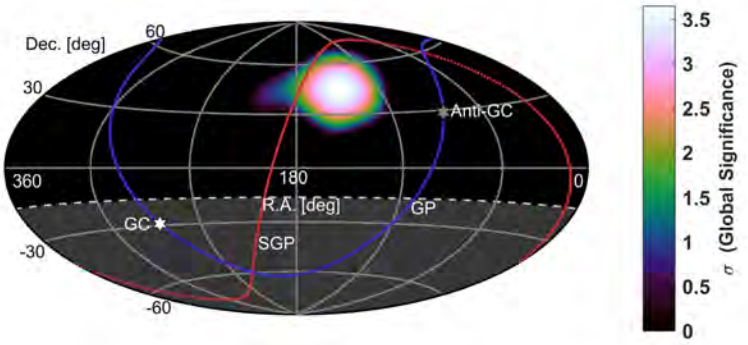

Figure 8.5: Projection of the global posttrial one-sided Hotspot anisotropy significance using KDE. The maximum significance is 3.65σ at 149° R.A., 44° Dec. This is 2° from the previously published Hotspot location that used Li-Ma statistics and looser cuts [28].

There were 326 MC out of 2.5×10^6 MC which had a higher "instantaneous σ" than $0.00226\sigma_{inst}$. This corresponds to a global posttrial one-sided significance of 3.65σ which is visible in Figure 8.5 as the maximum at 149° R.A., 44° Dec. This is 2° from the previously published Hotspot location [28].

8.4 Comparison to Li-Ma Significance

The most popular solution to the "on-off problem" problem is the Li-Ma significance (it is also known as the "Li-Ma problem") which is the combination of two Poisson likelihood ratios and takes into account that a signal may be present [76] [77]. A review of the various test statistics in use is given in [81], and [90].

The Li-Ma two-sided significance of an excess/deficit of events is shown in Equation 8.6. It is multiplied by the factor $sign(N_{on} - N_{bg})$ which means that deficits of events are given negative significances. N_{on} is the number of events inside the spherical cap bin and N_{off} the number of events outside. The spherical cap bin size radius is the great circle distance as described in Section 6.1.3. The exposure ratio, α, is calculated using a 2×10^7 isotropic Monte Carlo event set and describes the geometrical detector response discussed in Section 6.1.2 [77].

$$\sigma_{LM} = \sqrt{2}\left[N_{on} ln\left(\frac{(1+\alpha)N_{on}}{\alpha(N_{on}+N_{off})}\right) + N_{off} ln\left(\frac{(1+\alpha)N_{off}}{N_{on}+N_{off}}\right)\right]^{1/2} \tag{8.6a}$$

$$\alpha = N_{on}/N_{off} \text{ by Monte Carlo Estimation} \tag{8.6b}$$

$$N_{off} = N_{events} - N_{on} \tag{8.6c}$$

$$N_{bg} = \alpha N_{off} \tag{8.6d}$$

The Li-Ma method was applied to the same data set, using the same grid, as Section 8.3. The pretrial significance was maximized by a spherical cap bin size of 25°. A scan of bin sizes 15°, 20°, 25°, 30°, and 35° was done. The exposure ratio, α, (Equation 8.6b) is shown in Figure 8.6a for the 25° bin size. The number of events inside each spherical cap bin is shown in Figure 8.6b and the estimated background, N_{bg}, (Equation 8.6d) is shown in Figure 8.6c. The resulting pretrial two-sided Li-Ma significance found by Equation 8.6, and multiplied by $sign(N_{on} - N_{bg})$, is shown in Figure 8.6d. Figure 8.6d is the test statistic and can be compared to the KDE test statistic in Figure 8.3.

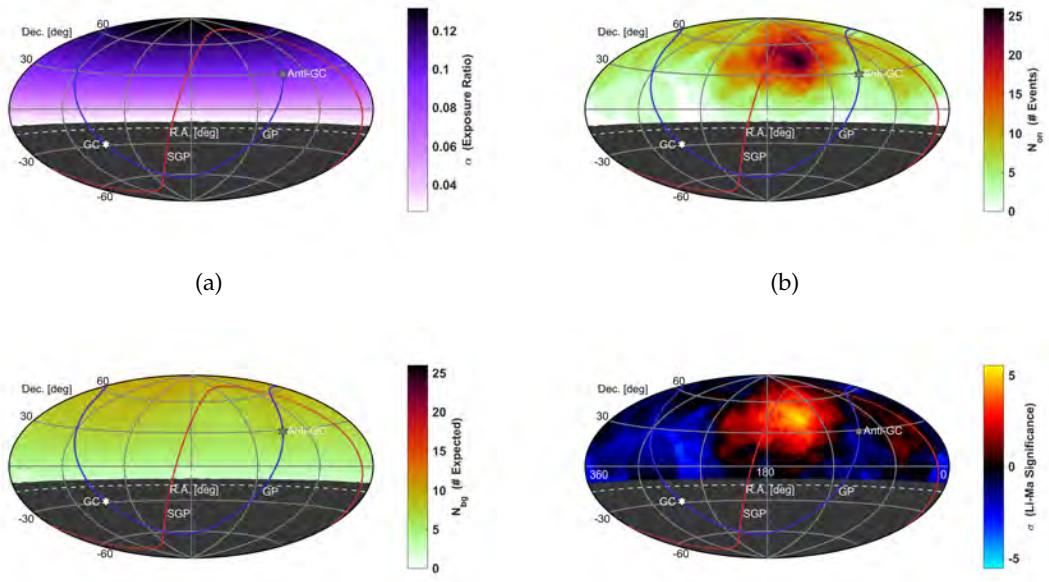

Figure 8.6: Projections of UHECR statistics used to calculate Hotspot significance using the Li-Ma method. (a) Exposure ratio α (Equation 8.6b) calculated with a 2×10^7 isotropic MC set. (b) Number of observed events, N_{on}, inside 25° radius bins. (c) Number of background events estimated from the geometrical exposure and measured data inside each bin (the same color scale as (b) is used for comparison). $N_{bg} = \alpha(N_{events} - N_{on})$. (d) Local Li-Ma two-sided significance map calculated from (a), (b) and (c) multiplied by $sign(N_{on} - N_{bg})$.

Figure 8.7 shows the pretrial two-sided Li-Ma significance from Equation 8.6 converted to a posttrial one-sided significance of a Hotspot for each grid point. This is found by applying the Li-Ma method to 2.5×10^6 isotropic MC sets, scanning each one with the same bin sizes, and counting the number with a $\sigma_{MC}\geq\sigma_{LM}$ for each grid point. This can be compared to the KDE result of Figure 8.5.

The maximum Li-Ma significance is $5.54\sigma_{LM}$ which translates to a global posttrial 3.66σ at 144° R.A., 41° Dec. The KDE method had a maximum of 3.65σ at at 149° R.A. 44° Dec. These two maxima are 5° apart and the significances are in very good agreement.

8.4.1 Stability

Table 8.1 shows the Li-Ma and KDE posttrial one-sided significance for 5 to 7 years of data. This table also shows a comparison of the significance using the original Hotspot analysis loose cuts and the tighter cuts used in this thesis [27]. It can be seen that if the Li-Ma bin size is allowed to change each year *post priori* to maximize the significance then it agrees well with the KDE σ for the loose set of cuts. Again, the KDE smoothing parameter is calculated by Equation 8.4b for a better estimate of the PDF and not to maximize its test statistic and the background is not even taken into account. The Li-Ma significance generally returns a lower significance using the tighter cuts and seems more dependent on statistics. The KDE method shows much better agreement between the two sets of cuts.

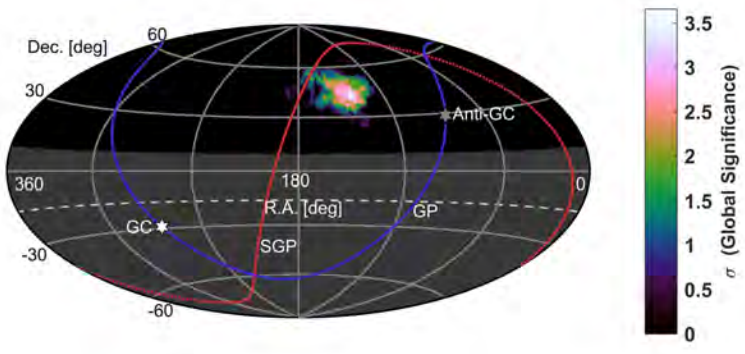

Figure 8.7: Projection of the global posttrial one-sided Hotspot anisotropy significance using the Li-Ma method. The maximum significance is 3.66σ at 144° R.A., 41° Dec. This is 5° from the previously published Hotspot location that used Li-Ma statistics and looser cuts [28].

Table 8.1: Li-Ma and KDE Significance: Years and Cut Comparison

Year	Cut	Li-Ma σ	Li-Ma Bin Size	KDE σ
5	Loose	3.52	20°	3.74
5	Tight	2.81	20°	3.52
6	Loose	4.20	20°	4.21
6	Tight	3.68	25°	4.24
7	Loose	3.72	25°	3.67
7	Tight	3.66	25°	3.65

8.4.2 Declination Bias

Figure 8.8 shows histograms of the declination of MC trial maximum test statistics for Li-Ma and KDE methods. They show number of counts in each bin divided by the solid angle covered by that bin. The KDE method compares favorably to Li-Ma and is better able to handle the low statistics at low declination. This allows the use of the KDE method grid down to -10° Dec. while the spherical cap binned methods require the grid to stop at +10° Dec.

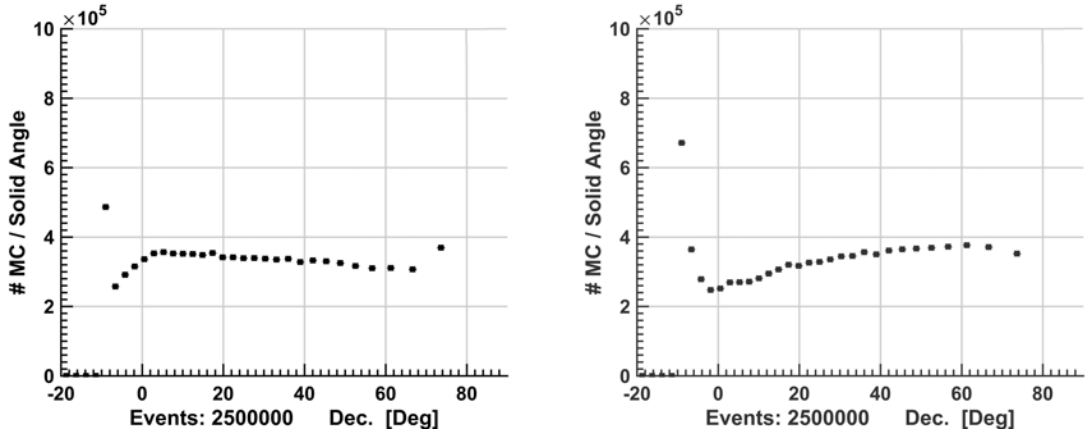

(a) (b)

Figure 8.8: Declination binned histograms (divided by solid angle) of the declination of MC trial maximum test statistics for the KDE and Li-Ma methods. (a) KDE method. (b) Li-Ma method.

CHAPTER 9

ENERGY SPECTRUM ANISOTROPY

A relative energy spectrum anisotropy search is done by comparing the energy distribution inside bins of equal exposure to that outside using the binned Poisson likelihood ratio test. The resulting center of maximum significance is at 139° R.A., 45° Dec. and has a pretrial one-sided significance of $6.17\sigma_{local}$. The energy distribution within the center of maximum significance shows that the "Hotspot" excess for $E \geq 10^{19.75}$ eV is found to correspond to a lower energy deficit, or "Coldspot," of events for $10^{19.2} \leq E < 10^{19.75}$ eV. This result is compared with the more common anisotropy statistical test of Li & Ma in Section 9.3.2 [76]. This Hot/Coldspot feature is suggestive of energy dependent magnetic deflection of the isotropic background and cosmic-rays from a source. The Hot/Coldspot is discussed further in Chapter 11.

The global posttrial one-sided probability of the $6.17\sigma_{local}$ energy spectrum anisotropy, appearing by chance anywhere on an isotropic sky, is found by isotropic Monte Carlo (MC) simulation to be 9.28×10^{-5} (3.74σ).

9.1 Method

9.1.1 Energy Distribution Comparison Test

To calculate the significance of a localized deviation in the energy spectrum the binned Poisson likelihood goodness of fit (GOF) statistical test [91] [92] is used to compare the data distribution inside spherical cap bins to the distribution of all data outside the cap. This test was used previously by Telescope Array (TA) in a composition paper for comparing X_{max} distributions [68]. It is a GOF test that allows a low number of events in each energy bin, for both the observed (N_{on} inside the spherical cap bins) and the expected (N_{bg} normalized events outside) energy distributions.

Equation 9.1 shows this test in terms of observed energy histogram bin frequencies, n_i, and expected bin frequencies, μ_i. The local pretrial σ_{local} significance is calculated by

approximating the Poisson likelihood ratio as a $-\chi^2/2$ with degrees-of-freedom $dof = \#bins + 2$. The two additional degrees of freedom come from the estimated background calculation and the combining of low statistic expectation energy bins, μ_i, as described below (this was verified by MC simulation).

$$\chi^2 \simeq 2\sum_i \mu_i - n_i + n_i ln(n_i/\mu_i) \tag{9.1a}$$

$$N_{on} = \sum_i n_i \tag{9.1b}$$

$$\alpha = N_{on}/N_{off} \text{ by MC Estimation} \tag{9.1c}$$

$$N_{bg} = \sum_i \mu_i = \alpha(N_{events} - N_{on}) \tag{9.1d}$$

The possibility of a low count number in an energy bin is due to the overall low number of events in the data set, the power law distribution of the average energy spectrum. There is also the necessity of minimizing the energy bin sizing as the local energy distribution deviations may have a change in number of events that is faster than a power law.

The *a priori* choice of energy binning is based on the energy resolution of the detector. It is chosen to be slightly smaller than the average resolution for energies $10^{19.0} \leq E < 10^{20.4}$ eV. This results in an energy bin width of 0.05 $\log_{10}(E/eV)$.

If the *expected* number of events in an energy bin is less than 1 ($\mu_i < 1$) it is combined with adjacent bins. The resulting smallest energy bin expectations are greater than 2 ($\mu_i > 2$), for which it can be calculated that the bias from approximation to a χ^2 is less than 15%, and drops to 5% at expectations of 5 events for that bin [93]. This test is discussed at length in Appendix A. This small bias is present at all grid points on the map, and also present in the MC trials when calculating the global posttrial significance.

The *expected* energy distribution is defined as the histogram of events outside the spherical cap bin (N_{off}) normalized to the expected number of events inside the cap bin (N_{bg}). The expected number of events inside the cap bins is calculated using the method of Li and Ma [76]. At each point of the oversampling grid the exposure ratio, Equation 9.1c, is calculated from a set of 5×10^7 isotropic MC events. The background calculated from the data is $N_{bg} = \alpha N_{off}$, Equation 9.1d, and therefore varies depending on the number of data N_{on} inside each spherical cap bin [77].

The posttrial significance calculation, by MC trials, takes into account that the lower bound energy threshold is a free parameter. Low energy thresholds of E$\geq 10^{19.0}$, $10^{19.1}$, $10^{19.2}$, and $10^{19.3}$ eV were tested to maximize the data pretrial significance. The maximum significance was found with a threshold of $10^{19.2}$ eV. This is a free parameter that the posttrial significance calculation takes into account as described in Section 9.2.3.

The lowest energy threshold, $10^{19.0}$ eV, is the minimum energy for which SD acceptance efficiency is $\sim$100%. Statistics above $10^{19.4}$ eV are not sufficient for an energy spectrum anisotropy analysis with only 546 events total – that must be separated into spherical cap bins and further separated into energy bins. According to [37] $10^{19.3}$ eV is the theoretical upper bound of galactic iron, so there may be some small amount of galactic contamination.

9.1.2 Equal Exposure Binning

There is a sample size bias in distribution tests of flux such as χ^2's, and likelihood ratios, that create a declination bias in the calculated significances if the sample size changes with declination. Due to the geometrical zenith angle exposure g(θ) = sin(θ)cos(θ) just such a bias is created if the spherical cap bin sizes are constant, as was the case in previous "Hotspot" anisotropy analyses [27] [28].

The spherical cap bin size radius is the great circle distance, in terms of normal vectors $\Delta d_i = arctan\frac{|n_t \times n_i|}{n_t \cdot n_i}$. This is the same distance that defines the spherical cap binning of Chapters 8 and 11, and the distance used in Chapter 10. Here an equal exposure radii binning is adopted such that at each point of the equal opening angle oversampling grid the MC calculated exposure ratio, $\alpha = N_{on}/N_{off}$, is a constant value.

A 2×10^7 MC event set was used in the three parameter fit of the spherical cap bin sizes on the grid, the average spherical cap bin size (15.0°, 20.0°, 25.0°, and 30.0°), and the resulting constant α ratio. After the nominal bin sizes were found for each exposure ratio, α, a map of α was calculated using a set of 5×10^7 MC. This is to account for any remaining small variations from the bin size fit. This is the final value used in Equation 9.1d.

Exposure ratios of 3.35%, 6.04%, 9.58%, and 14.03% were tested to maximize the data pretrial significance (these ratios result in spherical cap bin size averages of 15.0°, 20.0°, 25.0°, and 30.0°). The maximum significance was found with an exposure ratio of 14.03%.

This is a free parameter that the posttrial significance calculation takes into account as described in Section 9.2.3.

Figures 9.1a and 9.1b show the constant exposure ratio binning of $\alpha = 14.03\%$ (or 30° average spherical cap bin size). Figure 9.1a shows the spherical cap bin sizes at each grid point. The resulting very small variation in α, displayed in the range that would be expected if the cap bin size was a constant value, is in Figure 9.1b.

9.2 Results

Using the method outlined above the pretrial significance of local energy distribution deviations is calculated. The maximum relative energy spectrum anisotropy significance was found to be for energies $E \geq 10^{19.2}$ eV and an exposure ratio of 14.03% (or an average 30° spherical cap bin size). These are free parameters and appropriate penalty factors for this scan are taken by applying them to MC trials as described in 9.2.3.

The maximum significance at an energy threshold of $E \geq 10^{19.2}$ eV is interesting on its own due to the fact that distribution tests of flux such as χ^2 (and likelihood ratio tests) are biased towards having higher significances with greater statistics – $E \geq 10^{19.0}$ eV has 2.3 times more events.

Above $10^{19.2}$ eV there are 1332 data set events; 1248 with energy $10^{19.2} \leq E < 10^{19.75}$ eV and 84 with $E \geq 10^{19.75}$ eV. The energy threshold of $E \geq 10^{19.75}$ eV was used for the TA

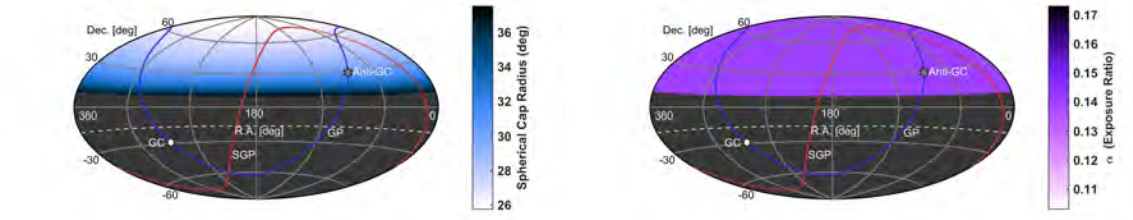

(a) (b)

Figure 9.1: Equatorial Hammer-Aitoff projections of the 14.03% equal exposure spherical cap binning and the resulting exposure ratio. The dashed curve at Dec. = -16° defines the FoV. (a) Spherical cap bin sizes with a MC defined exposure ratio $\alpha = N_{on}/N_{off} = 14.03\%$ at each grid point. The average bin radius is 30.0°. (b) Resulting very small variation in α exposure ratio (displayed on the range required if the cap bin size was a constant). $\alpha = 0.14028$ with an RMS of 9×10^{-5}.

"Hotspot" analysis and corresponds to the lower energy threshold determined by the AGN correlation results from PAO [25]. Due to the tighter cuts there are less events in this energy range. Figure 9.2 shows an equatorial coordinate sky map of the 1332 cosmic-ray events with E$\geq 10^{19.2}$ eV.

9.2.1 Density Map

The oversampled number of events, N_{on}, is shown in Figure 9.3a. A fairly large area of an overall deficit of N_{on} events can be seen by eye – this appears to be shifted off the supergalactic plane by ∼-10°. This can also be seen in the scatter plot of events in Figure 9.2.

9.2.2 Local Significance

Using the method outlined in Section 9.1 the significance of local energy spectrum deviations is calculated. In each spherical cap bin the energy distribution of events inside (N_{on}) are compared to the energy distribution of events outside the cap bin (N_{off}).

In the binned Poisson likelihood goodness of fit (GOF) test (Equation 9.1a), the *expected*

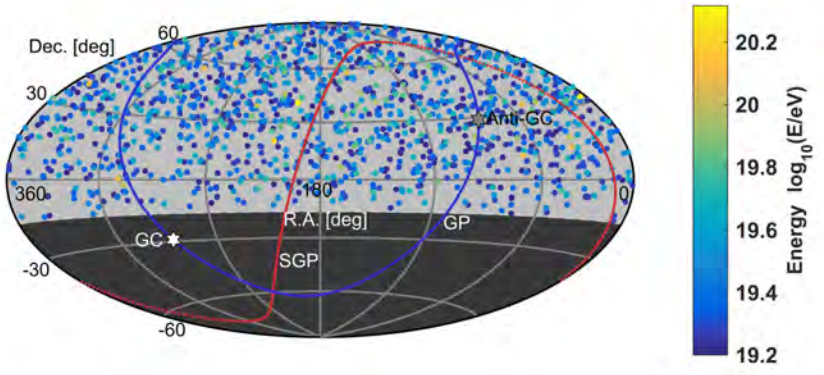

Figure 9.2: Equatorial Hammer-Aitoff projection of the 1332 UHECR events in the data set with E$\geq 10^{19.2}$ eV observed by the TA SD array. The colors are $\log_{10}$(E/eV). Any energy anisotropy is not easily seen by eye though there is an overall deficit of events at the location of the previously reported Hotspot (147° R.A., 43° Dec.). The dashed curve at Dec. = -16° defines the FoV. Solid curves indicate the galactic plane (GP) and supergalactic plane (SGP). White and grey hexagrams indicate the galactic center (GC) and galactic anticenter (Anti-GC).

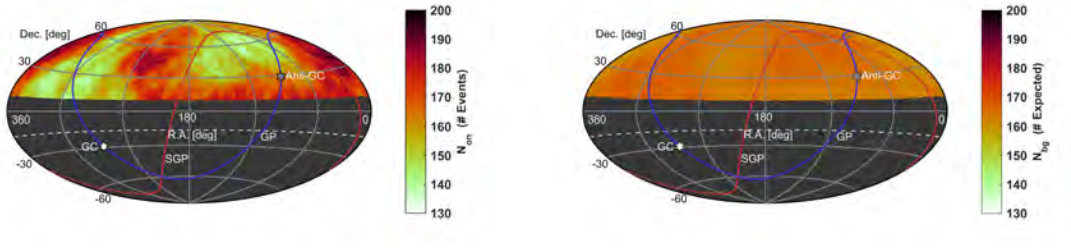

(a) (b)

Figure 9.3: Equatorial Hammer-Aitoff projections of the number of events inside 14.03% equal exposure bins and the expected background events (E$\geq 10^{19.2}$ eV). (a) Number of observed events, N_{on}, inside the spherical cap bins of Figure 9.1a. (b) Number of expected background events N_{bg}.

μ_i histogram bin frequencies are the N_{off} energy histogram frequencies normalized to the expected number of events inside the cap bin N_{bg}. N_{bg} is shown in Figure 9.3b and calculated using Equation 9.1d. The α parameter is shown in Figure 9.1b and is the MC calculated exposure ratio described in Section 9.1.2.

The resulting local pretrial energy spectrum anisotropy significance is shown in Figure 9.4, using the spherical cap bin average of 30° and E$\geq 10^{19.2}$ eV. The maximum pretrial significance is $6.17\sigma_{local}$ at 139° R.A., 45° Dec. inside a spherical cap bin of radius 28.43°. This is 7° from the previously published "Hotspot" location [27].

Figure 9.5 shows the binned Poisson likelihood energy distribution GOF test at the maximum significance location. The histogram of events inside the spherical cap bin of radius 28.43°, compared to the histogram of expected energies is in Figure 9.5a. Individual bin χ^2 contributions are in Figure 9.5b.

It is apparent that there is an equal contribution to the total χ^2 between a "Hotspot" excess of events E$\geq 10^{19.75}$ eV, and a "Coldspot" deficit $10^{19.2} \leq$E$< 10^{19.75}$ eV. The deficit is larger in magnitude than the excess as the expected number of events is $N_{bg} = 166.2$ and the observed number of events $N_{on} = 147$.

9.2.3 Global Significance

To calculate the global posttrial significance a scan penalty must be taken for the four minimum energy cuts ($10^{19.0}$, $10^{19.1}$, $10^{19.2}$, and $10^{19.3}$ eV) and 4 equal exposure ratio spherical cap bin sizes (3.35%, 6.04%, 9.58%, and 14.03%) that were tested to maximize the data

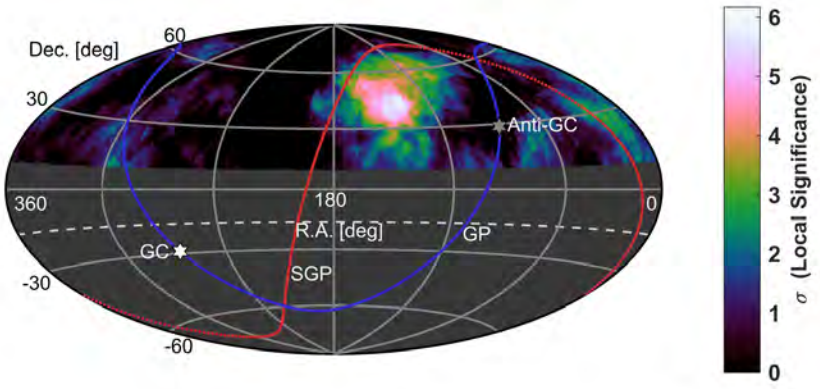

Figure 9.4: Projection of the local pretrial energy spectrum anisotropy significance for each 14.03% equal exposure spherical cap bin (E≥$10^{19.2}$ eV). The maximum significance is 6.17σ_{local} at 139° R.A., 45° Dec. This is 7° from the previously published Hotspot location [27]. The dashed curve at Dec. = -16° defines the FoV. Solid curves indicate the galactic plane (GP) and supergalactic plane (SGP). White and grey hexagrams indicate the galactic center (GC) and galactic anticenter (Anti-GC).

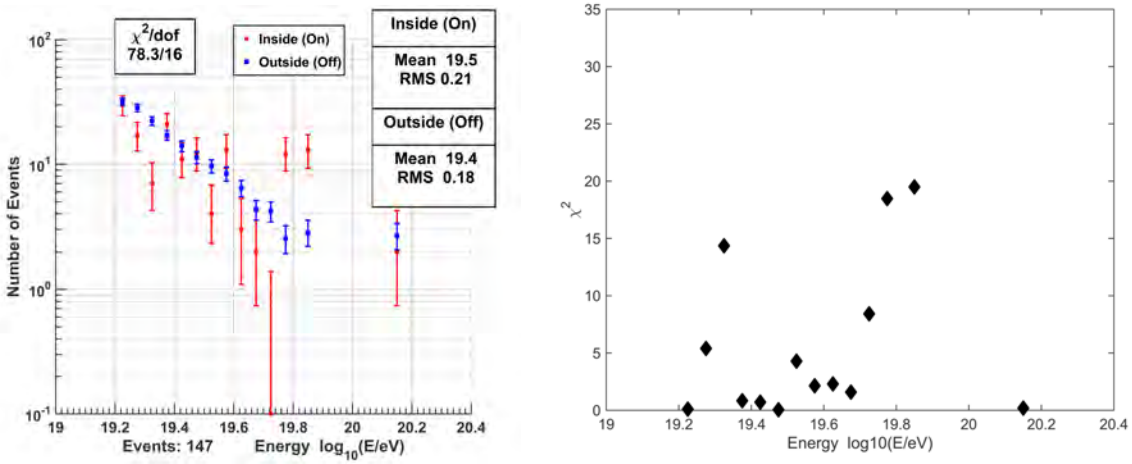

(a) (b)

Figure 9.5: Energy histogram at the point of maximum significance and the individual bin χ^2 contributions as calculated by Equation 9.1a. (a) Energy histogram of events, inside the spherical cap bin of radius 28.43° (red) at the maximum local significance shown in Figure 9.4, compared to the histogram of expected energies (blue). The expected number of events N_{bg} = 166.2. There are only three bins E<$10^{19.75}$ eV above expectation. (b) Individual bin χ^2 contributions.

binned Poisson likelihood GOF σ_{local} shown in Figure 9.4.

The isotropic Monte Carlo (MC) simulations, as described in Chapter 7, are created with the same number of events as the data for each low energy threshold. The scanned variables are applied to each MC set to create 16 binned Poisson likelihood σ_{local} maps. The maximum σ_{local} significance at any grid point on all 16 maps is considered as one MC for counting MC sets that have a higher significance than the data.

2.5×10^6 sets of 16 maps were created to calculate the posttrial global significance and the empirical probability distribution function (PDF) of these MC maximum σ_{local}'s is shown in Figure 9.6a.

There were 232 MC out of 2.5×10^6 MC that had a higher maximum significance than $6.17\sigma_{local}$. This corresponds to a global posttrial one-sided significance of 3.74σ. The conversion function which gives the posttrial global significance, for any local pretrial significance, from the one-sided p value of the empirical complementary cumulative distribution, is in Figure 9.6b. This can be applied to every point on the oversampling grid as shown in Figure 9.7. This shows that the area of significance is roughly $\sim15^\circ$ in radius.

It is certainly of interest to estimate how much more data would be needed for this

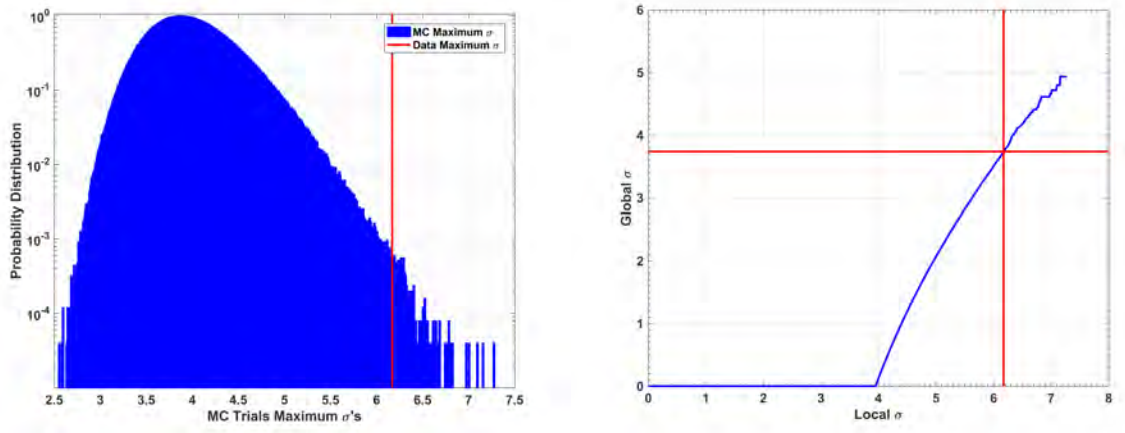

(a) (b)

Figure 9.6: MC trial maximum local significance distribution and the conversion to posttrial significance. (a) PDF of the maximum one-sided σ_{local}'s for all 2.5×10^6 MC trials. The area above the data, $6.17\sigma_{local}$, gives a 3.74σ global posttrial one-sided significance for the energy spectrum anisotropy. (b) Resulting significance survival function calculated, from (a), that returns the global posttrial significance, σ, given a pretrial local significance, σ_{local}. Red lines are the data result.

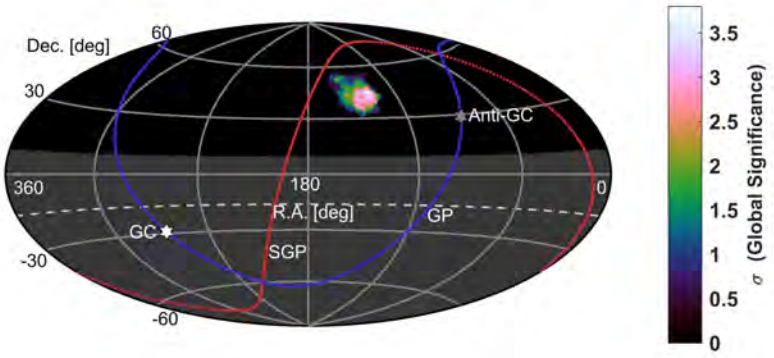

Figure 9.7: Projection of the global posttrial energy spectrum anisotropy significance for each 14.03% equal exposure spherical cap bin ($E \geq 10^{19.2}$ eV). The maximum significance is 3.74σ at 139° R.A., 45° Dec.; 7° from the previously published Hotspot location [27].

method to result in a posttrial 5.0σ observation. This can be estimated by fitting the linear trend of the local significance per integral day of data. Figure 9.8 shows the maximum binned Poisson likelihood significance on the data map starting at 1 year of data and for every additional day of data. According to a linear fit extrapolation adding an additional 8th year of data will possibly result in a pretrial significance of about $7.1\sigma_{local}$. According to Figure 9.6b this could result in a global posttrial significance of $\sim 5\sigma$.

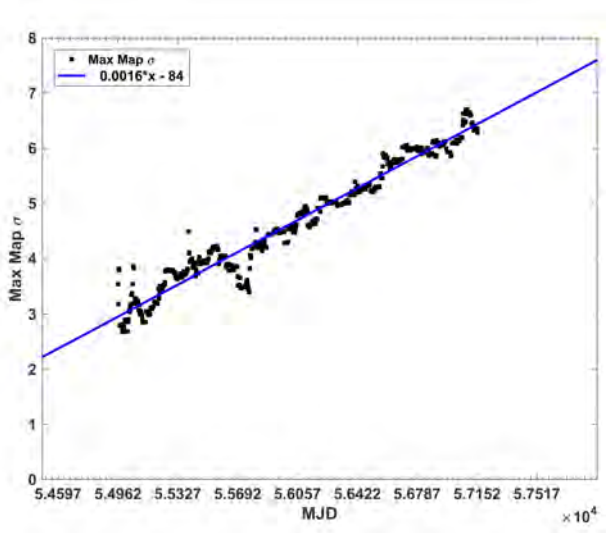

Figure 9.8: Maximum local pretrial significance for each additional day of data after the first year. Labeled x-axis tick marks are 1-year intervals. A linear fit extrapolates that an additional 8th year of data might result in a local pretrial significance of $\sim 7\sigma_{local}$.

9.3 Discussion

9.3.1 Supergalactic Plane Deflection

There are no known likely sources directly behind this composite excess/deficit feature at 139° R.A., 45° Dec. The location is centered near the supergalactic plane that contains local galaxy clusters such as the Ursa Major cluster (20 Mpc from Earth), the Coma cluster (90 Mpc), and the Virgo cluster (20 Mpc). The closest angular distance between the Hot/Cold center and the supergalactic plane is ∼19° which is the same distance as the maximum Hotspot alone and is in the vicinity of the Ursa Major cluster [27].

The starburst galaxy M82 is only 3.4 Mpc away and is reported by an independent analysis of the TA Hotspot to be the likeliest source. This is an analysis that makes use of angular distance and energy similar to that in Chapter 10 [29]. For events with energies E≥57 EeV this would require an angular deflection on the order of ∼25° in declination using the position result of Section 9.2.3.

If a straight line fit weighted by σ^2 is done in supergalactic coordinates for every grid point with a low energy "Coldspot," and a high energy "Hotspot," – the result is a shift off the supergalactic plane of -16° with a slope of 0.0. This is shown in Figure 9.9.

This is suggestive of an extended feature correlated with the supergalactic structure.

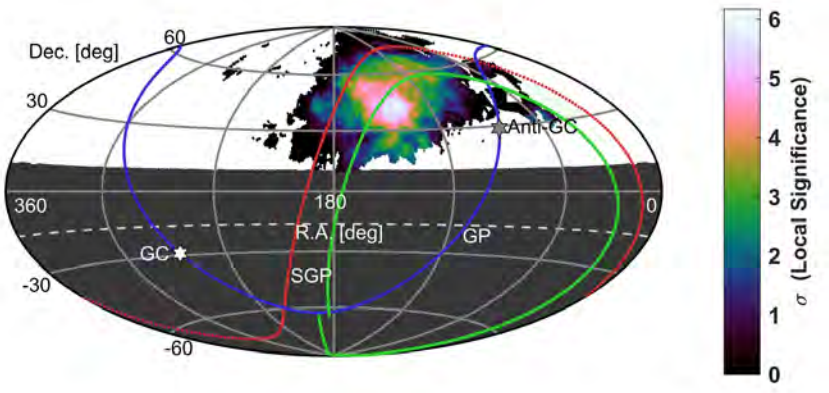

Figure 9.9: Projection of a supergalactic plane fit to the local pretrial significance of locations where there is a low energy Coldspot and a high energy Hotspot. The green line is a linear fit in supergalactic coordinates weighted by σ^2_{local} and is a shift of -16° off the supergalactic plane with a slope of 0.0. The red solid curve indicates the supergalactic plane (SGP).

Supergalactic magnetic sheets that can focus cosmic-ray flux, which has an effect for energies of E>50 EeV, has been discussed in [8] and deflection of lower energy background events transverse to the sheet is discussed in [10].

9.3.2 Li-Ma Hot/Coldspot

This result can be compared to the more common Li-Ma statistical test (described in Section 8.4) for anisotropy by a two energy bin spectrum test. Figure 9.10 shows the lower energy bin, $10^{19.2} \leq E < 10^{19.75}$ eV, and the higher energy bin, $E \geq 10^{19.75}$ eV, σ_{local} using the two-sided Li-Ma significance from Equation 8.6 [76] [77]. In Equation 8.6 the variables N_{on}, and N_{bg}, are the same as Equations 9.1b and 9.1d. The exposure ratio, α, is also the same Equation 9.1c. The resulting combined significance (probabilities multiplied) is shown in Figure 9.10c. The same low energy threshold and spherical cap bin sizing as Figure 9.4 is

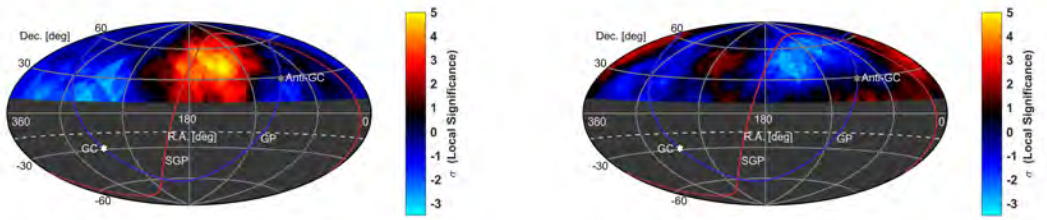

(a)

(b)

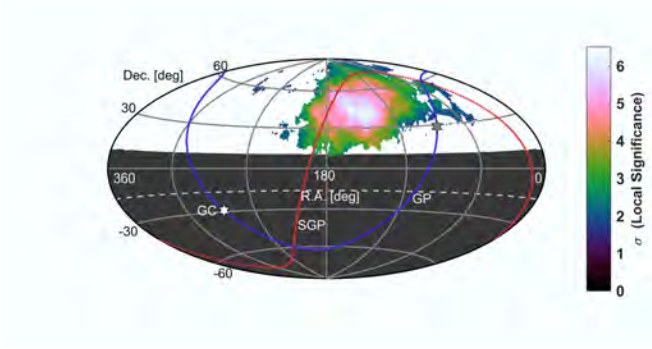

(c)

Figure 9.10: Li-Ma significances, with 14.03% equal exposure bins, for the high and low energy bins, and the combined significance of Hot/Coldspot areas. (a) Higher energy ($E \geq 10^{19.75}$ eV) two-sided pretrial Li-Ma significance. $S_{MAX} = 5.0\sigma_{local}$ at 147° R.A., 43° Dec. (b) Lower energy ($10^{19.2} \leq E < 10^{19.75}$ eV) significance. S_{MIN} = -3.5σ_{local} at 166° R.A., 47° Dec. (c) Combined significance (probabilities multiplied) of locations with Hot/Coldspot behavior. The maximum combined $S_{MAX} = 6.3\sigma_{local}$ is at 149° R.A., 42° Dec.

used, that is E$\geq 10^{19.2}$ eV and 30° $\langle$bin$\rangle$.

The high energy bin E$\geq 10^{19.75}$ eV has a "Hotspot" two-sided pretrial significance of S_{MAX} = 5.0σ_{local} at 147° R.A., 43° Dec. For the low energy $10^{19.2} \leq$E$< 10^{19.75}$ eV there is a "Coldspot" with two-sided pretrial significance of S_{MIN} = -3.5σ_{local} at 166° R.A., 47° Dec.

The maximum combined one-sided pretrial significance significance is at at 149° R.A., 42° Dec. with S_{MAX} = 6.51σ_{local}. It has the same "Hot/Coldspot" behavior. The combined Li-Ma significance at the point of the maximum Poisson likelihood GOF is 6.17σ_{local}. This is the same as the energy spectrum anisotropy result of Section 9.2.2. It is surprising agreement given that the different energy binning and statistical test would likely lead to a different global posttrial significance.

Chapter 11 calculates the posttrial Li-Ma significance of the Hot/Coldspot using the two energy bin test.

9.3.3 Energy Distribution Shape

Of interest is the probability distribution function (PDF) shape of the Coldspot and Hotspot parts of the energy spectrum anisotropy as this could perhaps help in understanding the physical mechanisms behind this feature. It is preferable to use the Crameŕ-von Mises (CvM) test as the CvM-test is an unbinned nonparametric test of equality of two probability distributions (the Poisson likelihood of Section 9.1.1 is binning dependent and is used as measure of difference in flux) [80] [94]. Unlike the Kolmogorov-Smirnov (KS) test, that uses the extremum difference between two cumulative distribution functions (CDF), the test statistic involves the integral area squared between the two CDF. It is a more accurate measure of agreement between PDFs.

Figure 9.11 shows the energy distribution with the *expectation* counts for the low energy Coldspot bin, and the high energy Hotspot bin, normalized to the *observed* counts. The sum of black bars congruent with blue bars is the 120 Coldspot events and the sum of black bars congruent with red bars is the 27 events in the Hotspot. The binning scheme is exactly the same as discussed in Section 9.1.1 and also used in Figure 9.5a (0.05 $\log_{10}$(E/eV) energy bins with expectation black bars combined with adjacent bins if $\mu_i < 1$).

The Coldspot CvM-test p-val = 0.38, shown in Figure 9.11, implies that the Coldspot follows the same spectral power law distribution as the rest of the data – but with a

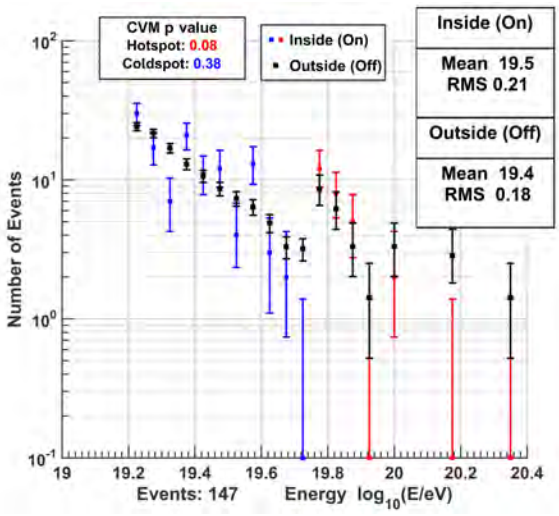

Figure 9.11: Energy histogram at the point of maximum significance with the expectation separately normalized for the Coldspot and the Hotspot. The Coldspot is $10^{19.2} \leq E < 10^{19.75}$ eV (blue), and the Hotspot $E \geq 10^{19.75}$ eV (red). The expected energies are black – the sum of the black bars congruent with the blue bars are the 120 Coldspot events and the sum of the black bars congruent with the red bars are the 27 events in the Hotspot. The CvM-test p values for the two ranges are shown.

suppressed flux as shown in Figure 9.5a. As for the Hotspot CvM-test the p-val = 0.08, though not significant, would seem to imply some disagreement with the rest of the data's GZK cutoff response in this energy range – even when accounting for the increased overall flux shown in Figure 9.5a.

Many probability density functions were fitted by unbinned maximum likelihood to the Hotspot data events to find the best fit. First, the energy is transformed to the center-of-mass energy, assuming incident proton UHECR, $E_{cm} = \sqrt{2Em_p}$. A list of fits (p>0.3) are shown in Table 9.1. They are ordered by the resulting p value of the CvM-test comparing the 27 data events to a 5×10^6 random number set for each distribution, with and without a cut at $E_{min} = \sqrt{2 \times 10^{19.75} m_p} = 3.06 \times 10^{14}$ eV.

The best fit is the generalized extreme value (GEV) distribution (p = 0.98) and uses only three parameters. The GEV distribution is the only possible limit distribution of a sequence of maxima of independent and identically distributed random variables. This is the resulting distribution of the maximum values taken from many independent distributions. This implies that, whatever the energy distribution of source particles, only the highest energy events reach us.

Table 9.1: Probability Distribution Fits to Hotspot Events

PDF	p val	Cut p val	Parameters
Data Outside	NA	0.0805	NA
GEV	0.984	0.983	ξ=0.43 (shape), σ=1.3$\times 10^{13}$ (scale), μ=3.4$\times 10^{14}$ (location)
Stable	0.979	0.974	α=1.1 (1st shape), β=1.0 (2nd shape), γ=9.3$\times 10^{12}$ (scale), δ=3.4$\times 10^{14}$ (loc.)
Cauchy-Lorentz	0.156	0.592	γ=1.1$\times 10^{13}$ (scale), x=3.4$\times 10^{14}$ (loc.)
Log-Logistic	0.512	0.155	σ=0.039 (scale), μ = 34 (loc.)
Breit-Wigner	0.08	0.452	γ=2.2$\times 10^{13}$ (width), M=3.4$\times 10^{14}$ (mass)
t Location-Scale	0.443	0.334	σ=1.6$\times 10^{13}$ (scale), μ=3.5$\times 10^{14}$ (loc.), ν=2.5 (degrees of freedom)
Gamma	0.240	0.343	a=179 (shape), b=2.0$\times 10^{12}$ (scale)

The Stable distribution is the next best fit, and has as special cases the Gaussian distribution, and the Cauchy-Lorentz distribution. It's a four parameter fit so it is not surprising that it is able to fit to 27 events with a $p = 0.98$. The first shape parameter, $\alpha \approx 1$, implies that the Cauchy-Lorentz fits better than a Gaussian. This is confirmed by the fitted distributions of Table 9.1. This shows that the Cauchy-Lorentz distribution is the best two parameter fit, and is the solution to forced resonance problems, which could imply a feature of UHECR acceleration. It is also used to described the energy distribution of coasting proton beams in accelerators.

The relativistic Breit-Wigner is a modified Cauchy-Lorentz distribution that models unstable resonance particles. The Delta baryon, Δ^+, of the GZK cutoff mechanism would follow this energy distribution. A resonance particle with the energy distribution of the fitted parameters would have a mean lifetime $\tau = 3 \times 10^{-29}$ s and a mass $M = 3 \times 10^{14}$ eV.

While a number of these distributions might lend themselves to possible interpretation in regards to UHECR dynamics, with only 27 Hotspot events much more data is needed to determine for sure whether the distribution follows the GZK cutoff, just as the rest of the data, or one (or more) of these probability distributions.

CHAPTER 10

ENERGY-DISTANCE CORRELATION

This is an unbinned search for energy-distance correlations using ranked correlations at the location of each event; measuring monotonic trend of distance versus energy for all events with greater energy. This energy-opening angle distance correlation anisotropy search is made with two assumptions – that UHECR are deflected by magnetic fields and there is a single dominant source of correlations. A single dominate source is an incidental assumption resulting from the method used to calculate the final significance. Previous energy-position correlation methods have made assumptions about magnetic field shapes and strength along with an assumed composition [95] [96] [97].

The resulting center of maximum significance of an energy-distance correlation source is at 125.9° R.A., 49.7° Dec. and has a pretrial one-sided significance of $6.47\sigma_{local}$. The post-trial probability of this $6.47\sigma_{local}$ energy-distance correlation source, appearing by chance on an isotropic sky, is found by Monte Carlo (MC) simulation to be 3.7×10^{-4} (3.37σ).

10.1 Energy Cut

For this analysis energies E$\geq$20 EeV ($10^{19.30}$ eV) were used. No scan of this energy threshold was done and therefore no scan penalty was calculated. This energy threshold was used for a previous energy-position correlation study that looked for multiplets of correlated events – though no significant multiplets were found [95] [73]. According to [37] 20 EeV is the theoretical upper bound of galactic iron, so this should be an extra-galactic result only. Furthermore, [98] states that for protons with energies above 20 EeV deflections can likely be considered linear with 1/E for typical galactic field models. The Telescope Array composition discussed in Chapter 13 is consistent with pure proton for E$\geq$2.5 EeV.

Also, as described further in Section 10.2.1 the energy-distance correlation is done at the point of each event using all events with higher energies. Therefore, the lower bound energy threshold of 20 EeV is not expected to be an important parameter to the final

significance.

The event reconstruction, and other cuts, are described in full in Chapter 4. After cuts, there are 852 events in the data set; 768 with energy 20≤E<57 EeV and 84 with E≥57 EeV. An equatorial coordinate sky map of the events colored by energy is shown in Figure 10.1. For calculating posttrial significances isotropic MC sets are created, as described in Chapter 7, with 852 events.

10.2 Correlations

As mentioned above, ultra-high energy studies of energy-position or energy-energy correlation have been done and all results were not significant [95] [96] [97]. These previous studies, as well as another suggested method [99] using spherical wavelets, include an abundance of scanned parameters along with assumed magnetic field models and UHECR composition. One of the first hints of an energy-position correlation was a cross-correlation between different chosen energy bins of AGASA data [100].

In this study no assumptions are made regarding magnetic field models or composition. Only one parameter choice is made – the 20 EeV lower bound energy threshold that

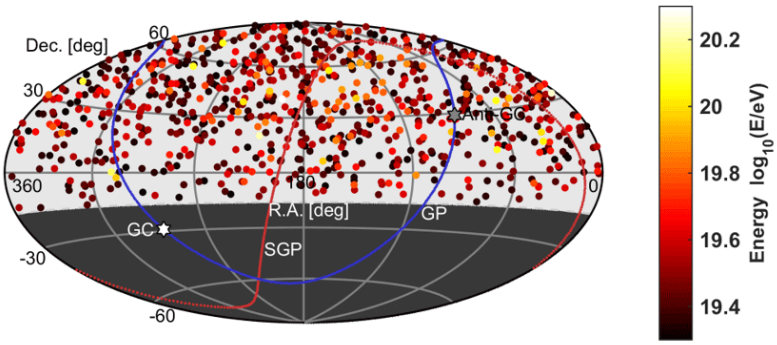

Figure 10.1: Equatorial Hammer-Aitoff projection of the 852 UHECR events in the data set, with E≥20 EeV, observed by the TA SD array. The colors are energy in $\log_{10}$(E/eV). Any energy-distance correlation is not visible by eye but there is an overall deficit of events at the location of the previously reported Hotspot (147° R.A., 43° Dec.). The dashed curve at Dec. = -16° defines the FoV. Solid curves indicate the galactic plane (GP) and supergalactic plane (SGP). White and grey hexagrams indicate the galactic center (GC) and galactic anticenter (Anti-GC).

is motivated by other studies as discussed in Section 10.1. The exact value of the lower bound energy threshold is not expected to significantly change the result and no scanning has been done to choose it.

The singular assumption is that lower energy cosmic ray events are deflected to larger angles from a source than those with higher energy. The significance of apparent deflections are found using a correlation of correlations (or meta-correlation) of energy versus distance between events as described below.

10.2.1 First Correlation

The position of every event in the data set becomes a "test point" from which all other events, with greater or equal energy, are selected. For example, the test point at the lowest energy event E = 20.03 EeV has sample size of N-1 = 851 events with energies E$\geq$20.03 EeV. The subset of events with larger energy are on average expected to be closer to a source than the test point.

The distance from a test point to each event in its subset is the great circle distance as described in Section 6.1.3. There is no binning or gridding of the sky and correlation energy thresholds are not chosen parameters.

Correlations between energy and distance at each test point are found using Kendall's τ_b ranked correlation [101]. Ranked correlation removes model assumptions and measures monotonic dependence between the variables. For the sake of brevity the simplified τ_a, that does not take into account duplicate values, is shown in Equation 10.1.

$$\tau = \frac{(\#\ of\ concordant\ pairs) - (\#\ of\ discordant\ pairs)}{n(n-1)/2} \tag{10.1}$$

The correlation coefficient τ_b has a range from -1 to +1. A coefficient of zero means there is no association between the variables. For -1, or perfect discordance, an increase (decrease) of variable x always follows a decrease (increase) in variable y. For +1, or perfect concordance, an increase (decrease) of x always follows an increase (decrease) of y.

Any monotonic function (x^n, $\log_{10}(x)$, e^x, etc.) can be applied to the distance, energy, or both and the resulting τ_b coefficient will have the same magnitude. The sign of the resulting coefficient would be the nontransformed τ_b multiplied by the signs of the first derivatives of the applied functions.

Though using great circle distance removes directional dependence of the correlation (along with the need for scanning directions, angular widths, or wavelet shapes [95] [96] [97] [99]), directionally dependent scattering for multiplets of events could still be found. This is due to the correlations being measured by oversampling using similar subsets of events at different locations in the sky. Also, the Kendall correlation is very robust against noise which is why it used here as opposed to Spearman's ranked correlation ρ (both are more robust than the more well known Pearson's *linear* correlation) [102].

10.2.1.1 First Result

An equatorial sky map of the resulting energy-distance correlations is shown in Figure 10.2. The color scale is the value of the correlation coefficient, τ_b, and the size of the circles at each test point are proportional to $1/p$-value, the p value being the probability that there is no correlation between distance and energy from that point (hypothesis – no correlation, alternative – nonzero correlation).

It can be seen that the correlations are clustered around the energy spectrum anisotropy

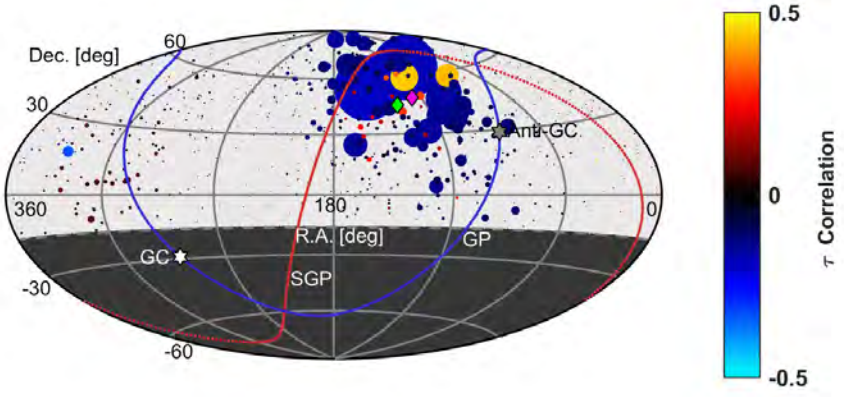

Figure 10.2: Projection of energy-distance correlation "test points," τ_b, for each event in the data set. Each dot size is proportional to $1/p$-value of the correlation and the color scale is τ_b. The average correlation location, weighted by $1/p$ is 126.2° R.A. 48.4° Dec. (magenta diamond). This is 15.2° from the previously published "Hotspot" location [27] and 9.4° from the energy spectrum anisotropy (green diamond). The dashed curve at Dec. = -16° defines the FoV. Solid curves indicate the galactic plane (GP) and supergalactic plane (SGP). White and grey hexagrams indicate the galactic center (GC) and galactic anticenter (Anti-GC).

of Chapter 9 and the previously reported Hotspot [27] [28].

Individual correlations with the highest pretrial significance are negative. This means that there is a trend, for events with greater energy (than the event at that point), for the distance to the next event to decrease with increasing energy. This is the expectation for the test point of a background event that happens to be near magnetically scattered source events. The signal is boosted, not decreased, by random background noise.

The test point with a negative correlation that has the highest posttrial significance is at 154.6° R.A. and 54.6° Dec. This test point, P_{-}, has a subset of 182 events with energies E≥41.18 EeV. The global posttrial one-sided significance of any test point in an MC set having $\tau \leq$-0.188 & p-val$\leq 1.67\times10^{-4}$ is 2.33σ. A map of event locations and a scatter plot of energy and distance are shown in Figure 10.3.

The test point with the highest global posttrial significance, P_{+}, is a positive correlation at 119.6° R.A. and 59.2° Dec. Its subset of 26 events have energies E≥75.041 EeV. The posttrial one-sided significance of a point with $\tau \geq 0.452$ & p-val$\leq 9.27\times10^{-4}$ is 2.46σ. A map of event locations and a scatter plot of energy and distance are shown in Figure 10.4.

Individual correlations with the highest posttrial significance are positive. This means that there is a trend, for events with greater energy (than the event at that point), for the

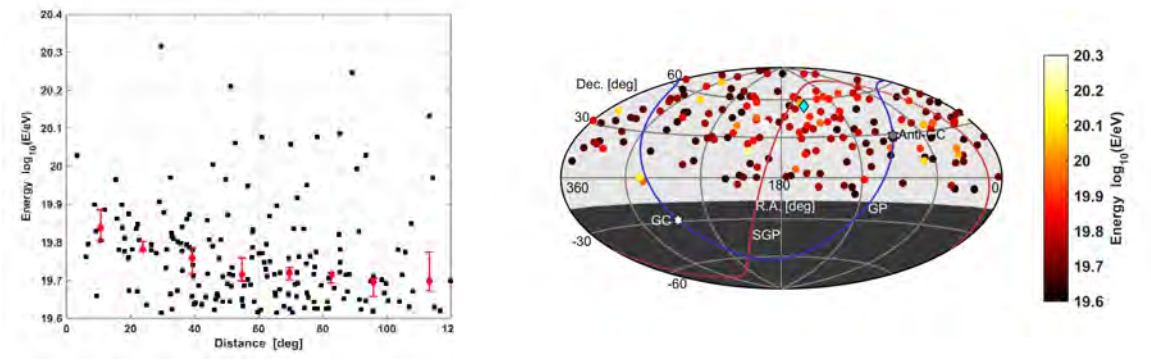

(a) (b)

Figure 10.3: Scatter plot, and projection, of the 182 events in the subset of the test point (154.60° R.A., 54.55° Dec.) with the most significant negative correlation between energy and distance (E≥41.18 EeV). τ_b = -0.188 and $p = 1.67 \times 10^{-4}$. (a) Scatter plot of energy in $\log_{10}$(E/eV) versus distance overlaid with bars of the median energy. (b) Hammer-Aitoff projection of a UHECR map in equatorial coordinates for the test point subset of events. The cyan diamond is the location of the test point. The color scale is energy in units of $\log_{10}$(E/EeV).

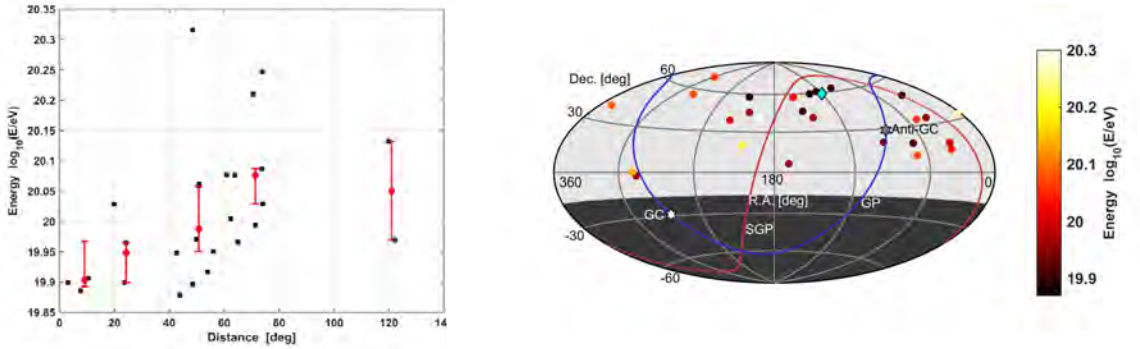

(a) (b)

Figure 10.4: Scatter plot, and projection, of the 26 events in the subset of the test point (119.617° R.A., 59.194° Dec.) with the highest posttrial significance correlation between energy and distance (E≥75.04 EeV). τ = 0.452 and $p = 9.27 \times 10^{-4}$. (a) Scatter plot of energy in $\log_{10}$(E/eV) versus distance overlaid with bars of the median energy. (b) Projection of the UHECRs in equatorial coordinates for the test point subset of events. The cyan diamond is the location of the test point. The color scale is energy in units of $\log_{10}$(E/EeV).

distance to increase with increasing energy. On average $\tau>0$ happens at higher energies as this is the expectation for the test point of a source event that is deflected away but is near the center of a source (that does not emit the highest energy events in the data set). The average energy of test points with positive correlation ($\tau>0$) is 36 EeV and for negative correlations ($\tau<0$) the average energy is 32 EeV. The energy threshold of P_+ is 75 EeV and P_- is 41 EeV.

This is further supported by the fact that by simulating simple point sources it is found that the density of positive correlations increase as the density of a source increases. Also, 6 out of the 7 closest subset events to the maximum posttrial significance test point, P_+, are inside the spherical cap bin of the maximum significance energy spectrum anisotropy of Chapter 9 with energies E≥57 EeV.

10.2.1.2 Significance Bounds

A reasonable estimate of a global posttrial significance of the correlations, as a whole, is the application of Stouffer's method ($\sigma \sim \sum_{i=1}^{k} \sigma_i / \sqrt{k}$) of combining independent tests to these two test points. Combining the posttrial significance of the most significant negative, P_-, and positive correlation, P_+, results in a 3.39σ one-sided significance of a source of energy dependent deflection. This is not the method used in the final significance calculation,

as these correlations are not independent, but the result can be considered as an upper limit on the significance and is 0.02σ higher than the final result.

A lower bound posttrial significance can be found by counting MC event sets having both an P_+, and P_-, of higher individual significance than the data. The result is 703 counts out of 1.5×10^6 MC which is 3.31σ. This is a lower bound as it does not take into account all the correlations or their positions.

A more proper measurement of significance will be shown to be in the middle of the upper bound and lower bound significances found in this section, $3.31\leq\sigma\leq3.39$. There are a number of reasons why neither of these estimates are used as the final significance – they do not take into account all pretrial significant correlations and the $\sim20^\circ$ clustering of the highest correlations or assume the correlations are independent. Also, the necessity of using multiple test statistics in finding a posttrial significance is not ideal. The location of the source of correlations is also not found.

10.2.2 Meta-Correlation

To appropriately measure the significance of the energy-distance correlation the bulk properties of all the test points should be taken into account. The test point correlations are measures made by oversampling from different locations on the sky, and each has a different sample size due to the different energy thresholds. Also, needed is a localization of the source since the individual test points are not at the source center where correlations of higher energy events are not likely to originate (higher energy events should be deflected less).

This is done by a linear Pearson correlation of the correlations, or a meta-correlation, between the $|\tau|$ correlation coefficients and great circle distance – at every test point to all test points. This can be considered similar to methods used in Seismology known as a ''Double Correlation or C^2'' [103]. The different sample sizes are accounted for by doing a partial correlation controlling for the p values. The linear correlation is shown in Equation 10.2a and the partial correlation in terms of linear correlations is Equation 10.2b. The maximum negative $\rho_{|\tau|,p}$ correlation is a source of energy-distance correlations – from that point the first correlations, τ, decrease in magnitude.

$$\rho_{XY} = \frac{Cov(X,Y)}{\sqrt{Var(X)Var(Y)}} \tag{10.2a}$$

$$\rho_{|\tau|,p} = \frac{\rho_{|\tau|\Delta d} - \rho_{|\tau|p}\rho_{p\Delta d}}{\sqrt{1-\rho^2_{|\tau|p}}\sqrt{1-\rho^2_{p\Delta d}}} \tag{10.2b}$$

The resulting meta-correlation is shown in Figure 10.5. Now that each test point has equal sample size a single test statistic can be used to find the significance of the possible energy-distance correlation source by counting isotropic MC.

10.3 Final Result

The maximum magnitude negative, $\rho_{|\tau|,p}$ (negative means it is a source of correlations) is located at 125.9° R.A. 49.7° Dec. and has a one-sided pretrial significance of $6.47\sigma_{local}$. This is 15.7° from the previously published Hotspot location and 10.0° from the energy spectrum anisotropy [27] [28]. This means that there is a significant decrease in energy-distance correlations when moving away from this point on the sky in any direction.

Figure 10.6a shows the distance with respect to the $|\tau|$ correlation for the test point of maximum significance. The trend of correlations from this point is further analyzed in Figure 10.6b. The correlations are separated into two clusters and separate bi-square linear fits are done to reduce the effect of outliers. It is apparent that there are two separate

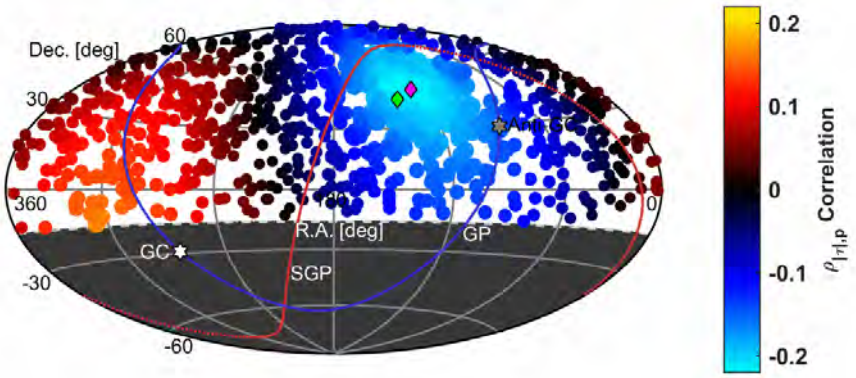

Figure 10.5: Projection of the τ-distance linear correlation coefficient controlling for the τ p values, $\rho_{|\tau|,p}$, for each test point of the data set. The dot sizes are proportional to the $1/p$-value of the $\rho_{|\tau|,p}$ coefficient and the color scale is the value of the coefficient. The maximum correlation location is 125.9° R.A. 49.7° Dec. (magenta diamond) and has pretrial significance of $6.47\sigma_{local}$. This is 10.0° from the energy spectrum anisotropy (green diamond).

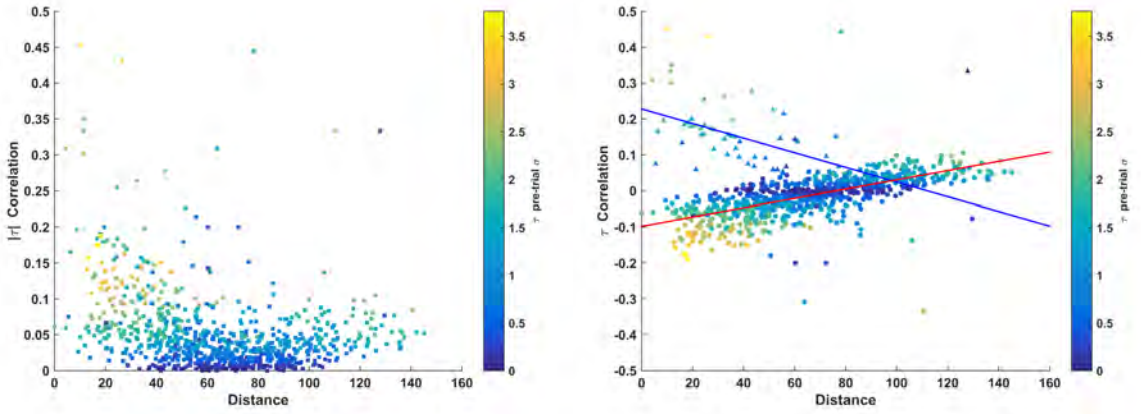

(a) (b)

Figure 10.6: Scatter plots of the τ correlation with respect to distance of the maximum posttrial significance test point, of the meta-correlation, $\rho_{|\tau|,p}$. Color scale is proportional to the pretrial significance of the τ correlations. (a) $|\tau|$ correlation with respect to distance. (b) τ correlation with respect to distance. Linear fits are made to two clusters – one cluster is triangles, the other circles. These are the two trends of decreasing magnitudes of correlations from this test point that contribute to the final significance.

trends of decreasing magnitudes of correlations from this test point – one for the negative correlations and one for the positive correlations. These two trends contribute to the final posttrial significance.

10.3.1 Global Significance

The global posttrial significance of an isotropic MC (or energy scrambled data) having a negative $\rho_{|\tau|,p}$ correlation with $6.47\sigma_{local}$ significance or greater is 3.37σ (556 MC counts out of 1.5×10^6 or 521 counts with energy scrambled data). This agrees well with the conclusion of Section 10.2.1. The probability distribution function (PDF) of MC significances is shown in Figure 10.7a.

The MC significance PDF enables the calculation of the posttrial global significance for any given local pretrial significance. This function is shown in Figure 10.7b. The local pretrial to global posttrial conversion can be applied to every test point and is shown in Figure 10.8. This shows that this is a fairly large effect, with a radius of about $\sim30^\circ$, that is a similar size to the spherical cap bin size of the Hot/Coldspot, and energy spectrum anisotropies.

An estimate of the future significance given more data can be found by fitting to a

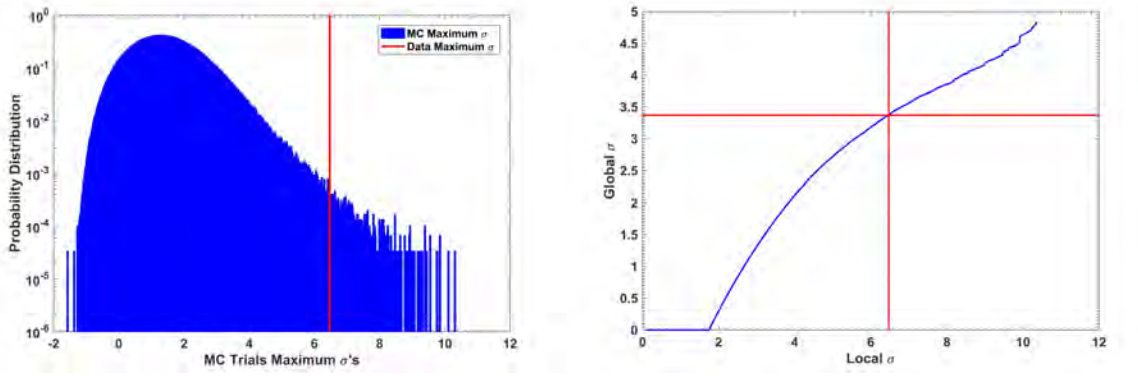

(a) (b)

Figure 10.7: MC trial meta-correlation maximum significance PDF and the conversion to posttrial significance. (a) σ_{local} PDF for all 2.5×10^6 MC trials. The area above the data, $6.47\sigma_{local}$, gives a 3.37σ global posttrial one-sided significance for the energy-distance correlation. (b) Resulting function calculated, from (a), that returns the global posttrial significance, σ, given a σ_{local}. Red lines are data.

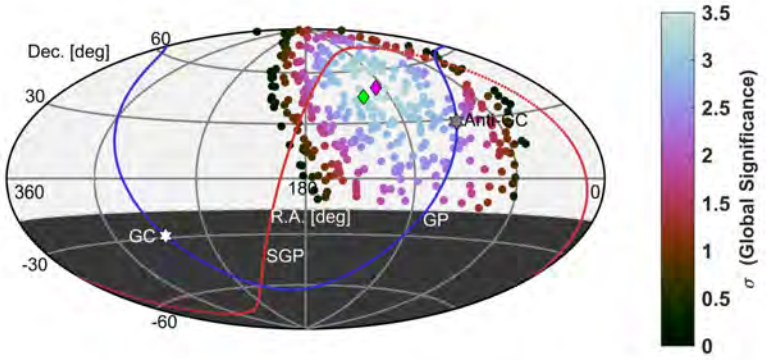

Figure 10.8: Projection of the global posttrial energy-distance correlation significance for each test point ($\rho_{|\tau|,p}>0$ have no significance). The maximum significance is 3.37σ at 125.9° R.A. 49.7° Dec.; 10.0° from the energy spectrum anisotropy (green diamond).

linear trend the local significance per integral day of data. Figure 10.9 shows the maximum pretrial significance on the data map for every additional day of data. According to a linear fit extrapolation starting with the 5th year of data, adding an additional 8th year of data will possibly result in a pretrial significance of $8.1\sigma_{local}$. According to Figure 10.7b this could result in a global posttrial significance of $\sim4\sigma$.

Figure 10.9: Maximum local pretrial significance of the energy-distance correlation for each additional day of data. Labeled x-axis tick marks are 1 year intervals. A linear fit, from the 5th year to the 7th year, extrapolates that an additional 8th year of data might result in a pretrial significance of $8.1\sigma_{local}$ (The discontinuity in slope is likely simply a result of low statistics).

10.4 Discussion

The maximum local pretrial significance, for the test of energy-distance correlation, is localized at 125.9° R.A., 49.7° Dec. with a statistical significance of $6.5\sigma_{local}$. The global posttrial probability of an energy-distance correlation anisotropy of this significance appearing by chance in an isotropic cosmic-ray sky was found to be 3.7×10^{-4} (3.37σ). It is estimated that a single additional year of TA SD data might yield a significance of $\sim4\sigma$.

The posttrial significance was also calculated by taking the data itself, scrambling the energies, and counting the number of scrambled data sets that had a greater test statistic. The final posttrial significance is the same as the isotropic MC result – this is assurance that the method is not another angular, or location clustering test (such as Chapter 8), but is in fact an energy-distance correlation.

The combination of energy-distance correlations and the energy spectrum anisotropy of Chapter 9 in the same vicinity in the sky results in an excess and deficit of events at the same location in some energy ranges. In this case it will be shown in Chapter 11 that this results in a composite feature of a Coldspot deficit of events at energies $10^{19.1}\leq E<10^{19.75}$ eV and a Hotspot excess of events for energies $E\geq10^{19.75}$ eV with a $\sim25°$ radius.

CHAPTER 11

HOT/COLDSPOT SUMMARY ANALYSIS

As has been shown in the previous three chapters a number of pieces of evidence for an energy dependent intermediate-scale anisotropy have been found in the arrival directions of ultra-high energy cosmic rays of energies above $10^{19.0}$ eV. The previously reported "Hotspot" excess above isotropic background for energies greater than $10^{19.75}$ eV corresponds to a deficit, or "Coldspot", of events for energies $10^{19.2} \leq E < 10^{19.75}$ eV. This combined feature is the result of an energy spectrum anisotropy shown in Chapter 9, with a significance of 3.74σ, and an energy-distance correlation shown in Chapter 10, with a 3.37σ significance – this is suggestive of possible energy dependent magnetic deflection of events from a source of cosmic-rays and the isotropic background at the source location.

In this chapter the analysis is done as a direct extension of the original Hotspot paper [27], and its 7 year update [28]. The Hot/Coldspot feature is studied by the method shown in Section 9.3.2 – that is oversampling the density of events in two energy ranges using spherical cap bins of a constant exposure ratio and calculating the Li-Ma statistical significance [76] [77].

At the center of maximum Li-Ma combined significance the Hotspot excess for energies $E \geq 10^{19.75}$ eV has a two-sided pretrial Li-Ma statistical significance of $+5.23\sigma_{local}$, and the deficit Coldspot for energies $10^{19.1} \leq E < 10^{19.75}$ eV has a significance of $-4.03\sigma_{local}$. This combined feature is centered at 142° R.A., 40° Dec. and has a combined one-sided pretrial significance of $7.11\sigma_{local}$.

The probability of an event density asymmetry as strong as this Hot/Coldspot, appearing by chance in an isotropic cosmic-ray sky, is found by Monte Carlo (MC) simulation to be 5.12σ. That is the significance of an excess and a deficit in either energy bin, where one energy bin has at least a magnitude of $5.23\sigma_{local}$, and the other at least a magnitude of $4.03\sigma_{local}$.

11.1 Method

The Hot/Coldspot analysis was done using the same oversampling grid, four equal exposure spherical cap bins, and four low energy thresholds as Chapter 9. The Li-Ma statistical method as described in Section 8.4 is applied to two energy bins as done in Section 9.3.2 – a high energy bin E$\geq 10^{19.75}$ eV and a low energy bin with energies at least E$\geq 10^{19.0}$ eV. The combined significance is the one-sided significance of the two energy bins two-sided Li-Ma significance p-values multiplied as discussed in Section 6.1.1.

11.1.1 Equal Exposure Binning

Exposure ratios (α) of 3.35%, 6.04%, 9.58%, and 14.03% were tested to maximize the data pretrial significance (these ratios result in spherical cap bin size averages of 15.0°, 20.0°, 25.0°, and 30.0°). The maximum significance was found with an exposure ratio of 9.58% and the bin sizes are shown in Figure 11.1a. This is a free parameter that the posttrial significance calculation takes into account as described in Section 11.2.2.

11.1.2 Energy Threshold

For the first energy bin low energy thresholds of E$\geq 10^{19.0}$, $10^{19.1}$, $10^{19.2}$, and $10^{19.3}$ eV were tested to maximize the data pretrial significance. The maximum significance was found with a threshold of $10^{19.1}$ eV with 1900 events. This is another free parameter that

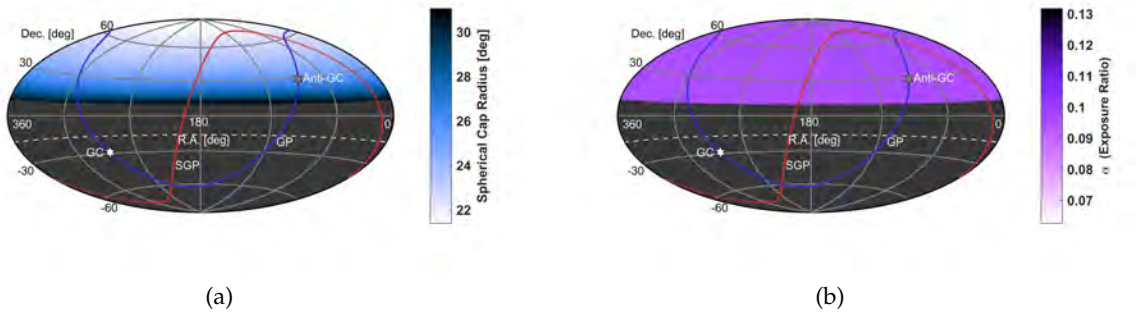

(a) (b)

Figure 11.1: Equatorial Hammer-Aitoff projections of the 9.58% equal exposure spherical cap binning and the resulting exposure ratio. The dashed curve at Dec. = -16° defines the FoV. (a) Spherical cap bin sizes with a MC defined exposure ratio $\alpha = N_{on}/N_{off} = 9.58\%$ at each grid point. The average bin radius is 25.0°. (b) Resulting very small variation in α exposure ratio (displayed on the range required if the cap bin size was a constant). $\alpha = 0.0957$ with an RMS of 1×10^{-4}.

the posttrial significance calculation takes into account as described in Section 11.2.2.

The high energy bin E$\geq 10^{19.75}$ eV is used to avoid a free parameter as this was used for the TA Hotspot analysis and corresponds to the lower energy threshold determined by the AGN correlation results from PAO [25] [27] [28]. This high energy bin is the same as used in Chapter 8. The scatter plot of Figure 8.1 shows these 84 events.

11.2 Results

The energy cut that maximizes the event density asymmetry significance is E$\geq 10^{19.1}$ eV. Above $10^{19.1}$ eV there are 1984 events in the data set; 1900 with energy $10^{19.1} \leq$E$< 10^{19.75}$ eV and 84 with E$\geq 10^{19.75}$ eV.

The Coldspot lower energy 1900 events are shown in Figure 11.2a. The Holdspot higher energy 84 events are shown in Figure 8.1. The oversampled number of events N_{on} inside each 9.58% equal exposure spherical cap bin (Figure 11.1a) is calculated from these events. This is shown in Figure 11.2b for the Coldspot energy bin events and in Figure 11.3a for the Hotspot energy bin events. Both the Hotspot excess and the Coldspot deficit of events can be seen by eye and appear to be about $\sim$-15° from the supergalactic plane.

11.2.1 Local Significance

Figure 11.2d shows the lower energy bin two-sided Li-Ma significance, σ_{local}, from Equation 8.6 [76] [77]. The higher energy bin σ_{local} is shown in Figure 11.3c.

The resulting one-sided local pretrial event density asymmetry significance, found from Figure 11.2d and Figure 11.3c, is shown in Figure 11.4. Grid points with no density asymmetry have zero significance (an excess or deficit in both energy bins). The maximum magnitude pretrial significance is a Hot/Coldspot with $7.11\sigma_{local}$ at 142° R.A., 40° Dec. inside a spherical cap bin of radius 24.23°. This is 6.5° from the Hotspot location of Chapter 8, 5.1° from the energy spectrum anisotropy of Chapter 9, and 14.6° from the energy-distance correlation of Chapter 10.

11.2.2 Global Significance

To calculate the global posttrial significance a scan penalty must be taken for the four minimum energy thresholds ($10^{19.0}$, $10^{19.1}$, $10^{19.2}$, and $10^{19.3}$ eV) and 4 equal exposure ratio spherical cap bin sizes (3.35%, 6.04%, 9.58%, and 14.03%) that were tested to maximize the

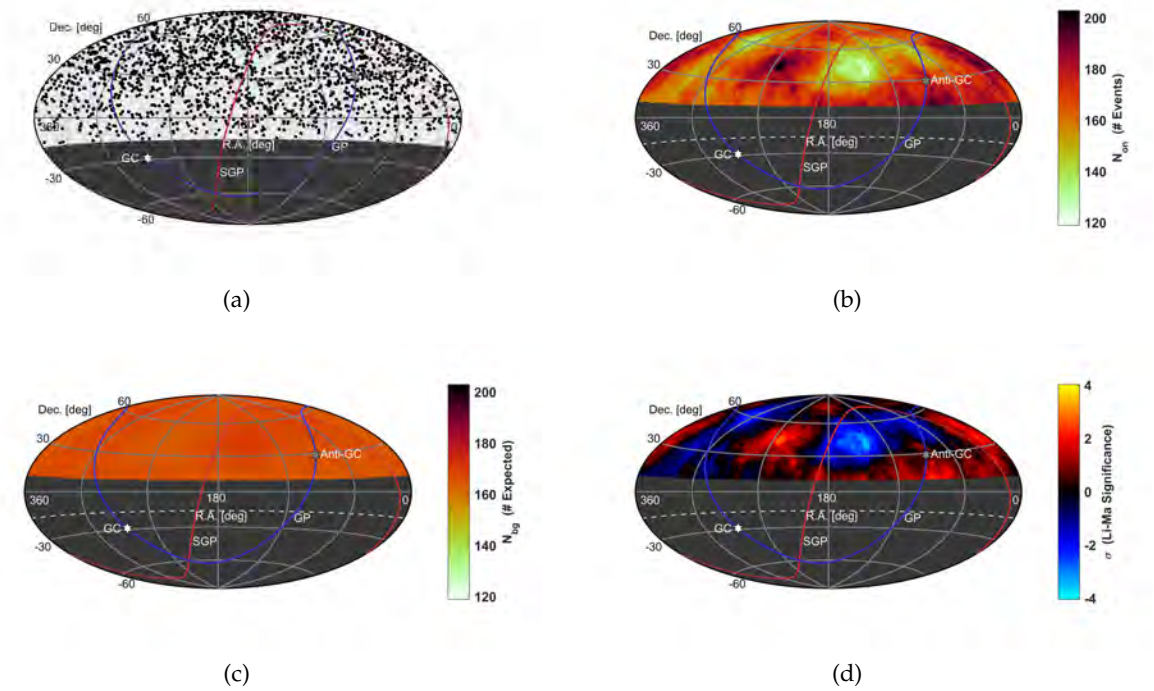

Figure 11.2: Projections of low energy bin UHECR statistics, inside 9.58% equal exposure bins, used to calculate Li-Ma significance and the result ($10^{19.1} \leq E < 10^{19.75}$ eV). (a) The 1900 UHECR events in the low energy bin observed by the TA SD array. A visible deficit of events is near the location of the previously reported Hotspot 147° R.A., 43° Dec. (b) Number of observed events, N_{on}, inside the spherical cap bins of Figure 11.1a. (c) Number of expected background events N_{bg}. (d) Local Li-Ma two-sided significance map calculated from Figure 11.1b, (b), and (c), multiplied by $sign(N_{on} - N_{bg})$.

combined Li-Ma σ_{local} shown in Figure 11.4.

The isotropic MC simulations, as described in Chapter 7, are created with the same number of events as the data for each low energy threshold and the 84 events in the high energy bin. The scanned variables are applied to each MC set to create 16 combined σ_{local} maps. All 16 maps are checked for a higher σ_{local} with a higher density asymmetry that data at any grid point on all 16 maps. This is considered as 1 MC for counting MC sets that have a higher significance than the data.

1.09×10^8 sets of 16 maps were created to calculate the posttrial global significance. The empirical probability distribution function (PDF) of the MC maximum density asymmetry σ_{local}'s is shown in Figure 11.5a.

To test for the significance of the event density asymmetry it is not enough that the

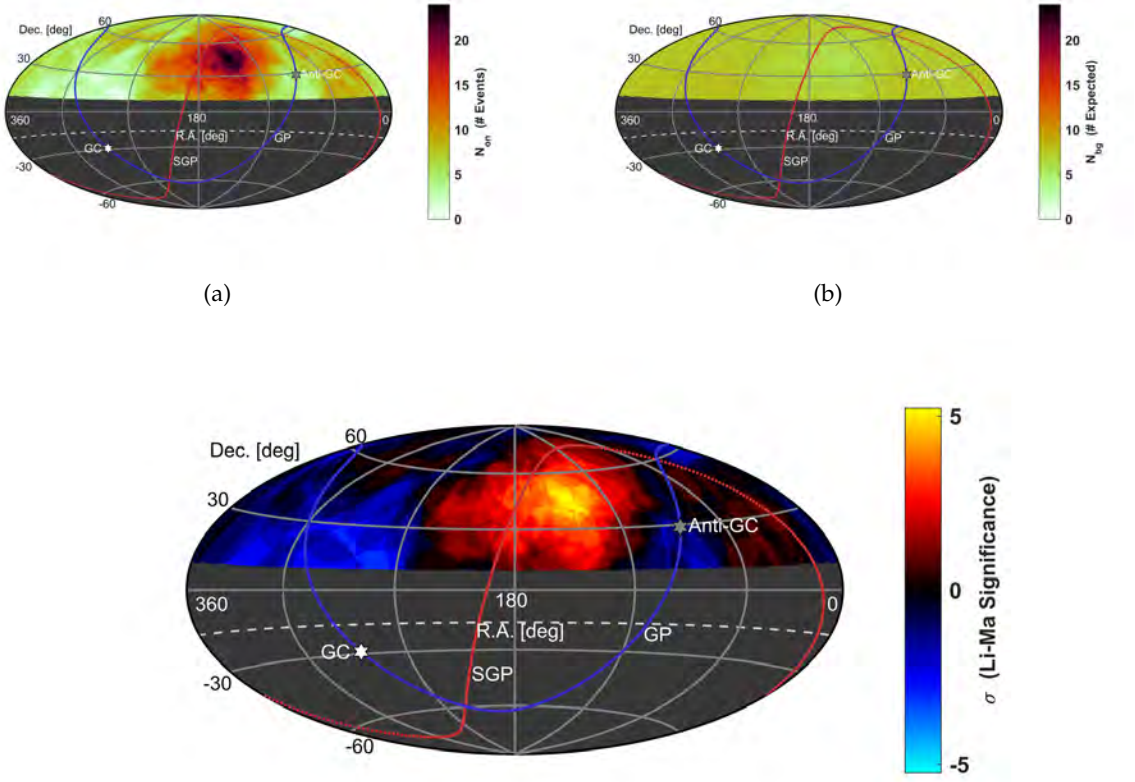

Figure 11.3: Projections of high energy bin UHECR statistics, inside 9.58% equal exposure bins, used to calculate Li-Ma significance and the result (E$\geq 10^{19.75}$ eV). (a) Number of observed events from Figure 8.1, N_{on}, inside the spherical cap bins of Figure 11.1a. (c) Number of expected background events N_{bg}. (d) Local Li-Ma two-sided significance map calculated from Figure 11.1b, (b), and (c), multiplied by $sign(N_{on} - N_{bg})$.

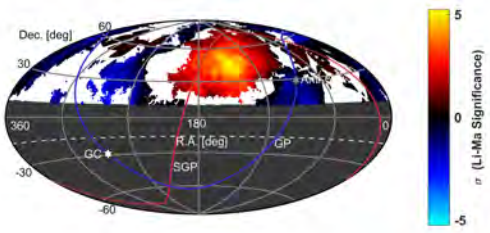

(a)

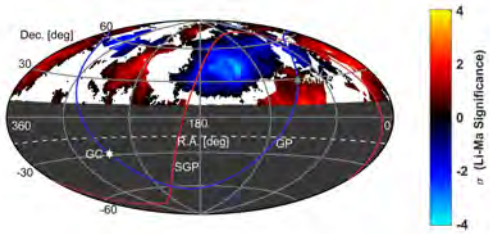

(b)

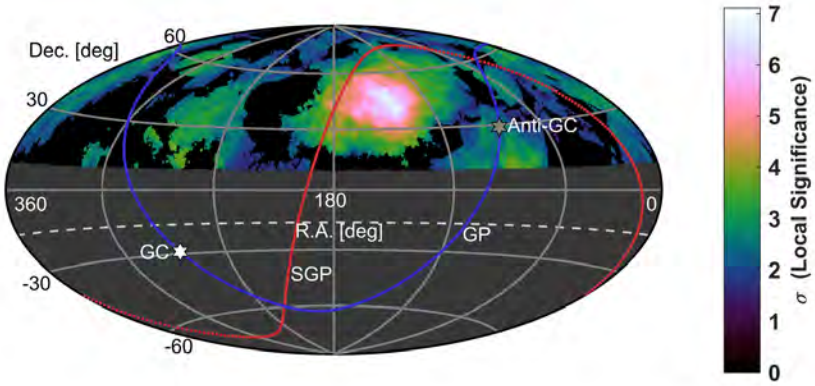

(c)

Figure 11.4: Projections of the two energy bins local two-sided Li-Ma significance and the one-sided combined significance – for 9.58% equal exposure bins with event density asymmetry. Grid points with no density asymmetry, i.e. an excess or deficit in both bins, are given zero significance. (a) High energy bin significance. (b) Low energy bin significance. (c) Combined local pretrial significance. The maximum is $7.11\sigma_{local}$ at 142° R.A., 40° Dec.; 5° from the energy spectrum anisotropy of Chapter 9.

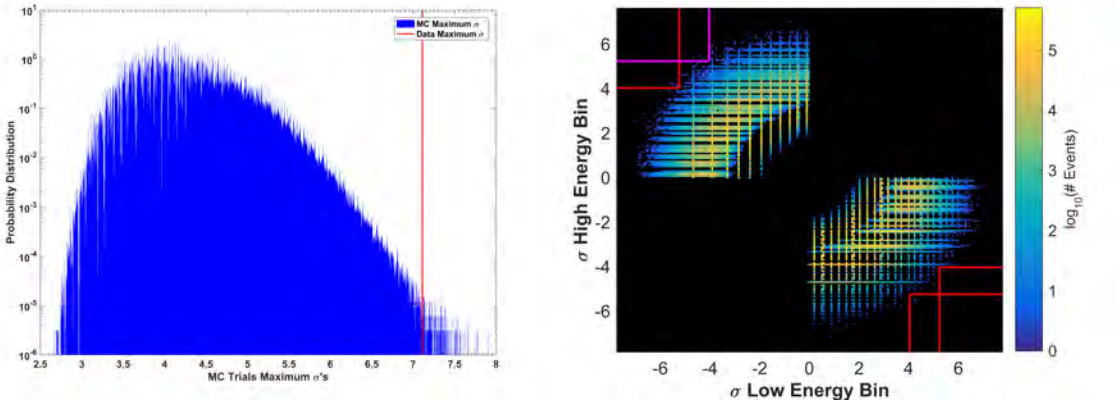

(a) (b)

Figure 11.5: MC trial maximum combined significance PDF (not used to calculate the posttrial significance) and the 2-d histogram of the two separate energy bin significances used to calculate the posttrial significance. (a) PDF of the maximum combined one-sided σ_{local}'s for all 1.09×10^8 MC trials. The area above the data, $7.11\sigma_{local}$, gives a 4.65σ global posttrial one-sided significance. This is not an event density asymmetry test. (b) 2-d histogram of the same MC trials low, and high, energy bin Li-Ma significances. Boundary lines are the significance test – MC inside the lines have a higher magnitude density asymmetry than the data. Magenta lines are the data values. The number of MC trials within the bounds corresponds to a 5.12σ significance.

combined σ_{local} be greater than or equal to the data combined σ_{local}. Each energy bin should also have a higher magnitude than the two data bins. The test for this is shown in Figure 11.5b. This is a 2-d histogram of the MC Li-Ma significances of the low energy bin and the high energy bin for the 1.09×10^8 MC maximum combined significances. The red and magenta lines show the bounds for which a MC trial would pass the test. The magenta lines are the data significances. Only 17 MC trials had a higher density asymmetry than the data (low energy $-4.03\sigma_{local}$ and high energy $5.23\sigma_{local}$). This corresponds to a global posttrial one-sided significance of 5.12σ.

Figure 11.5b also allows the calculation of the posttrial global significance for any two local pretrial Li-Ma significance values. This local pretrial to global posttrial conversion can be applied to every point on the oversampling grid and is shown in Figure 11.6. This shows that the area of significance is roughly $\sim15^\circ$ in radius.

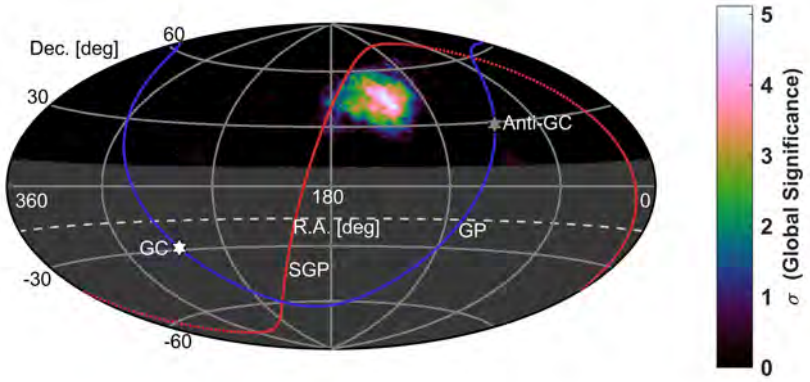

Figure 11.6: Projection of the global posttrial event density asymmetry significance for each 9.58% equal exposure spherical cap bin (E$\geq 10^{19.1}$ eV). The maximum significance is 5.12σ at 142° R.A., 40° Dec. This is 5° from the energy spectrum anisotropy of Chapter 9. The dashed curve at Dec. = -16° defines the FoV. Solid curves indicate the galactic plane (GP) and supergalactic plane (SGP). White and grey hexagrams indicate the galactic center (GC) and galactic anticenter (Anti-GC).

11.3 Discussion

A Hot/Coldspot has been found with a local pretrial combined Li-Ma significance of 7.11σ at 142° R.A., 40° Dec. inside a 24.23° spherical cap bin for events with energies E$\geq 10^{19.1}$ eV. That is 5° from the energy spectrum anisotropy of Chapter 9. The global posttrial one-sided significance of an event density asymmetry of this magnitude is 5.12σ.

Since the hypothesis of interest is magnetic deflection of lower energy events, Figure 11.7 has positive combined σ_{local} only for grid points with a high energy bin Hotspot and a low energy bin Coldspot. Negative σ_{local} is an excess or deficit in both energy bins or a low energy excess/high energy deficit. The apparent ∼16° shifted correlation with the supergalactic plane discussed in Section 9.3.2 is again visible.

The Hot/Coldspot has galactic coordinates of 182° l, 46° b, which given Figure 2.3, suggests deflections of about 1° to 10°, for 60 EeV protons depending on the model, and 6° to 60° for 10 EeV proton.

11.3.1 Evidence for Causal Connection

Under the hypothesis that low energy events are expected to be deflected further away from a source than high energy events – perhaps by a close source itself, supergalactic

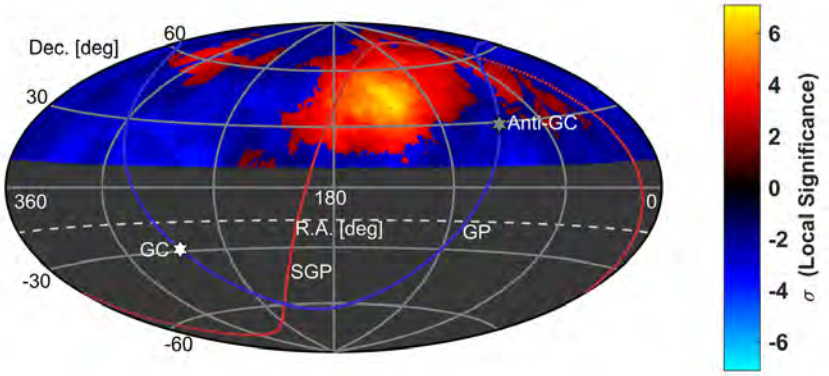

Figure 11.7: Projection of the local pretrial two-energy bin combined significance where locations with a Hot/Coldspot (High energy excess, low energy deficit) are positive and all other cases are negative – for 9.58% equal exposure bins. The maximum significance is $7.11\sigma_{local}$ at 142° R.A., 40° Dec. This is 5° from the energy spectrum anisotropy of Chapter 9.

magnetic sheets or flux tubes, and so forth – a low energy deficit, and high energy excess, event density asymmetry as shown by the Hot/Coldspot is expected. Besides the direct evidence for a causal connection between the Hot/Cold spots, from the energy-distance correlation of Chapter 10, further evidence for a causal connection between the Hotspot and the Coldspot is discussed below.

The significance of the Hotspot and the Coldspot are highly correlated with time. Figure 11.8 shows the magnitude of the local Li-Ma significance per integral day of data starting at one year of data at the location of the Hot/Coldspot. The correlation between the Hotspot magnitude and Coldspot magnitude has a zero chance (within CPU rounding error) of no correlation present.

The significance of any high energy excess, and a low energy deficit, is highly correlated with R.A. and Dec. This is shown in Figure 11.9 by taking the average significance in 1° bins. The correlation between the high energy excess event magnitudes and the low energy deficit magnitudes has a zero chance (within CPU rounding error) of no correlation present for both R.A. and Dec.

The maximum magnitude significance of each energy bin versus the scanned equal exposure spherical cap bin sizes (3.35%, 6.04%, 9.58%, and 14.03%) are also correlated

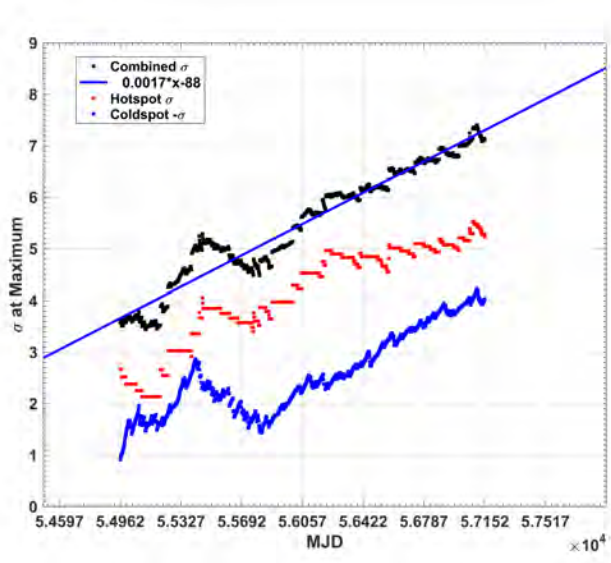

Figure 11.8: Magnitude of data local pretrial significance for high/low energy bins, and combined – for each additional day of data after one year at the Hot/Coldspot location. Black is combined, red is Hotspot significance, and blue is Coldspot significance. This shows that the Hotspot and Coldspot significances are correlated in time. Labeled x-axis tick mark are 1 year of data. Extrapolation tol 8 years of data shows a possible pretrial significance of $\sim 8\sigma$ that could result in a global posttrial $\sim 6\sigma$.

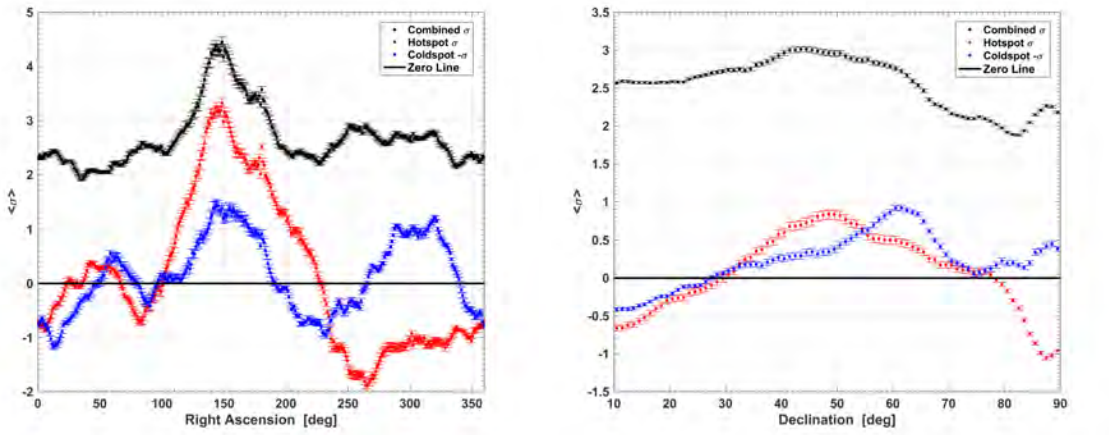

(a) (b)

Figure 11.9: Average pretrial significance of high/low energy bins, and combined – for grid points in 1° R.A., and Dec., bins. Black is combined, red is for the Hotspot, and blue is the magnitude of the Coldspot significance. (a) $\langle \sigma_{local} \rangle$ in 1° R.A. bins. This shows that the Hotspot, and Coldspot, significances are correlated in right ascension. (b) $\langle \sigma_{local} \rangle$ in 1° Dec. bins. This shows that the Hotspot, and Coldspot, significances are correlated in declination.

with each other (that is the size of the effect is the same measured independently): for the Hotspot energy the maxima are 4.64, 4.86, 5.24, and 5.01 σ_{local}, for the Coldspot energy bin the minima are -3.75, -3.93, -4.03, and -3.37 σ_{local} (for E$\geq 10^{19.1}$ eV). The location of maximum combined event density asymmetry significance is the same location as the Coldspot minima of -4.03σ_{local} and the Hotspot at that point has a significance of 5.23σ_{local} (only 0.01σ lower than the maximum).

The fraction of grid points with Hot/Coldspot behavior increases linearly with a cutoff on the high energy bin significance as can be seen in Figure 11.10a. All 3319 grid points with a high energy bin event excess with a $\sigma_{local}\geq 3.24$ have a low energy bin event deficit with an average $\sigma_{local} = -2.37$. These grid points range from 113° to 187° in R.A. and 26° to 65° in Dec. which shows that this behavior is not just at the Hot/Coldspot area.

The magnitude of the high energy excess σ_{local} at each grid point has a fairly linear relationship with the magnitude of the low energy bin deficit σ_{local}. This is shown in Figure 11.10b where the x-axis is the average high energy bin σ_{local}, within a 0.1 wide bin, and the y-axis is the average low energy bin σ_{local}. For high energy bin excesses with

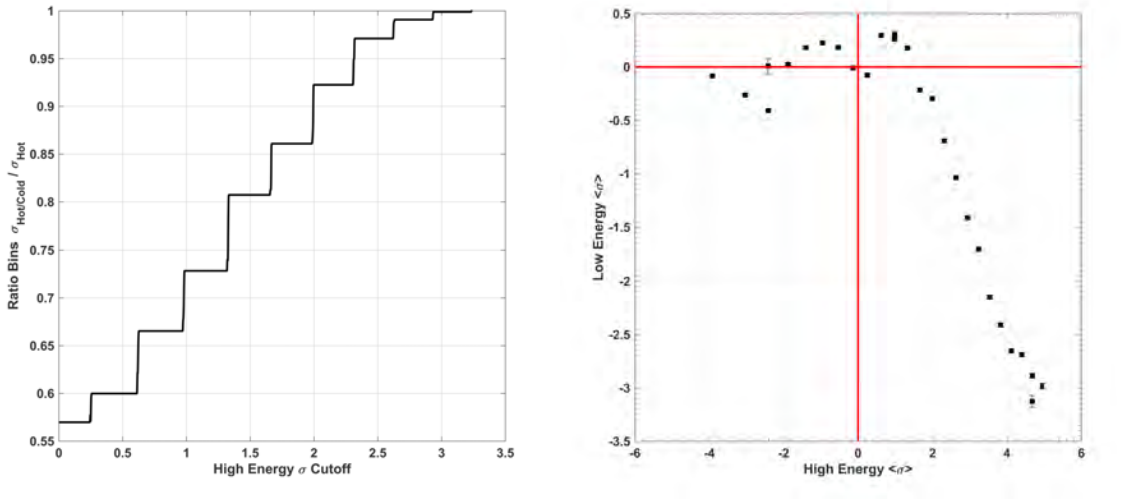

(a) (b)

Figure 11.10: Fraction of grid points, with a high energy bin excess greater than a σ_{local} threshold, that are Hot/Coldspots and a plot of average high energy bin σ_{local} versus average low energy bin. (a) Fraction of Hot/Coldspots. All 3319 grid points with a high energy bin event excess with a $\sigma_{local}\geq 3.24$ have a low energy bin event deficit. (b) High energy bin versus low energy bin $\langle\sigma_{local}\rangle$. As the high energy bin excess magnitude increases the average magnitude of the low energy bin deficit increases linearly for $\langle\sigma_{high}\rangle > 0.618$.

$\sigma_{local}>0.618$ as the magnitude increases the average magnitude of the low energy deficit increases.

The linear correlation coefficient for the correlation between σ_{high}, and σ_{low}, for all grid points is $\rho = -0.395$ with a zero chance (within CPU rounding error) of no correlation present. For all grid points with a high energy bin event excess ($\sigma_{high}>0$) the linear correlation coefficient for the correlation between σ_{high} and σ_{low} is $\rho = -0.625$ with a zero chance (within CPU rounding error) of no correlation present.

Furthermore, the maximum posttrial density asymmetry significance of a grid point with a low energy bin excess and a high energy bin deficit (a Cold/Hotspot) is only 0.84σ compared to the Hot/Coldspot 5.12σ. That is all grid points with a density asymmetry of any significance are low energy bin deficits and high energy bin excesses like the Hot/Coldspot.

11.3.2 Prior Information

It may be of interest to estimate a Bayesian-like consideration of the final significance of the results of this chapter since this analysis was done after the original published Hotspot analysis and the energy-distance correlation were found. It was considered probable that there would be a low energy deficit at the Hotspot given the appearance of the correlations of Chapter 10 and a magnetic deflection hypothesis. The energy spectrum analysis of Chapter 9 was not prior knowledge and is a more general energy anisotropy search.

Prior information of both the Hotspot, and the energy-distance correlations, may decrease the significance of this result but it is unknown exactly how much. Applying the Bonferroni correction of multiplying the p value by the number of tests (three) results in a 4.91σ significance.

PART III

COMPOSITION

CHAPTER 12

PATTERN RECOGNITION EVENT SELECTION

The most reliable composition dependent shower variable is X_{max}. X_{max} is the atmospheric depth of extensive air shower (EAS) maximum particle number discussed in Section 2.2.3 and Section 5.2.4. Good fluorescence detector (FD) X_{max} resolution requires that EAS have a clear rise and fall in photon signal flux vs. atmospheric slant depth (shower profile). EAS with clear peaks in the FD profile contain enough information for X_{max} to be reliably reconstructed.

When shower maximum is out of the FD field-of-view (FOV) the X_{max} reconstruction has a systematic dependence on the fitting method and the assumed form of the shower longitudinal distribution function. For profiles with a monotonically increasing or decreasing profile the position of shower maximum must be extrapolated. EAS on the lower end of the energy scale for the FD will usually be sufficiently bright enough to trigger the detector only when near the shower maximum. This results in a relatively flat profile that will also have a systematic dependence on fitting.

The effect on resolution of profiles lacking a large concave downward curvature can be reduced by fitting the Gaisser-Hillas (GH) function, requiring the resulting X_{max} to be within the FD FOV, and requiring a good fit [104]. The problem of flat profiles cannot be resolved this way as lower energy events have relatively large statistical errors in the signal bins and goodness of fit (GOF) tests for the GH profile will often report very good results. X_{max} resolution will have strong energy dependence if only a GOF is used. A different approach to removing these events is required.

A simple pattern recognition analysis (Binary PRA) method, independent of longitudinal distribution model (such as the GH form), has been created that categorizes events as flat, monotonically rising/falling, or sufficiently concave in signal magnitude such that we can be confident X_{max} is in the FOV. The method, along with ultra-high energy cosmic ray

(UHECR) composition results, has been previously described in [38]. Binary PRA gives a yes/no answer on whether a particular event has sufficient profile curvature which significantly improves the overall X_{max} resolution and the energy dependence of the resolution.

The downside of the Binary PRA is significant loss of statistics. Events can be recovered by applying a technique called Logistic Regression [105] [106] that extends the description of events further from a yes/no answer to a scale of the quality of each event. This is called the Quality Factor analysis (QFA).

12.1 Description

The PRA is applied to reconstructed FD shower profiles. EAS track shape is model independent and no model is needed to determine if there is a rise and fall in signal within the FOV. The simplest abstraction of a "GH like" (or concave) profile is a triangle. A set of triangles found from the shower profile is shown in Figure 12.1. These triangles, and profiles, contain the parameters required to discriminate non-concave events.

Based upon an eye scan of a sample (or training) set of Middle Drum (MD) hybrid FD/SD events (as reconstructed in Chapter 5) the method finds the limits on the allowed shapes of the extracted triangles and rejects events outside those limits. Only events that contain a shower maximum remain after cuts based on these limits are applied. The result is a track finder similar to those used in particle physics analysis [107].

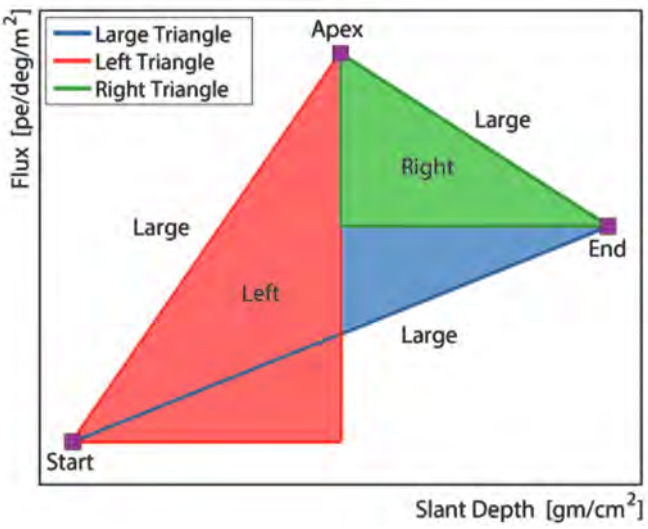

Figure 12.1: Triangles created from the binary pattern recognition (Binary PRA) feature construction step.

12.2 Binary Pattern Recognition Analysis (PRA)

Binary pattern recognition training involves creating a training set, constructing features, a decision tree (or cut value) population, and feature selection [108].

The training set was made by eye scanning a selected subset of MD hybrid FD/SD data and MC simulated events and categorizing them based on whether sufficient profile concavity can be seen. Data and MC simulation were treated equally as the training set is used only to find the allowable limits on the geometries of the triangles created from the feature construction step.

12.2.1 Triangle Construction

For triangle construction a fit on the shower profile to a quartic polynomial is done using an iteratively reweighted least-squares minimization, using a bi-square weights fit, that is robust against outliers, and bins with large errors [109]. The local maximum of the fit within the track of the shower is the apex of the large triangle.

The other two large triangle vertex points are found by a linear fits to the bins on each side of the apex. If there are three or less bins on a side of the apex the vertex is the a weighted average of signal for the y-axis and the slant depth of the last bin is the x-axis coordinate. The quartic fit is not used to find these two vertex points as it is unstable at the start and end of the track (due to there being more data points around the apex). These three points are used to form five triangles. The three most useful of these are labeled on Figure 12.1.

12.2.2 Feature Creation

For each training set event, attributes of the shower profile and fitted triangles were calculated. Some examples are profile statistics such as the signal mean and standard deviation, size and shapes of the five triangles, and the attributes of the signal quartic polynomial fit. The minimum and maximum values, for passed eye scan events, of more than 200 attributes were considered for cuts.

The largest or smallest values of the attributes of events with a clear X_{max} in view by eye scan give the allowed limits of these attributes.

12.2.3 Feature Selection

Feature selection is done to determine the attributes necessary to decide whether an event is good or bad. Cuts on features that do not remove any bad events (as determined by eye scan) are not used along with those that remove less than 0.5% of the training set. This minimizes the number of false negatives due to overfitting when the cuts are applied to a whole data set. Cuts (or groups of cuts based on categories) that remove the same events as another cut (or group of cuts), as found by brute force combinatorics, are also not used. The result is the minimum number of parameters needed to emulate the eye scan categorizing of events as good or bad.

The two cuts that remove the greatest number of bad events are a maximum limit to the allowed obliqueness (perimeter/area) of the large triangle and the minimum allowed area of the right triangle. The effect of these two cuts together is shown in Figure 12.2.

The training set good event in Figure 12.3a has the maximum value of large triangle obliqueness. This event sets the limit on the maximum allowed obliqueness of passed events. The training set good event in Figure 12.3b has the minimum value of right triangle area. This event sets the limit on the minimum allowed right triangle area of passed events.

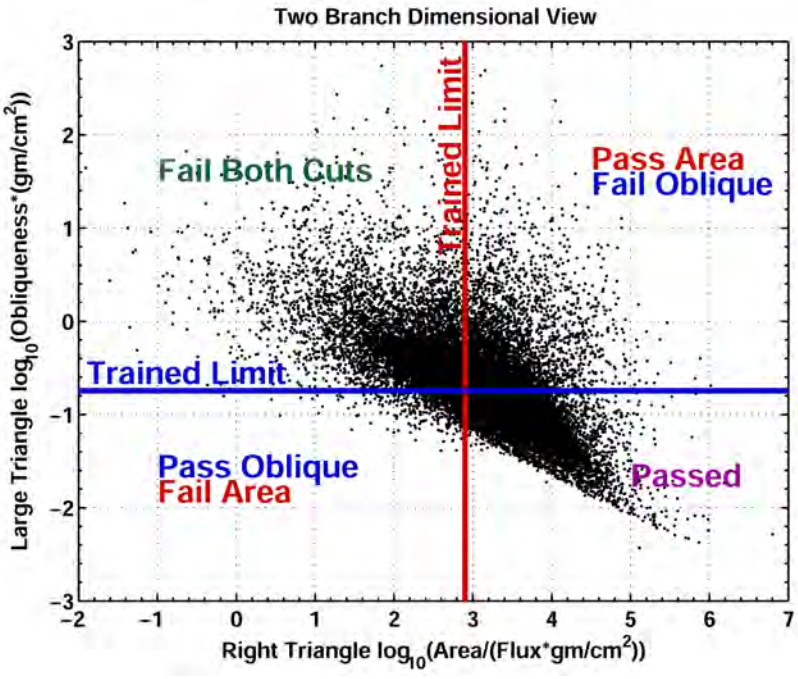

Figure 12.2: Events cut by the two Binary PRA features that cut the most events. Units given should not be interpreted as physical quantities.

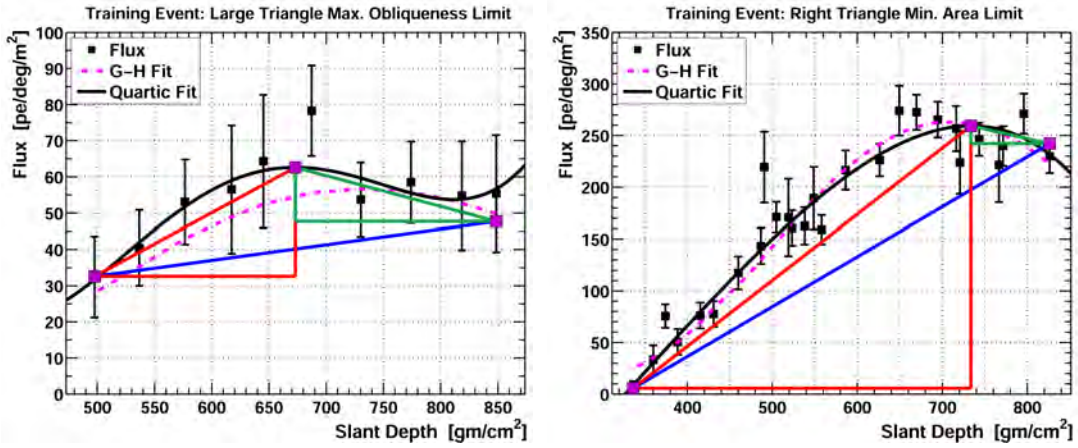

(a) (b)

Figure 12.3: Eye scan passed events that set limits on the two PRA features that remove the most bad events. (a) Maximum limit event for the large triangle obliqueness. (b) Minimum limit event for the right triangle area. Large error bins have been removed for display.

An event that was cut due to the right triangle area being smaller than the allowed limit is shown in Figure 12.4a. Figure 12.4b shows a failed event for which the large triangle obliqueness is larger than the allowed limit. The highest energy event shown in Figure 12.5 is the event with the smallest obliqueness and largest right triangle area.

Application involves extracting the features for the set of all data and MC simulated events, calculating the parameters that survived the feature selection process, and apply-

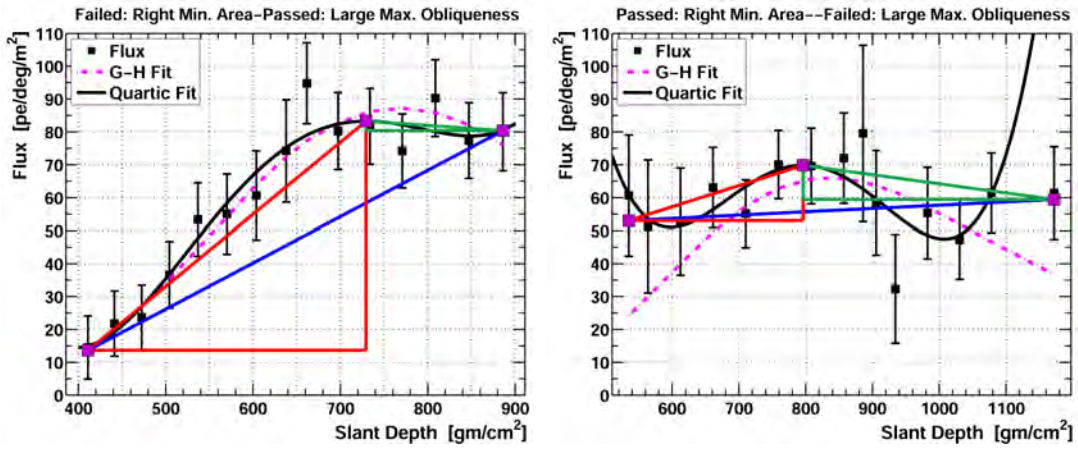

(a) (b)

Figure 12.4: Example events that pass one PRA limit but failed another. (a) An event that passed the large triangle obliqueness test but failed the right triangle area test. (b) An event that passed the right triangle area test but failed the large triangle obliqueness test.

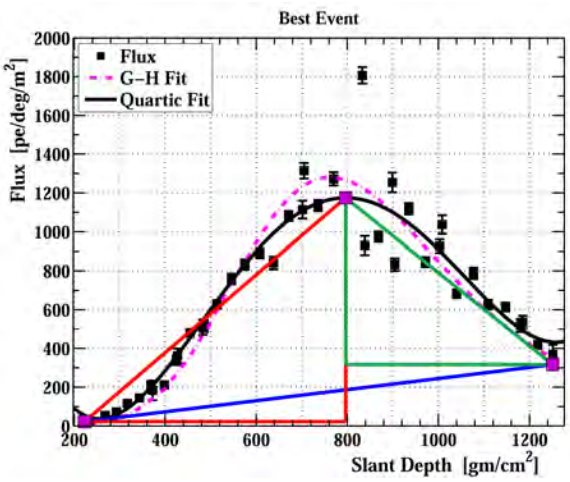

Figure 12.5: The passed event that has the minimum value of large triangle obliqueness and the maximum value of right triangle area (the best values of the two example Binary PRA features). This is also the highest energy event at E = $10^{20.12}$ eV. Bins with large errors have been removed for display purposes.

ing the cuts. If an event passes all cuts it is considered a good event. The result is a set of events for which the shower profiles have sufficient concave downward curvature that we can be confident that shower maximum is within the field-of-view (FOV) of the FD. The result of is an improved X_{max} resolution overall and a decrease in its dependence on energy.

12.2.4 Selected Features

The features found to be useful for emulating the eye scan are listed below. Shown in parenthesis is whether it is a minimum or maximum allowed value for an event to be passed as good.

1. Quartic Profile Fit

   (a) Cubic term of profile quartic fit (maximum). Remove events that are double peaked, wobbly, or have multiple stationary points.

2. Profile Attributes

   (a) Total number of profile bins (minimum). Ensures triangles can be fit to profile.
   (b) Mean of profile signal weighted by inverse square of bin errors (minimum). Event should be well above noise.

(c) RMS of profile signal weighted by inverse square of bin errors (minimum). Ensure minimum amount of signal variation to remove flat events.
(d) Maximum absolute difference of adjacent bin signals (minimum). Ensures minimum amount of signal change with slant depth.
(e) Percentage of slant depth extent largest gap without signal bins (maximum). Removes events possibly obscured by clouds.

3. Large Triangle

(a) Apex is between the other vertices. Ensures measured shower maximum is not at beginning or end of the profile.
(b) Length of smallest side (minimum).
(c) Length of middle sized side (minimum).
(d) Length of middle sized side normalized by apex signal maximum and slant depth extent (minimum).
(e) Magnitude of smallest vertex angle (minimum).
(f) Ratio of apex angle to length of opposite side (maximum).
(g) Ratio of normalized apex opposite side to apex angle (minimum).
(h) Perimeter/Area – sometimes called Obliqueness (maximum).

4. Left (Shallow) Triangle

(a) Obliqueness (maximum).

5. Right (Deep) Triangle

(a) Area (minimum).
(b) Normalized hypotenuse divided into the larger of the other two normalized sides (maximum).

6. Right (Deep) Underside Triangle

(a) Normalized length of largest side (minimum).

7. Mixed

(a) Number of bins on each end of profile up to or equal to large triangle apex depth (minimum). Improves confidence apex is in FOV.
(b) Profile "area" (signal*depth) without signal bins, normalized by apex signal maximum and slant depth extent (maximum). Removes events possibly ob-

scured by clouds. Increases importance of missing bins closer to shower maximum.

(c) Smallest vertical side (left or right triangle) divided by the average bin signal error (minimum). Concavity is more statistically significant.

12.2.5 Accuracy

The result is an overall accuracy of 98% when the cuts are applied to the training set – the total percentage of false positives being 2%. By construction false negatives are not possible when Binary PRA is applied to the training set.

Random test samples of events from the MD hybrid FD/SD data and proton Monte Carlo (MC) simulation sets were scanned by eye and the Binary PRA applied. The result was that the pattern recognition is 97% accurate on both the data and proton MC test sets. Twice as many random events were chosen for an iron MC test set as the pattern recognition was not trained on iron MC events. The iron MC accuracy is also found to be 97%. The overall accuracy including false positives, and negatives, when comparing the eye scan and pattern recognition for both training and test sets was 97%. On average only events in which X_{max} is not within the FOV (false positives) are detrimental to the resolution. Counting only false positives the accuracy percentage is 99.6%.

Samples of events from the Long Ridge/Black Rock stereo FD data and the corresponding proton/iron MC simulation sets were also scanned by eye and the Binary PRA applied. The result was that the PRA was 93% accurate according to eye scan. Counting only false positives the accuracy percentage is 96%. The difference between the hybrid and stereo accuracy is a result of looser stereo reconstruction failure parameters. These events where not accounted for by training with MD hybrid events. Most of the stereo Binary PRA false positives are easily removed with loose quality cuts.

12.2.6 X_{max} Resolution Energy Dependence

One of the benefits of this method can be seen in Figure 12.6. This figure shows that the energy dependence on resolution, largely caused by events with X_{max} outside the fluorescence detector FOV, is significantly improved by the pattern recognition analysis when compared to the usual shower geometry cuts. This result was published in [38].

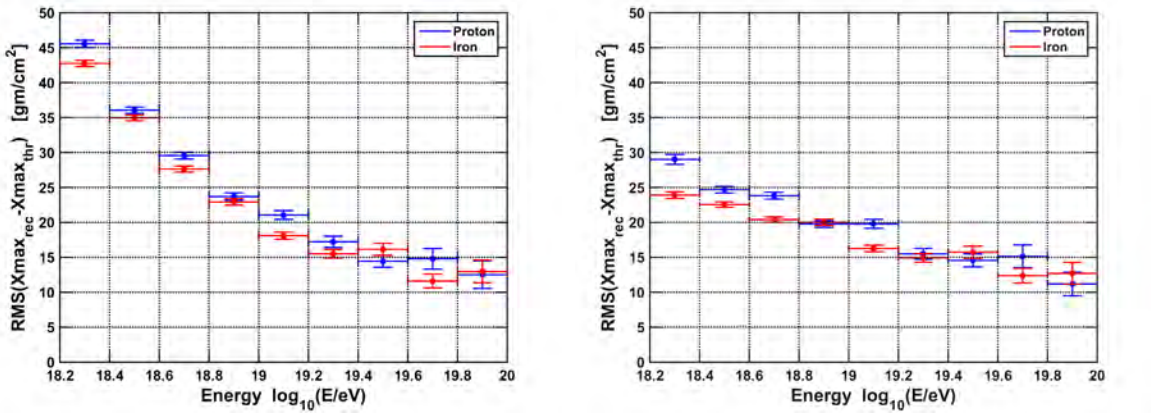

(a) (b)

Figure 12.6: X_{max} resolution plots, showing the energy dependence of the RMS QGSJETII-03 MC reconstructed minus thrown X_{max}, for geometry cuts only (Section 5.3) and Binary PRA applied. (a) Geometry cuts only. (b) Binary PRA with additional geometry cuts.

12.3 Quality Factor Analysis (QFA)

Eye scan determination of events is effectively modeled by the Binary PRA method but creates a ∼50% reduction in passed events compared to the usual shower geometry cuts. Instead of cutting events by a binary yes/no answer some events can be recovered by determining a scale of quality of events and selecting a threshold on this value. This can be done with Logistic Regression (LR) which is a type of binary classification [105] [106]. LR is used extensively in marketing, finance, biology, and medicine.

The inputs to LR are a binary yes/no response vector, and a set of attributes (predictors), that are intended to predict the response. The returned coefficients of the LR model can be used to calculate the probability of a future event being a "pass" for the yes/no question – given that events values for the same set of predictors.

Equation 12.1 shows the logistic regression cost function minimized to find the coefficients. This is derived using the maximum likelihood ratio method [105] [106]. N is the number of events, j is the event index, y_j is the response from Binary PRA (a 0 or 1), $\vec{x}_j$ is the vector of predictor values (a subset of PRA features). Equation 12.2 is the logistic function and takes as input the dot product of the fitted coefficient vector and the predictor vector. This returns the probability that the event is good. The logistic function maps the range $(-\infty, \infty)$ to $[0, 1]$.

$$min_{\beta} J(\beta) = -\sum_{j=1}^{N} [y_j \log F(\vec{x}_j) + (1 - y_j) \log (1 - F(\vec{x}_j)] \tag{12.1}$$

$$F_j(\vec{x}_j) = \frac{1}{1 + e^{-(\beta_0 + \vec{\beta} \cdot \vec{x}_j)}} \qquad \vec{\beta} \cdot \vec{x}_j = \beta_1 x_{j1} + \beta_2 x_{j2} + \ldots \tag{12.2}$$

In this case the response vector is the data passed from only a subset of the Binary PRA features. The predictors are another subset of the Binary PRA features. The subsets were chosen to maximize the increase in statistics for any particular resolution and to optimize the correlation between Quality Factor (QF) and resolution.

12.3.1 Features

Response vector (training set) Cuts: Shown in parenthesis is whether it is a minimum or maximum allowed value for an event to be passed as good.

1. Quartic Profile Fit
   (a) Cubic term of profile quartic fit (maximum). Cut is loosened compared to PRA.
2. Profile Attributes
   (a) Weighted RMS of profile signal (minimum). Cut is tightened.
   (b) Largest gap without signal percentage of slant depth extent (max). Cut is loosened.
3. Large Triangle
   (a) Length of smallest side (min). Cut is loosened.
   (b) Ratio of normalized apex opposite side to apex angle (min). Cut is tightened.
   (c) Obliqueness (max). Cut is tightened.
4. Right (Deep) Underside Triangle
   (a) Normalized length of largest side (min). Cut is loosened.
5. Mixed
   (a) # bins on each end of profile up to the large triangle apex depth (min).
   (b) Normalized "area" without signal bins (max).

Predictor Values:

1. Quartic Profile Fit
   (a) Cubic term of profile quartic fit.
2. Profile Attributes
   (a) Profile signal weighted mean. QF set to zero for events removed by Response vector cut.
   (b) Maximum absolute difference of adjacent bin signals.
   (c) Largest gap without signal percentage of slant depth extent.
3. Large Triangle
   (a) Apex between other vertices. Binary value.
   (b) Length of middle sized side. QF set to zero for events removed by Response vector cut.
   (c) Ratio of apex angle to length of opposite side. QF set to zero for events removed by Response vector cut.
4. Left (Shallow) Triangle
   (a) Obliqueness.
5. Right (Deep) Underside Triangle
   (a) Normalized length of largest side. QF is zero for large values.
6. Mixed
   (a) # bins on shallow side of large triangle apex.

12.4 QF Resolution Equivalences

The resulting QF scale shows a strong correlation with reconstruction resolutions (and bias) of X_{max}, energy, zenith and azimuth angle, and R_p. As QF increases all these values improve. The energy and X_{max} resolutions with respect to QF threshold (or integral plot) are shown in Figure 12.7 (very loose geometry cuts were applied).

Events with a longer track, higher photon signal, smaller signal uncertainties, and clearer signal peak have higher quality factors. Since a very clear signal peak is no longer required there is also an approximately 40% increase in the number of passed events for

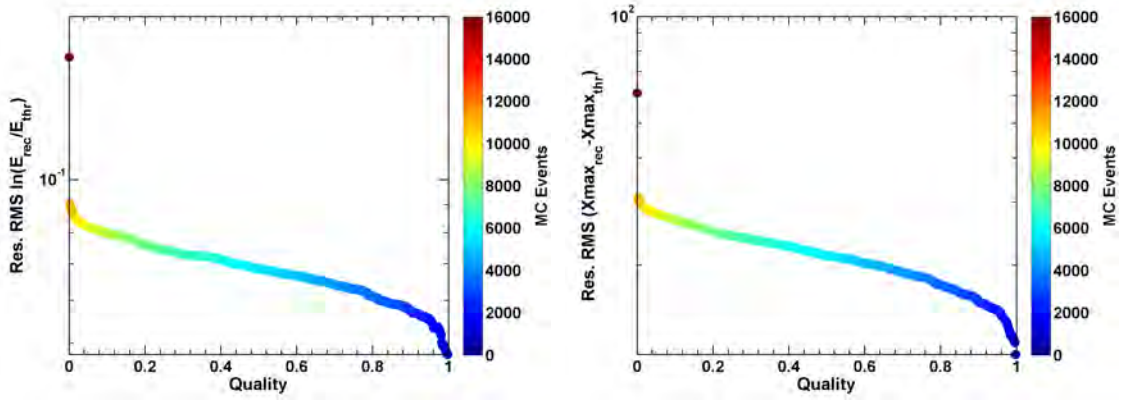

(a) (b)

Figure 12.7: Energy, and X_{max}, integral Quality Factor (QF) RMS resolution plots – QF threshold correlation with resolutions (QGSJETII-03 proton). Color is number of events in the MC set. Loose cuts E>$10^{18.2}$ eV, SD boundary dist. >-1500 m, zenith <60°, and SD/FD core diff. <2500 m. (a) Energy resolution versus QF threshold. QF≥0 is 17%. (b) X_{max} resolution versus QF threshold. QF≥0 is 60.9 g/cm^2 .

the same resolution. The final QF threshold of a 19.6% or greater probability of being a good event was chosen to result in the same X_{max} resolution as the Binary PRA.

12.5 Conclusion

Applying a Quality Factor threshold allows selection of the desired X_{max} resolution. Events with X_{max} in the FOV can still be incorrectly reconstructed therefore cuts that take into account the event geometry need to be applied in addition to a QF threshold. Geometry cuts were optimized to further minimize the energy dependence of the X_{max} resolution while maximizing the number of events. The optimized geometry cuts are listed in Section 5.3. The resulting resolutions energy dependence is shown in Figure 5.4b for QFA and is flatter than the Binary PRA (Figure 12.6b) with a 40% increase in the number of passed events. This important if the UHECR composition is energy dependent. The resulting composition study is discussed in Chapter 13.

CHAPTER 13

COMPOSITION

The composition analysis in this thesis uses seven years of observation from the Middle Drum (MD) FD and surface detector (SD) array for a set of hybrid measurements using the event reconstruction described in Chapter 5. This site consists of telescopes repurposed from the HiRes-1 experiment and are described in Chapter 3 [45]. These observations are compared to a set of distributions created by Monte Carlo (MC) simulations that use a detailed model of the detector as described in Section 2.3.6 and Section 3.3. Also introduced is the "shift plot" that compares the full shape of the data and MC distributions, and their evolution with energy, using the two-sample L-test developed for this thesis (described in Appendix B).

The composition of ultra-high energy cosmic rays (UHECRs) is an important contribution to the unsolved question of their origin. The Greisen-Zatsepin-Kuzmin (GZK) limit [12] [13] has been seen by a number of experiments including the Telescope Array (TA) and Pierre Auger Observatory (PAO) [110] [111]. These results suggest sources of UHECRs are nearby in the local supercluster ($\lesssim$100 Mpc). If galactic and extragalactic field models are correct a light cosmic ray composition should become anisotropic at the highest energies. As discussed at length in Chapter 8 TA has published evidence of an anisotropy in arrival directions of UHECR that does not rule out sources within this radius [27].

Results from Fly's Eye, HiRes, and TA, indicated a predominantly light composition of cosmic rays [69] [39] [68]. PAO's hybrid publication in 2012 also states that for UHECR of energy 10^{18} to $10^{18.5}$ eV the X_{max} distribution is compatible with a large fraction of protons with a somewhat heavier composition at higher energies [112]. PAO also suggests that the composition is changing to a heavier composition with higher energy due to the RMS of the X_{max} distribution [40]. This is analyzed in detail in Section 13.1.3 using TA data.

13.1 Data Compared to Simulation

The values of X_{max} for any particular primary particle have statistical fluctuations. Though heavy primaries have a narrower distribution, with an average X_{max} higher in the atmosphere, while protons will interact more deeply, with a wider distribution (see Section 2.3.4), the distributions have significant overlap. Indirect detection techniques are unable to determine an individual UHECR's mass due to these large statistical fluctuations inherent to extensive air showers (EAS). Hence, the distribution of a large number of measurements must be used to make inferences about composition.

13.1.1 Full Distribution Comparison

Figure 13.1 shows X_{max} distributions within 0.2 $\log_{10}$(E/eV) energy bins (Figure 13.1e is E$>10^{19.2}$ eV). The Cramér-von Mises (CvM) test result p-value is shown on each plot [80]. The CvM-test statistic uses the integral difference squared of the empirical cumulative distributions being compared (as opposed to the maximum difference of the cumulative distributions used in the Kolmogorov-Smirnov (KS) test). The CvM-test is a more powerful test that is more sensitive to the tails of the distributions, and less biased towards the median, than the KS-test [113].

These show that data is incompatible with QGSJETII-03 iron for all energies, while being in good agreement with proton primaries, using a full distribution test. All deviations from pure iron are greater than 10σ significance, while all deviations from pure proton are less than 2σ.

13.1.2 Distribution Moments Comparison

Figure 13.2 shows the typical distribution moment plots traditionally used in composition analysis due to low statistics. These figures compare data with QGSJETII-03 proton, nitrogen, and iron. The elongation plot in Figure 13.2a shows how the mean of the X_{max} distribution changes with energy. Figure 13.2b is a similar plot using the median value of the X_{max} distribution at each energy. Figure 13.2c shows the RMS deviation using bins of equal number of events as the error on the RMS is large for bins with low statistics.

In the elongation figures using mean, and median, X_{max} the data appears to be statistically compatible with a pure proton QGSJETII-03 composition. The elongation linear fit

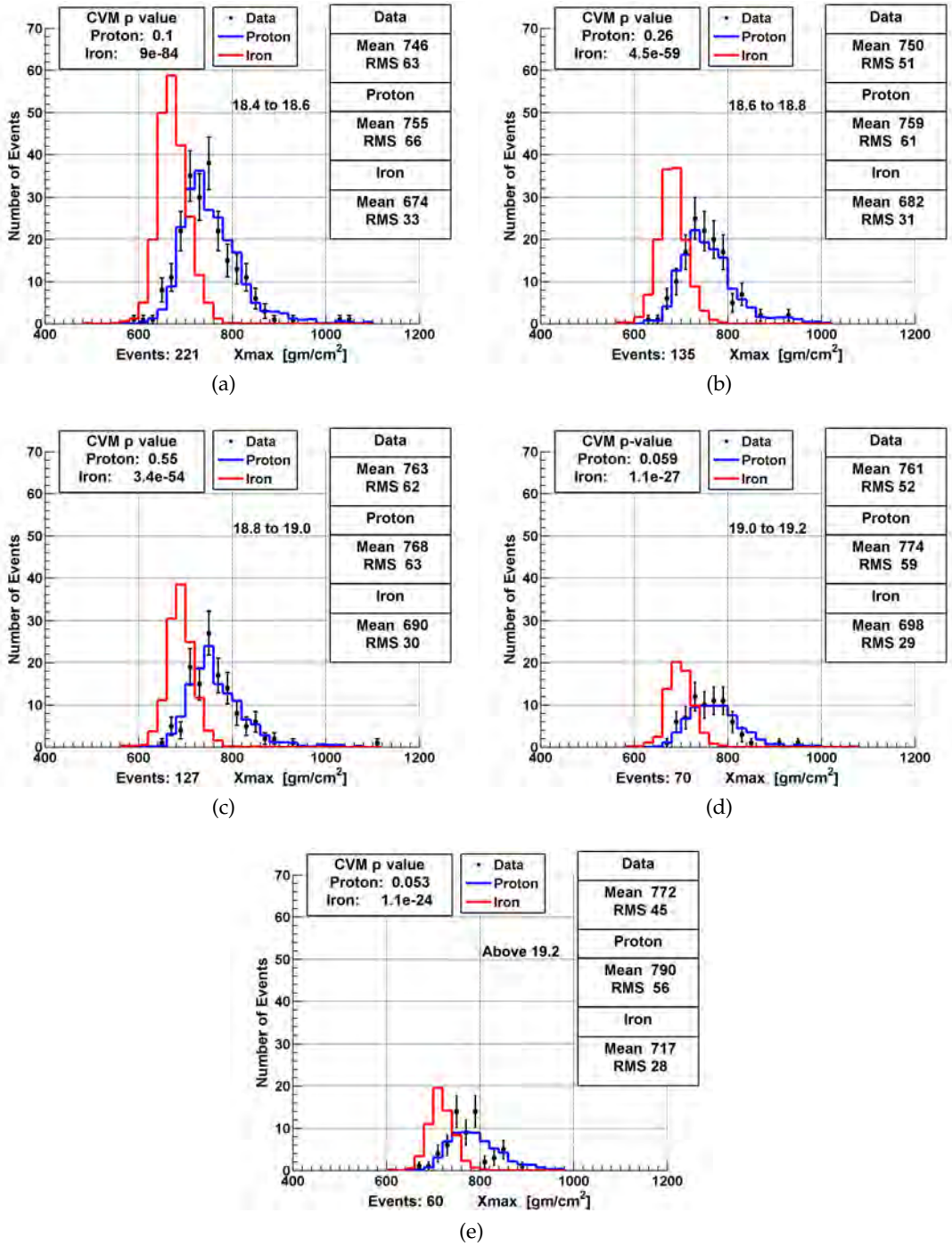

Figure 13.1: Full X_{max} distributions from the data (black points), QGSJETII-03 proton MC (blue), and iron MC (red) binned by 0.2 in $\log_{10}$(E/eV). Figure (e) is events with energies E$\geq 10^{19.2}$ eV. The MC has been normalized to the area of the data. The CvM-test p values show good agreement between data and proton. The p values show no agreement with iron.

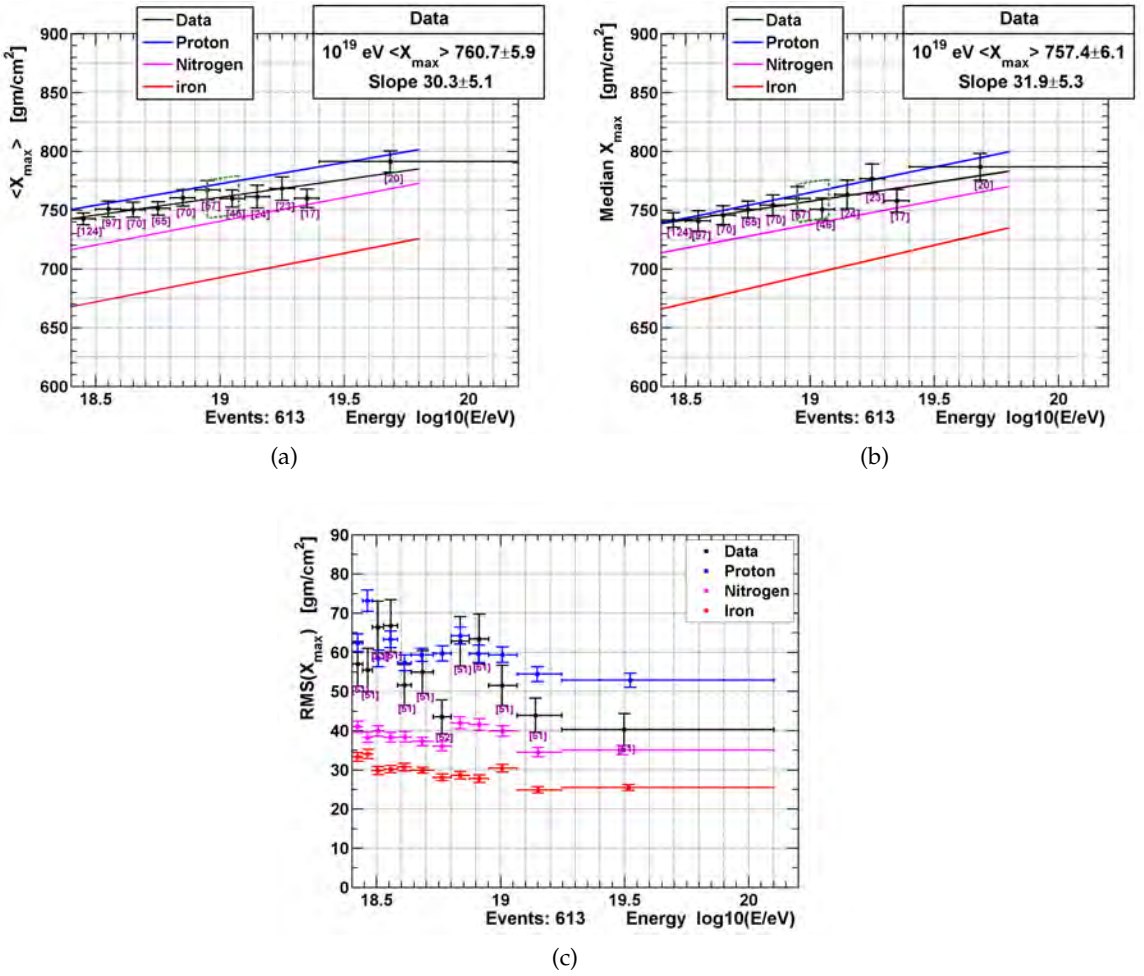

Figure 13.2: X_{max} distribution moment plots commonly used for composition analysis – (a) is the mean, (b) is the median, and (c) is the RMS. Shown are data (black), QGSJETII-03 proton MC (blue), nitrogen (magenta), and iron MC (red). These show agreement between data and proton MC while showing disagreement with iron. The green hashed box indicates the total systematic error on $\langle X_{max} \rangle$.

appears to be moving towards nitrogen at higher energies but this is within the statistical error of the fit. Though, referencing Figure 2.5, which shows the spread of the various models, it appears that a strong nitrogen composition at the highest energies could be possible for models such as SYBILL 2.1 (or EPOS) but even with these models the data is only approximately one, or two, error bars (including systematic and statistical uncertainty) from pure proton.

From the RMS plot of Figure 13.2c it would appear by eye that the composition is indeed getting heavier with energy but further statistical analysis, done in the following

section, shows that this is not strong evidence of a changing composition.

13.1.3 Composition without Mean X_{max}

In all models of EAS, discussed in Section 2.3.6, particle interaction parameters have been extrapolated from lower energy Large Hadron Collider (LHC) data. These model parameters include charged particle multiplicity, cross section, and elasticity (and more) of proton-proton interactions. Due to this it has been shown that there is a systematic uncertainty on $\langle X_{max} \rangle$ with a *lower bound* of about $\sim$20 g/cm^2 for proton primaries [114] [115] [116]. This lower bound is even larger with nuclei primaries such as nitrogen and iron.

Adding in quadrature the experimental systematic uncertainty ($\sim$16 g/cm^2), statistical uncertainty ($\sim$4 g/cm^2), and the lower bound uncertainty for proton primaries results in a total uncertainty greater than $\sim$25 g/cm^2. This means that all models are within $\sim 1.5\sigma$ uncertainty and composition interpretations involving the X_{max} distribution location (mean, median, CvM-test, etc) must give all models equal weight (see elongation Figure 2.5).

For example, if the data distribution of Figure 13.1e, with a σ deviation from QGSJETII-03 proton less than 2σ, is shifted by 25 g/cm^2 then the result is a significance disagreement of $\sigma > 5$. Whether these distributions belong to the same parent distribution, or not, cannot be determined within just 1σ of the model parameter uncertainty.

13.1.3.1 Solution: Shifting L-test

Fortunately, the experimental systematic, statistical, and systematic model parameter uncertainties on the RMS of X_{max} is smaller than that of $\langle X_{max} \rangle$ [115]. To test whether data and MC come from the same parent distributions with the same higher moments (than $\langle X_{max} \rangle$) a new statistical test must be used. The L-test was developed for this thesis and gives the probability that two distributions come from the same parent location family of distributions. It is described in detail in Appendix B. The "location" of a probability density function is the parameter that defines its mode. An example of a location family of distributions would be Gaussian distributions with different means but the same standard deviations.

In addition to the L-test, O'Brien's test for homogeneity of variance is also used in this section for comparison. O'Brien's test is a multisample test for equality of variances – that

is it gives the probability that any number of sample sets all belong to parent distributions with the same variance [117] [118]. Due to the fact that this only tests one moment of the distributions it generally reports greater agreement than the L-test (at least in the case of X_{max}).

Figure 13.3a is a "shift plot," that plots the L-test "shift" (the number of g/cm^2 subtracted from the MC distribution that minimizes the CvM-test statistic), and makes use of the entire distribution within each energy bin (instead of breaking them down into component moments as in Figure 13.2). The colored areas show the range of shift required for QGSJET-01c [47], QGSJETII-03 and 04 [119], Sibyll 2.1 [48], and EPOS [49] proton, and iron. The shift is a robust measure of distance between the parent distribution locations (more accurate, and more precise, than the mean or median distance) as shown in Section B.1.3.

Also, displayed are QGSJETII-03 rails for proton, nitrogen, and iron. The colored data points, described by the scale on the right, give the σ significance deviation calculated from the probability that the two distributions belong to the same parent location family, independent of distribution locations (a test of moments higher than the mean). The first three black iron data points are a minimum 5.9σ (the p-value is calculated by bootstrap

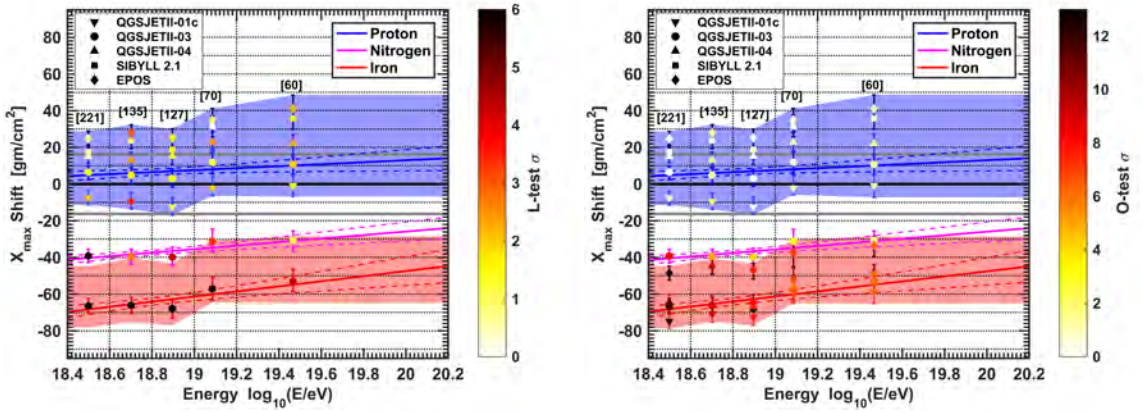

(a) (b)

Figure 13.3: X_{max} distribution shift plots – σ-significance of data deviation from MC independent of distribution location and the "shift" (a robust measure of the distance between population modes). Areas are proton (blue), iron (red), using various models. Solid lines are QGSJETII-03 (magenta is nitrogen) with dashed uncertainties. Grey lines are $\langle X_{max} \rangle$ systematic uncertainty. (a) L-test shift plot. Color scale is data deviation from MC σ-significance independent of distribution location. First three iron black circles are σ>5.9. (b) Same shifts as (a) where the color scale is O'Briens test of variance for comparison [117].

and was stopped at one billion trials). This shows that after shifting iron up $\sim$60 g/cm^2 the distribution shape is still incompatible with data at a greater than 4σ significance for all energies.

Figure 13.3b is a "shift plot" that plots the L-test "shift" along with a color scale of p values converted to σ deviation from O'Brien's test of variance. This shows that the L-test results are reasonable and also gives a better lower limit to the iron significance of the first three energy bins ($\sigma > \sim 8$).

It would appear that there is some indication of the data distribution getting heavier with energy as the L-test deviation from QGSJETII-03 nitrogen is only 1.1σ. Figure 13.4a shows the significance of L-test deviations for proton from all considered models (same values as Figure 13.3a). Given that there systematic and statistical uncertainties in the X_{max} RMS an L-test σ deviation less than 3.5σ should probably be considered good agreement. The average significance for the last energy bin is 1.8σ and given the statistical uncertainties shown, along with the systematic uncertainty in RMS, there is no statistically significant evidence of a change in composition.

Furthermore, as O'Brien's test is a multisample test it can be used to determine if the RMS, of any energy bin, is statistically different from any other energy bin – the result of this data/data comparison is a 0.97σ significance of any change in X_{max} population RMS.

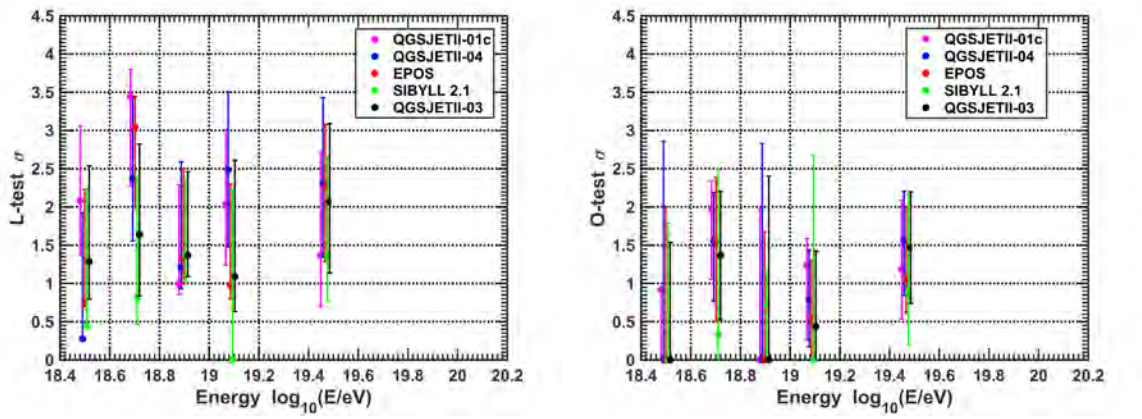

(a) (b)

Figure 13.4: σ-significance of data deviation from proton MC of various models independent of distribution locations. (a) L-test σ-significance of higher moments. (b) O'Brien's variance test.

13.2 Conclusion

This thesis introduced the pattern recognition QFA analysis that reduces X_{max} resolution (and bias) change with energy. This was done so that a change in composition with energy could be more accurately measured. Also, introduced is the two-sample L-test described in Appendix B, and the"shift plot," that utilizes the full distribution change with energy to determine agreement between data and Monte Carlo simulation. Using 7 years of hybrid FD/SD data it is found that a light, nearly pure proton composition is in good agreement with the data and iron is ruled out as a significant primary of UHECR for all models considered. Finally, using statistical tests that are independent of distribution location it is shown that the TA UHECR data is statistically (and systematically) compatible with pure proton, for all models, and all energies.

PART IV

SUMMARY

CHAPTER 14

SUMMARY

A significant feature suggestive of possible energy dependent magnetic deflection has been observed in 7 years of Telescope Array (TA) surface detector (SD) ultra-high energy cosmic ray (UHECR) events E$\geq 10^{19.1}$ eV, that appears as a deficit of low energy events with energies E$< 10^{19.75}$ eV, and an excess of events with energies E$\geq 10^{19.75}$ eV in the same region of the sky. The maximum anisotropy is at 142° R.A., 40° Dec. with a local pre-trial one-sided significance of σ_{local} = 7.11σ. The global posttrial one-sided significance of an event density asymmetry anisotropy of this magnitude appearing by chance in an isotropic cosmic-ray sky was found to be 5.12σ (p=1.56$\times 10^{-7}$). This feature is the combination of an energy spectrum anisotropy and an energy-distance correlation.

This region includes the Hotspot shown using a new kernel density estimation method in Chapter 8 with a 3.65σ significance. It also includes an energy spectrum anisotropy shown using a new equal exposure method in Chapter 9 with a 3.74σ significance, and an energy-distance correlation, shown by a new double correlation method in Chapter 10, with a 3.37σ significance. The combined significance of the energy anisotropies, assuming independent tests by Stouffer's method, is 5.03σ which is close to the Hot/Coldspot 5.12σ. This supports the assertion that the Hot/Coldspot is the combined result of the energy spectrum and energy-distance correlation anisotropies. The significance of these anisotropies has been increasing steadily as more data is taken.

Systematic checks comparing the shower geometry variable (azimuth, zenith, core position etc.) distributions inside the anisotropic area, to outside, show no disagreements (nor are there disagreements between the different energy ranges inside the area) – they all also agree with isotropic Monte Carlo (MC) simulation. The R.A., trigger time, and Dec. distributions inside the area with Hotspot bin energies agree well with the Coldspot energy bin events – they also agree with isotropic MC. The full energy distributions agree

well between different seasons inside and outside. Also, energy corrections applied to account for hourly, and seasonal, variations in average surface detector signal result in no significant change to the significances of the anisotropies. Furthermore, no anisotropies are seen when events are plotted in anti-sidereal time – as should be the case if they are real and not the result of some kind of seasonal variation.

The location of the Hot/Coldspot anisotropy is 24° from the supergalactic plane which contains local galaxy clusters such as the Ursa Major cluster (20 Mpc from Earth), the Coma cluster (90 Mpc), and the Virgo cluster (20 Mpc). It has been reported, using a method reminiscent of the energy-distance correlation, that the most likely source of the Hotspot events is the closest starburst galaxy M82 that is only 3.4 Mpc away [29] [30].

An extended feature that appears to be correlated with supergalactic structure can be seen if the significances of Hot/Cold locations in Figure 9.9, or 11.7, (which is nearly the entire contiguous $\sigma>0$ area around the maximum) are converted to supergalactic coordinates and fit to a straight line (weighted by σ^2). The result is a line parallel to the supergalactic plane with zero slope shifted $\sim$-16° in supergalactic declination. Supergalactic magnetic sheets that can focus cosmic ray flux, that have an effect for E>50 EeV, has been discussed in [8] and deflection of lower energy background events transverse to the sheet is discussed in [10].

If highest energy UHECR are predominately protons as indicated by Chapter 13 (independent of model for all energies), and previous TA studies, this feature may also be associated with the closest galaxy groups and/or the galaxy filament connecting us with the Virgo cluster [120] [29] [30]. If the anisotropic cosmic rays are heavy nuclei, they may originate near the supergalactic plane and be deflected by extragalactic magnetic fields (EGMF) and the galactic magnetic halo field (GMF) [121] [122]. Whether magnetic deflection or focusing is the mechanism, the magnitude is expected to be energy dependent. The energy-distance correlation is direct evidence of energy dependent magnetic field deflection.

To determine the origin of this feature, we will need greater UHECR statistics in the northern sky. Better information about the mass composition of the UHECRs and the configurations of GMF, and EGMF is also important. The TAx4 expansion, which will expand the TA detection grid by a factor of four is designed to provide the equivalent of

20 TA-years of SD data by 2019 [123], this could possibly yield a $>7\sigma_{global}$ observation if the ratios of the Hot/Coldspot to background events remains as is currently seen (and $>5\sigma$ for the other energy anisotropies). TA$\times$4 and other related projects will enable us to make an even more precise UHECR anisotropy map with high statistics and help further solve the mystery of the UHECR origin and composition.

APPENDIX A

POISSON LIKELIHOOD RATIO GOODNESS OF FIT

Binned likelihood ratio tests give the probability that a distribution of event frequencies follow an expected distribution. The most well known true goodness-of-fit (GOF) test that gives this probability is the Pearson's χ^2 test, usually called simply the χ^2 test.

The χ^2 test requires a large enough observed sample size that the binned expected distribution event frequencies follow the assumption of independent normally distributed data. For small observed frequencies this assumption is violated and the binned Poisson maximum likelihood ratio GOF test is required.

A binned likelihood ratio test is required as unbinned maximum likelihood fits do not tell you how well the fit follows the data (i.e. there is no standard probability distribution). The likelihood at its maximum does not behave as a GOF statistic [124] [125].

Nor is the usual recommendation of finding the probability distribution of the maximum likelihood via Monte Carlo methods reliable [126] (Note: Opening the file downloaded by clicking the bibliography URL download link requires its file extension to be changed from ".ps.gz" to ".ps").

Unbinned non-parametric (not assuming Gaussian) GOF tests such as Kolmogorov-Smirnov (KS) [127], Cramér-von Mises (CVM) [80], and Anderson-Darling (AD) [128] tests all use test statistics found from empirical cumulative distributions that are normalized to a maximum probability of one. The result is that these are comparisons of distribution shapes and not relative frequencies. That is when comparing two distributions what is returned is the probability that both distributions came from the same parent distribution, not the probability that they are the same distribution.

For instance if a data set of 100 observed events (that follow a Gaussian distribution with $\mu = 0$ and $\sigma = 1$), but the expected distribution was only 10 events (that follow a

Gaussian distribution with $\mu = 0$ and $\sigma = 1$), an unbinned non-parametric test would show perfect agreement while the Binned Poisson Likelihood Ratio test would report a large disagreement.

A.1 Derivation

In the histogram case the likelihood ratio, λ, is the ratio of the likelihood (probability density function) of the null hypothesis (that the observed events histogram bins come from the expected distribution) to the likelihood of the alternative hypothesis (bins from distributions exactly as observed). According to Wilks' Theorem as the total observed sample size, N, of a distribution approaches ∞ the log-likelihood ratio test statistic , $-2\log(\lambda)$, approaches a χ^2 distribution with degrees of freedom N_{bin} [129]. From this the p-value of the agreement between two histograms can be found.

Each bin follows a Poisson distribution random number in the case of small observed statistics. The null hypothesis is that each observed bin is sampled from a Poisson distribution with the expected mean (Equation A.1a) and its likelihood is the probability of the measured count, n_i, given the expectation, μ_i. The alternative hypothesis is that the observed data bins follow Poisson distributions with different than expected with means that are exactly as measured, $\mu_i = n_i$ (Equation A.1b). This alternative hypothesis is the maximum likelihood.

$$f_i(n_i, \mu_i) = \frac{\mu_i^{n_i} e^{-\mu_i}}{n_i!} \tag{A.1a}$$

$$f_i(n_i, ni_i) = \frac{n_i^{n_i} e^{-n_i}}{n_i!} \tag{A.1b}$$

The "log-likelihood" of the null hypothesis expectation for a single bin is shown in Equation A.2 as it is the log-likelihood that is made use of in Wilks' theorem approximation to the χ^2 distribution.

$$\log[f_i(n_i, \mu_i)] = \log\left(\frac{1}{n_i!}\right) + n_i \log(\mu_i) - \mu_i \tag{A.2}$$

The overall likelihood ratio, λ, of a histogram is the likelihood ratios of all bins multiplied, $\lambda = \prod \lambda_i$, just as independent probabilities multiply. Applying Wilks' theorem to the ratio of two histograms as a whole results in Equation A.3a.

The final result is shown in Equation A.3b where the μ_i are the counts in bins of the expected distributions histogram and the n_i are the counts in bins of the observed distributions histogram. For the bins where $n_i = 0$ the limit is taken so that $\chi_i^2 = 2\mu_i$.

$$\chi^2(N_{bins} - 1) \simeq -2\log\left[\prod_{i=1}^{N_{bins}} \frac{f_i(n_i, \mu_i)]}{f_i(n_i, n_i)}\right] = -2\sum_{i=1}^{N_{bins}} \frac{\log[f_i(n_i, \mu_i)]}{\log[f_i(n_i, n_i)]} \tag{A.3a}$$

$$\chi^2(N_{bins}) \simeq 2\sum_{i=1}^{N_{bins}} n_i \log(\frac{n_i}{\mu_i}) + \mu_i - n_i \tag{A.3b}$$

Further detail regarding this GOF test may be found in [91] and [92].

A.2 Caveat

One should be aware of the deviations from the χ^2 approximation that occur with small expectation bin counts (not the observed), $\mu \lesssim 5$, when using this goodness of fit test – what follows in this section is taken from [93].

A.2.1 Mean $\langle -2\log(\lambda)\rangle$

The mean value of the χ^2 distribution for one degree of freedom is exactly one. Using this fact we can quantify, for a single histogram bin, exactly how fast $\langle -2\log(\lambda)\rangle$ approaches the χ^2 distribution. For small values of μ the infinite sum of Equation A.4a for $\langle -2\log(\lambda)\rangle$ converges quickly and is very accurate using only $\sim$20 terms. Equation A.4b shows the asymptotic nonconverging series of $\langle -2\log(\lambda)\rangle$ that is reasonably accurate using only $\sim$10 terms for $\mu \gtrsim 5$.

$$\langle -2\log(\lambda)\rangle = 2e^{-\mu}\sum_{k=0}^{\infty}[(\mu - k) + k\log(k/\mu)]\frac{\mu^k}{k!} \tag{A.4a}$$

$$\langle -2\log(\lambda)\rangle \simeq 1 + \sum_{k=1}^{\infty}\frac{a_{k+1}k!}{\mu^k}\ ,\ a_j = -\sum_{i=0}^{j-1}\frac{a_i}{j+1-i} \tag{A.4b}$$

From this it is immediately apparent that $\langle -2\log(\lambda)\rangle$ asymptotically approaches 1 from above as $\mu \to \infty$. Figure A.1 shows a plot of this function. On average there is an underestimation of the χ^2 for bins with $\mu \lesssim 0.5$ and the maximum positive bias is at $\mu \approx 1.33$.

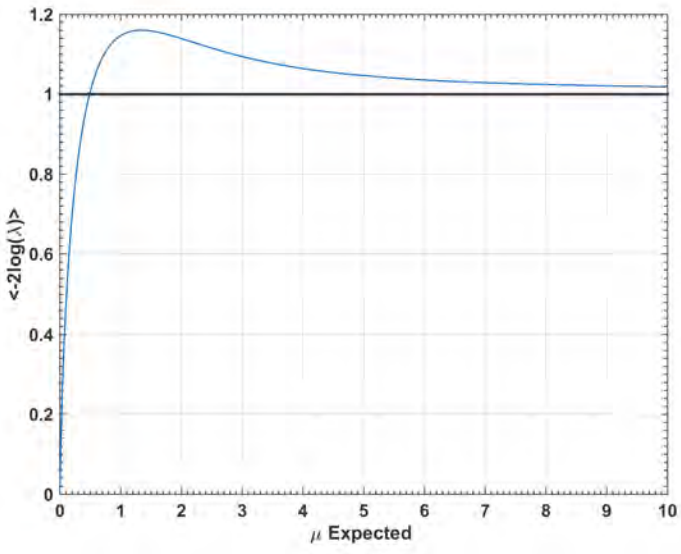

Figure A.1: The single histogram bin bias of the $-2\log(\lambda)$ Poisson likelihood ratio χ^2 estimation. On average there is an underestimation of the χ^2 for bins with expectation counts $\mu \leq \sim 0.5$ and the maximum positive bias is at $\mu \approx 1.33$. It approaches the $\langle \chi^2 \rangle = 1$ for $\mu \to \infty$.

On the other hand the mean value of the classic Pearson's χ^2 is shown to equal to 1 for every value of the expectation μ in Equation A.5.

$$\left\langle \frac{(n-\mu)^2}{\mu} \right\rangle = \frac{e^{-\mu}}{\mu} \sum_{k=0}^{\infty} (k-\mu)^2 \frac{\mu^k}{k!} = 1 \tag{A.5}$$

A.2.2 Variance $Var(-2\log(\lambda))$

The variance of the χ^2 distribution for one degree of freedom is 2. This can be used to quantif how fast $Var(-2\log(\lambda))$ approaches the χ^2 distribution. For small values of μ the infinite sum of Equation A.6a for $\langle -2\log(\lambda) \rangle$ converges quickly and is accurate using only $\sim$20 terms.

$$\langle -2\log(\lambda) \rangle = -\langle -2\log(\lambda(\mu)) \rangle^2 + 4e^{-\mu} \sum_{k=0}^{\infty} [(\mu - k) + k\log(k/\mu)]^2 \frac{\mu^k}{k!} \tag{A.6a}$$

$$Var(-2\log(\lambda)) \simeq 2 + \frac{2}{3}\mu^{-1} + \frac{4}{3}\mu^{-2} + \frac{701}{180}\mu^{-3} + \frac{449}{30}\mu^{-4} + ... \tag{A.6b}$$

Equation A.6b shows the asymptotic series of $Var(-2\log(\lambda))$ that was plotted using only ~ 5 terms for $\mu \gtrsim 7.5$. It can be seen that $Var(-2\log(\lambda))$ asymptotically approaches 2 from above as $\mu \to \infty$.

The variance of χ^2 is shown in Equation A.7 and approaches infinity as $\mu \to \infty$.

$$Var\left(\frac{(n-\mu)^2}{\mu}\right) = \frac{e^{-\mu}}{\mu^2}\sum_{k=0}^{\infty}(k-\mu)^4\frac{\mu^k}{k!} - 1 = 2 + \frac{1}{\mu} \tag{A.7}$$

Figure A.2 is plot of these two variance functions. The $-2\log(\lambda)$ variance is less than χ^2, for bins with $\mu \leq \sim 1.6$, and the maximum variance is at $\mu \approx 3$. The variance for χ^2 is greater than that of the Poisson likelihood ratio for $\mu \leq \sim 2.6$.

A.2.3 Conclusion

In the histogram case the total mean, and variance, of $-2\log(\lambda)$ is simply the values of the separate bins added. The recommendation is that no bin should have an expected value, μ, less than 0.5 so that the bias as shown in Section A.2.1 does not change sign between bins.

Section A.2.2 shows that $\mu = 0.5$ is close to a local minimum for the variance of $-2\log(\lambda)$ and is less than $1/2$ that of the χ^2 distribution. Bins with expectation $\mu \leq 1$ were combined into adjacent bins for the analysis of Chapter 9 so that fluctuations of larger statistics bins don't hide deviations in the small statistics bins. The result is that less than $\sim$15% of bins have $\mu \leq 3$ which is a good rule of thumb to follow.

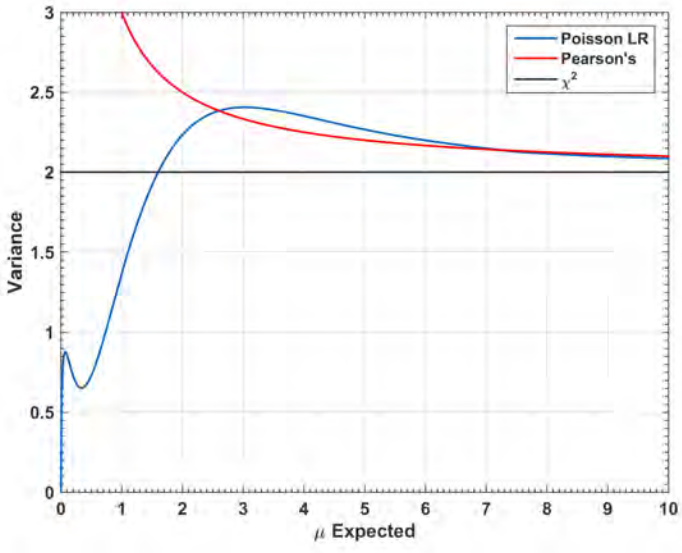

Figure A.2: Single histogram bin variance of the $-2\log(\lambda)$ Poisson likelihood ratio χ^2 estimation. The variance is less than χ^2 for bins with expectation counts $\mu \leq \sim 1.6$ and the maximum variance of 2.4 is at $\mu \approx 3$. It approaches the $Var(\chi^2) = 2$ for $\mu \to \infty$. Pearson's χ^2 variance is greater for $\mu \leq \sim 2.6$

APPENDIX B

L-TEST

Two sample unbinned nonparametric (not assuming Gaussian) goodness of fit tests such as Kolmogorov-Smirnov (KS) [127], Cramér-von Mises (CvM) [80], and Anderson-Darling (AD) [128], all use test statistics found from empirical cumulative probability distribution functions. They give the probability that both distributions are from the same parent distribution.

It may often be the case that one wants to compare two distributions where the relative biases of the different experiments is unknown. Such is sometimes the case with the ultra-high energy cosmic ray X_{max} variable used to find the composition of cosmic rays in a statistical manner. There are also various models of primary particle compositions used in these X_{max} distribution comparisons and these models have a much larger variance in the mean $\langle X_{max} \rangle$ than the higher moments of their distributions [114]. If there are enough statistics in a data set it may also be of interest to do X_{max} composition anisotropy on the sky where the $\langle X_{max} \rangle$ is known to be temperature dependent which causes a relative bias in right ascension due to the seasons.

These issues translate into uncertainties in the location (mean, median, or mode depending on the distribution) parameter of the probability density function (PDF). Probability distributions are most generally described by three parameters – location, scale, and shape. The Gaussian distribution for instance has a location parameter μ (which happens to be its mean) and a scale parameter σ^2 (which happens to be its variance). The skewness and kurtosis (and all higher moments) of the Gaussian distribution are constants because it does not have a shape parameter and only it's location and scale can change.

What follows is a description of a new unbinned nonparametric goodness of fit test which is location insensitive. It is an attempt to resolve the currently intractable issues described above, which affect the locations of two X_{max} distributions to be compared,

much more than their higher moments. This is done by shifting the distribution location until the CvM-test T-statistic (the squared integral difference of the empirical cumulative distribution functions) is minimized, $T_{min} = L$, then calculating the probability of the remaining disagreement.

This can be seen as a two sample nonparametric analog to a test of normality, for which the location of the distribution also does not matter (only that the moments higher than the scale are consistent with the constant values of a Gaussian) – though for the L-test both the scale and shape are variable.

The question to be answered is – what is probability that the two distributions are samples of the same location family parent distribution $D_{z_0} = D(z - z_0)$? In the case of this thesis this is used in Chapter 13 to answer the question of whether the TA ultra-high energy cosmic ray data is compatible with the proton composition location family parent distribution (as described by all models).

B.1 L-Test

The basis of the L-test statistic is a minimization of the two sample Cramér-von Mises (CvM) statistic shown in Equation B.1 for the case of two histograms [80]. Tables used to find p-values from this statistic for the CvM-test can be found in [94].

The CvM-test statistic is chosen as the basis for the L-test as it has been shown to be more robust in general than the KS-test statistic [113]. The KS-test statistic is the maximum difference between the two empirical cumulative distribution functions (ECDF) – this statistic is biased towards detecting differences of location more than the higher moments. The CvM-test is much more sensitive to deviations between ECDF that have the same location (median, mean, etc.). The intention with the L-test is to force, by Equation B.2, the locations of the distributions to be the same so the KS-test statistic is not optimal.

Also, the CvM-test statistic is used because the Anderson-Darling test statistic A is the CvM T-statistic weighted so the tails contribute more to the integral [128]. By shifting distributions to find the minimum A the relative weights of data samples would change for every shift tested. This increases the uncertainty of the resulting shift if it should be of interest. This shift, S, is a robust estimate of the distance between the modes of the

continuous parent distributions of the two ECDF. A minimum uncertainty on the resulting shift, S, is desirable as it may be useful for calibration purposes, or further confidence that the two distributions have a different or the same parent distribution.

B.1.1 CvM-Test Statistic

In Equation B.1 $F(x)$ and $G(y)$ are the empirical cumulative distribution functions (ECDF) for each distribution. The ECDF's are the normalized cumulative sum of a histogram calculated with bin edges at every value of the two samples combined. Sample one has measurements $x = (x_1, x_2, x_3...)$ with a cumulative distribution function (CDF) F, and the second sample has $y = (y_1, y_2, y_3...)$ has a CDF G. Their union, which is used for the bin edges of the CDF's, is z = (x,y).

$$T = \frac{N1N2}{(N1+N2)^2} \sum_{k=1}^{N1+N2} [F(z_i) - G_k(z_i)]^2 = \frac{N1N2}{(N1+N2)^2} \left\{ \sum_{i=1}^{N1} [F(x_i) - G(x_i)]^2 + \sum_{j=1}^{N2} [F(y_j) - G(y_j)]^2 \right\} \quad \text{(B.1)}$$

The sum in the limit of infinite samples would approach the continuous case of the integral of the differences between the CDF's squared.

B.1.2 *L*-statistic (Minimization of the *T*-statistic)

In mathematical terms the L test statistic is shown in Equation B.2. The reason for taking the *log* of the sum is that this makes the L statistic follow the Generalized Extreme Value (GEV) Distribution as should be expected for the end result of a minimization. This will be shown in Section B.1.2.1.

If two distributions have the same location the T-statistic will be close to its minimum value. Therefore, $\tilde{x} = x - median(x)$ and $\tilde{y} = y - median(y)$ are used in the T-statistic minimization as the median is a robust measurement of location.

Equation B.3b and B.3c are just the empirical cumulative distribution functions at a particular bin edge in the set $\hat{z} = (\tilde{x} - S, \tilde{y})$ after shifting.

$$L_F = \log \left\{ \min_{a \le S \le b} \frac{N1N2}{(N1+N2)^2} \sum_{k=1}^{N1+N2} [\hat{F}(S)_k - \hat{G}(S)_k]^2 \right\} \quad \text{(B.2a)}$$

$$a = min(\tilde{x}) \ , \ b = max(\tilde{x}) \quad \text{(B.2b)}$$

$$\hat{F}(S)_k = \frac{1}{N1} \sum_{j=1}^{N1} [(\tilde{x}_j - S) \le \hat{z}(S)_k] \ , \ [x] = \begin{cases} 1 \ if \ True \\ 0 \ if \ False \end{cases} \quad \text{(B.2c)}$$

$$\hat{G}(S)_k = \frac{1}{N2}\sum_{j=1}^{N2}[\tilde{y}_j \leq \hat{z}(S)_k] \tag{B.2d}$$

This leaves the question of how to find the minimum of the non-local $T(x,y) \rightarrow T(x - s_{min}, y) = L$ for empirical CDF's. To get a robust result two different minimization functions with different bounds or starting points were used and the smallest L_i is considered the actual L.

One is a minimizer that uses an algorithm based on golden section search and parabolic interpolation (Brent's method) [130]. This function is used with a bound of $a = min(\tilde{x})$ to $b = max(\tilde{x})$. The second is a minimizer that uses a simplex search method [131]. This function is used twice with the starting point at a and the starting point at b.

B.1.2.1 *L*-statistic Distribution

It is unknown at this time if there is a general distribution-free limiting distribution for the L statistic (distribution-free means not dependent on the parent distributions of F and G). In the meantime a direct solution is a bootstrap calculation for any given distribution G which is the larger of the two samples. Some preliminary work has been done in fitting the resulting expected distributions for various probability distribution functions that will be shown in a following subsection.

The question to be answered is – are the two sample distributions from the same location family parent distribution $D_{z_0} = D(z - z_0)$? The parent distribution of G can be approximated by taking bootstrap samples (that is sampling with replacement), $Y1_i$ from y the size of distribution F, and $Y2_i$ from y the size of distribution G then calculating the L statistic. This is shown in Equation B.3.

$$L_i = \log\left\{\min_{a_i \leq S \leq b_i} \frac{N1N2}{(N1+N2)^2}\sum_{k=1}^{N1+N2}[\hat{G1}^i(S)_k - \hat{G2}^i(S)_k]^2\right\} \tag{B.3a}$$

$$\hat{G1}^i(S)_k = \frac{1}{N1}\sum_{j=1}^{N1}[((\tilde{Y1}_i)_j - S) \leq (\hat{Z}_i)(S)_k] \tag{B.3b}$$

$$\hat{G2}^i(S)_k = \frac{1}{N2}\sum_{j=1}^{N2}[(\tilde{Y2}_i)_j \leq (\hat{Z}_i)(S)_k] \tag{B.3c}$$

The estimated probability that F and G are two samples from the same location family parent distribution $D_{z_0} = D(z - z_0)$ is shown in Equation B.4. $L_F = L_{Observed}$ and $L_{Expected}$ is the bootstrap sampled set of the L_i.

$$p\text{-}value = \frac{1}{N}\sum_{i=1}^{N}[L_i \geq L_{Observed}] \tag{B.4}$$

B.1.3 Shift: A Robust Measure of Distance

The shift, S, in Equation B.2 is a robust measure of the distance between the locations of the parent distributions of F and G. This can be shown by generating many samples from two distributions with a known distance and comparing the average shift with the average differences between the sample medians and means. The examples used here are the X_{max} distributions of Telescope Array ultra-high energy cosmic ray data, and the reconstructed QGSJETII-03 Monte Carlo (MC) X_{max} simulations (see Chapter 13), fit to Generalized Extreme Value (GEV) PDF functions. The samples are generated from the GEV fits with the same statistics as data and MC.

Figure B.1 shows the X_{max} data and proton MC distributions fit by unbinned maximum likelihood to GEV PDFs. Figure B.1a is for energies $10^{18.8}$≤E≤10^{19} eV and Figure B.1b is for 10^{19}≤E≤$10^{19.2}$ eV.

For energies $10^{18.8}$≤E≤10^{19} eV there are 127 data events and 1015 MC events. The GEV location parameter distance is 3.5 g/cm^2. Generating GEV samples with the same GEV parameters, and statistics, 5000 times results in an average shift, $\langle S \rangle$, of 3.8±4.9(RMS) g/cm^2. Average sample mean distance is 4.49±5.48(RMS) g/cm^2. Average sample median dis-

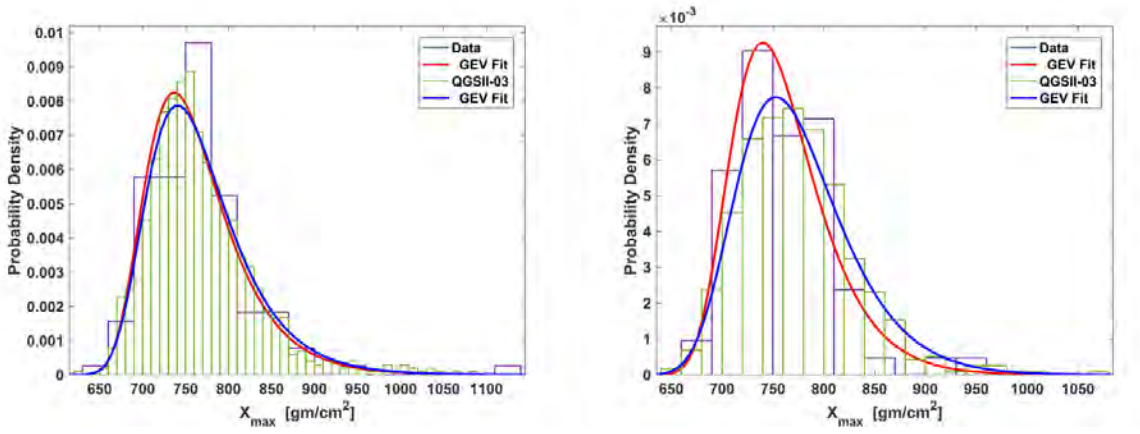

(a) (b)

Figure B.1: X_{max} data, and proton QGSJETII-03 MC, distributions in two energy ranges fit by maximum likelihood to Generalized Extreme Value (GEV) PDFs used to generate random numbers. (a) Events $10^{18.8}$≤E≤10^{19} eV. (b) Events 10^{19}≤E≤$10^{19.2}$ eV.

tance is 4.49±5.48(RMS) g/cm^2.

For energies 10^{19}≤E≤$10^{19.2}$ eV there are 70 data events and 585 MC events. The GEV location parameter distance is 11.1 g/cm^2. Generating 5000 GEV samples results in a $\langle S \rangle$ of 12.3±5.8(RMS) g/cm^2. Average sample mean distance is 14.17±6.2(RMS) g/cm^2. Average sample median distance is 13.6±7.1(RMS) g/cm^2.

Figure B.2 shows the X_{max} data and iron MC distributions fit by unbinned maximum likelihood to GEV PDFs. Figure B.2a is for energies $10^{18.8}$≤E≤10^{19} eV and Figure B.2b is for 10^{19}≤E≤$10^{19.2}$ eV.

For the energies $10^{18.8}$≤E≤10^{19} eV fit there are 127 data events and 1162 MC events. The GEV location parameter distance is -59.2 g/cm^2. Generating 5000 GEV samples results in a $\langle S \rangle$ of -64.3±5.2(RMS) g/cm^2. Average sample mean distance is -72.9±5.3(RMS) g/cm^2. Average sample median distance is -65.4±5.9(RMS) g/cm^2.

For the energies 10^{19}≤E≤$10^{19.2}$ eV fit there are 70 data events and 679 MC events. The GEV location parameter distance is -50.6 g/cm^2. Generating 5000 GEV samples results in a $\langle S \rangle$ of -55.6±6.1(RMS) g/cm^2. Average sample mean distance is -61.9±5.85(RMS) g/cm^2. Average sample median distance is -55.6±6.85(RMS) g/cm^2.

In each case the shift (S) is more accurate, and more precise, than the mean or median distance, and is within one sample RMS of the actual distance between the distribution

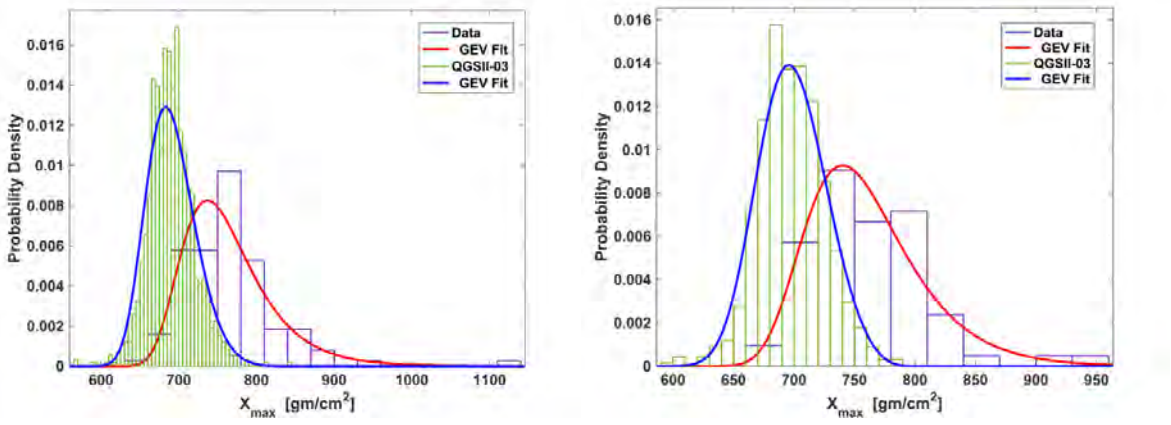

Figure B.2: X_{max} data, and iron QGSJETII-03 MC, distributions in two energy ranges fit by maximum likelihood to GEV PDFs used to generate random numbers. (a) Events $10^{18.8}$≤E≤10^{19} eV. (b) Events 10^{19}≤E≤$10^{19.2}$ eV.

locations. The same situation holds if the comparison is done between data and the other models of MC (Section 2.3.6).

B.1.4 *p*-value Calculation

As the bootstrap calculation takes a lot of computation time, it is of course of interest whether there is an equation which can relate the L-statistic to the p value directly $f(L_F, N1) = p$ for any empirical cumulative distribution functions $\hat{F}$ and $\hat{G}$.

The probability distribution of the L-statistic is the Generalized Extreme Value (GEV) distribution as it is the product of a minimization process. Many other distributions were tested and the GEV is by far the best fit for any sample size or tested distributions of $\hat{F}$ and $\hat{G}$. The GEV is the limit distribution of a set of independent and identically distributed random variables (that being the CvM-test T-statistic) and its probability distribution function (PDF) is shown in Equation B.5a. The GEV cumulative distribution function (CDF) is shown in Equation B.5b.

$$f(x;\mu,\sigma,\xi) = \frac{1}{\sigma}\exp\left\{-\left(1+\xi\frac{(x-\mu)}{\sigma}\right)^{-1/\xi}\right\}\left(1+\xi\frac{(x-\mu)}{\sigma}\right)^{-1-1/\xi} \tag{B.5a}$$

$$F(x;\mu,\sigma,\xi) = \exp\left\{-\left[1+\xi\left(\frac{(x-\mu)}{\sigma}\right)\right]^{-1/\xi}\right\} \tag{B.5b}$$

The CDF of the L statistic expectation that will be used is Equation B.6.

$$\Lambda_k = \frac{1}{N}\sum_{j=1}^{k}[L \leq L_k] \tag{B.6}$$

Some fits are shown in Figure B.3 and Figure B.4 using a single Gaussian distribution with $\sigma = 45$ and $N2 = 500$ samples for the bootstrapped sampled G, using Equation B.3. GEV fits were done for each expected distribution of L with 100,000 bootstrap samples, for a changing smaller sample of G of size $N1$.

Using these fits we can determine how the GEV distribution parameters of L change as a function of sample size $N1$. The fits are shown in Figure B.5. All fits exclude $N1<20$ as it is clear that sample sizes smaller than that do not follow the same linear trends and the p-value cannot be reliably evaluated.

Figure B.5a shows how the location parameter, μ, has an increasing linear trend with small residuals. Figure B.5b shows how the scale parameter, σ, has a decreasing linear

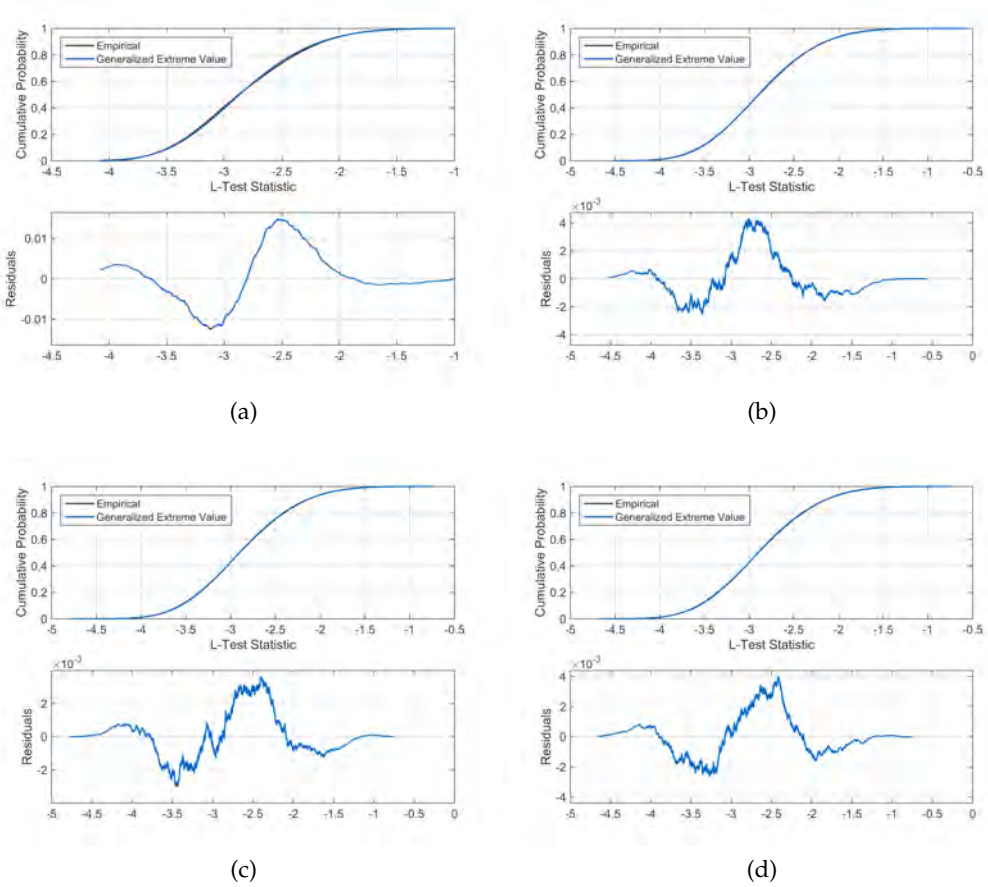

Figure B.3: Distributions of the L-statistic expectation calculated by bootstrap sampling of a Gaussian distribution of $\sigma = 45$ with $N2 = 500$ samples (G in Equation B.3) compared to the same distribution with various sample sizes $N1$. They are fitted to the GEV distribution shown in Equation B.5b. (a) $N1 = 5$ (b) $N1 = 10$ (c) $N1 = 15$ (d) $N1 = 20$. It can be seen that a sample size of $N1 = 5$ has the worst fit.

trend with small residuals. The last fit to the shape parameter, ξ, is an increasing trend with somewhat larger relative residuals shown in Figure B.5c.

Plugging Equation B.7 into Equation B.5b and subtracting from 1 could theoretically give the p-value for any given $N1$ and $L_{Observed}$ for a large sample size $N2$.

$$\xi = 9.320 \times 10^{-5} N1 - 0.2112 \tag{B.7a}$$

$$\sigma = -1.737 \times 10^{-4} N1 + 0.5296 \tag{B.7b}$$

$$\mu = 5.331 \times 10^{-4} N1 - 3.096 \tag{B.7c}$$

To compare the bootstrap method with the functional form two samples of Gaussians ($\sigma = 45$, $N1 = 50$, $N2 = 500$) were tested and the p values compared 1000 times. The resulting

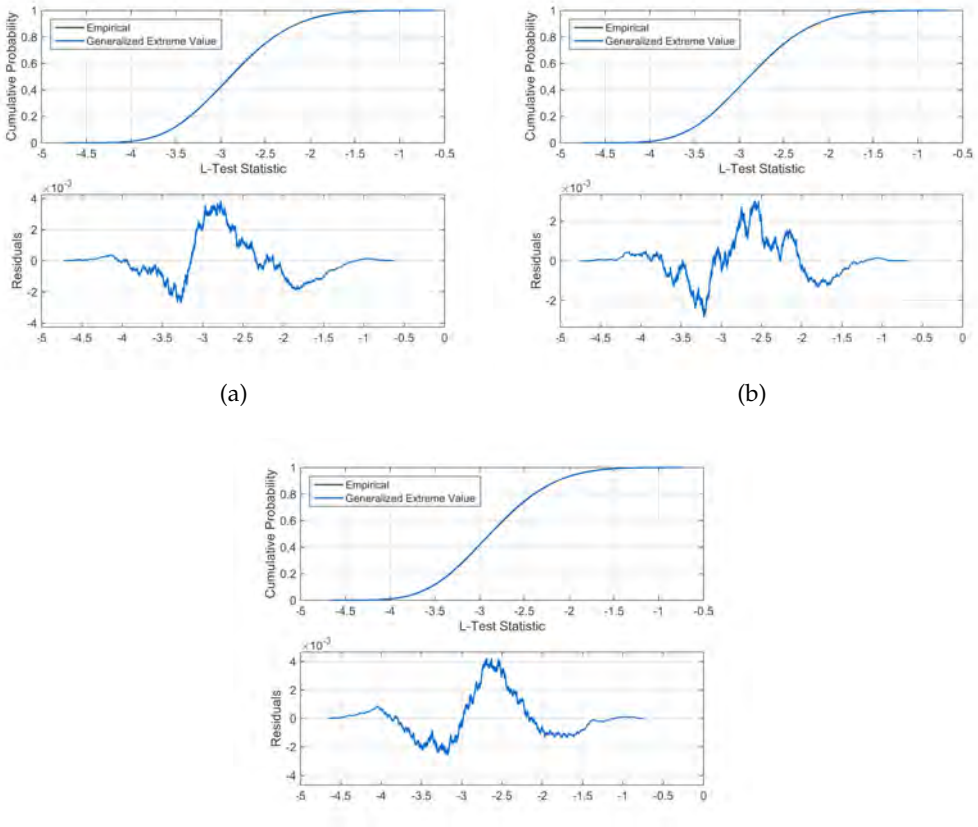

(a)

(b)

(c)

Figure B.4: Distributions of the L-statistic expectation calculated by bootstrap sampling of a Gaussian distribution of $\sigma = 45$ with $N2 = 500$ samples (G in Equation B.3) compared to the same distribution with various sample sizes $N1$. They are fitted to the GEV distribution shown in Equation B.5b. (a) $N1 = 30$ (b) $N1 = 40$ (c) $N1 = 50$.

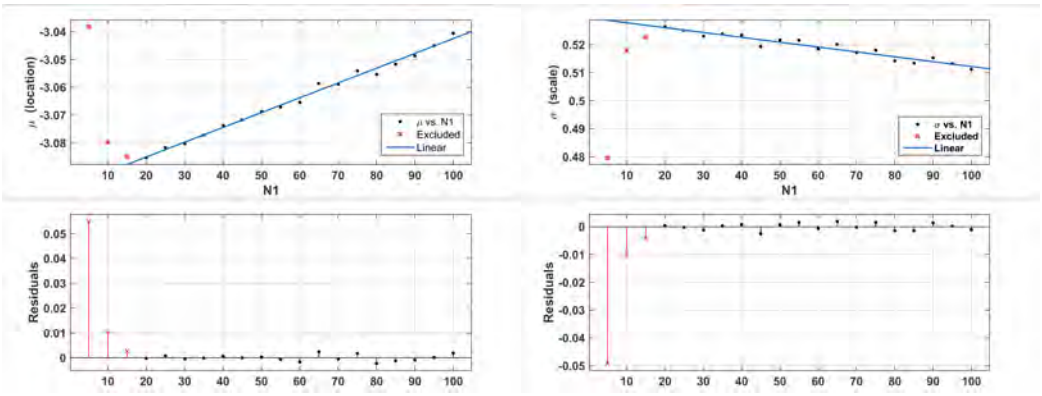

(a) (b)

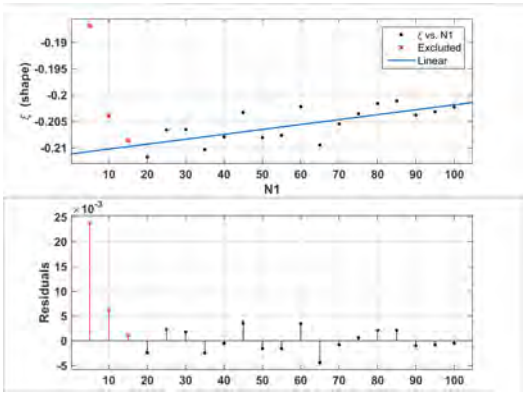

(c)

Figure B.5: Linear fits to the GEV parameters fit as shown in Figure B.4 versus the number of samples $N1$ in $\hat{F}$. (a) Location parameter μ. (b) Scale σ. (c) Shape ξ.

$p_{boot} - p_{fun}$ histogram is shown in Figure B.6a and due to the large spread of differences it is apparent that the functional form and the bootstrap results are very different. It has also been found that imaginary values can result from the functional form when the two distributions compared are from different parent PDFs.

In conclusion only the bootstrap method appears to give valid results for now. Perhaps further work can find a distribution-free form of the L-statistic expectation. The resulting σ disagreements from comparing the 1000 sets of two Gaussians is shown in Figure B.6b. The maximum was a $\sigma = 3.8$, while the mean $\langle\sigma\rangle = 1.3$, which is about the expectation if the distribution test is reasonably unbiased.

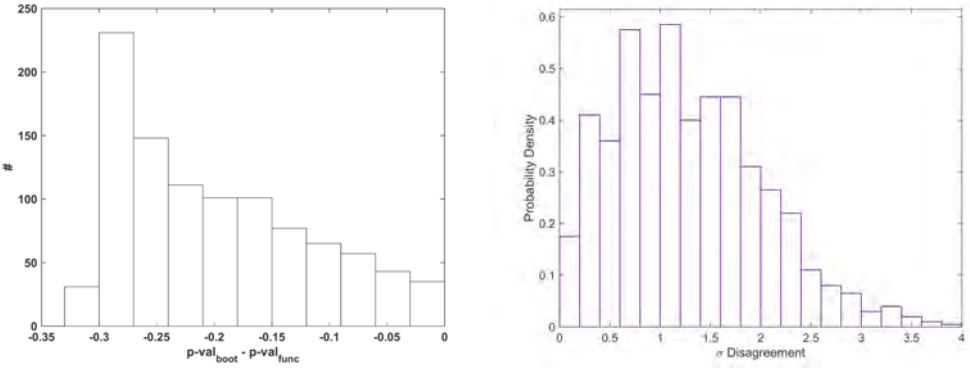

(a) (b)

Figure B.6: Distribution of the difference between the functional p-value calculation attempt with the bootstrap calculation and a distribution of the bootstrapped σ significance deviations reported by the L-test. These use 1000 sets of two Gaussians (σ = 45, $N1$ = 50, $N2$ = 500). (a) Histogram of the p-value difference between bootstrap and attempted functional form. (b) Distribution of L-test σ significance deviations.

REFERENCES

[1] A. M. Hillas, The origin of ultra-high-energy cosmic rays, Ann. Rev. Astron. Astrophys. 22 (1984) 425–444.
URL http://articles.adsabs.harvard.edu/full/1984ARA%26A..22..425H

[2] M. Ahlers, et al., Fermilab-fn-0847-a, YITP-SB-10-01.

[3] E. Fermi, On the origin of the cosmic radiation, Phys. Rev. 75 (1949) 1169–1174.
URL https://link.aps.org/doi/10.1103/PhysRev.75.1169

[4] L. O. Drury, An introduction to the theory of diffusive shock acceleration of energetic particles in tenuous plasmas, Rept. Prog. Phys. 46 (8) (1983) 973–1027.
URL http://stacks.iop.org/0034-4885/46/i=8/a=002

[5] A. Bonafede, et al., The Coma cluster magnetic field from Faraday rotation measures, Astron. Astrophys. 513 (2010) A30. arXiv:1002.0594.

[6] C. B. Finley, Anisotropy of arrival directions of ultrahigh energy cosmic rays, Ph.D. thesis, Columbia University (2006).
URL http://telescopearray.com/media/papers/finley_thesis.pdf

[7] P. G. Tinyakov, I. I. Tkachev, Deflections of cosmic rays in a random component of the galactic magnetic field, Astropart. Phys. 24 (2005) 32–43. arXiv:astro-ph/0411669.

[8] P. L. Biermann, et al., The supergalactic structure and the origin of the highest energy cosmic rays (astro-ph/9709250. MPI-FR-699) (1997) 9 p. arXiv:astro-ph/9709250.

[9] P. L. Biermann, et al., Cosmic structure of magnetic fields, in: Y. Giraud-Heraud, J. Tran Thanh van (Eds.), Very High Energy Phenomena in the Universe; Moriond Workshop, 1997, p. 227. arXiv:astro-ph/9709252.

[10] D. Ryu, et al., Cosmic magnetic fields in large scale filaments and sheets, Astron. Astrophys. 335 (1998) 19–25. arXiv:astro-ph/9803275.

[11] P. Blasi, et al., Cosmological magnetic fields limits in an inhomogeneous universe, Astrophys. J. 514 (1999) L79–L82. arXiv:astro-ph/9812487.

[12] K. Greisen, End to the cosmic ray spectrum?, Phys. Rev. Lett. 16 (17) (1966) 748–750. doi:10.1103/PhysRevLett.16.748.

[13] G. T. Zatsepin, V. A. Kuz'min, Upper limit of the spectrum of cosmic rays, JETP Lett. 4 (1966) 78.
URL http://adsabs.harvard.edu/abs/1966JETPL...4...78Z

[14] R. U. Abbasi, et al., First observation of the Greisen-Zatsepin-Kuzmin suppression, Phys. Rev. Lett. 100 (2008) 101101. arXiv:astro-ph/0703099.

[15] D. Allard, et al., Implications of the cosmic ray spectrum for the mass composition at the highest energies, JCAP 0810 (2008) 033. arXiv:0805.4779.

[16] J. Blümer, the Pierre Auger Collaboration, The northern site of the Pierre Auger Observatory, New J. Phys. 12 (3) (2010) 035001.
URL http://stacks.iop.org/1367-2630/12/i=3/a=035001

[17] R. Jansson, G. R. Farrar, A new model of the galactic magnetic field, Astrophys. J. 757 (1) (2012) 14.
URL http://stacks.iop.org/0004-637X/757/i=1/a=14

[18] D. J. Bird, et al., Study of broad scale anisotropy of cosmic ray arrival directions from 2×10^{17} eV to 10^{20} eV from Fly's Eye dataarXiv:astro-ph/9806096.

[19] R. M. Baltrusaitis, et al., Arrival directions of cosmic rays of E greater than 0.4 EeV, Astrophys. J. 303 (1986) 333–335.
URL http://adsabs.harvard.edu/full/1986ApJ...303..333B

[20] R. U. Abbasi, et al., Search for global dipole enhancements in the HiRes-I monocular data above $10^{18.5}$ eV, Astropart. Phys. 21 (2004) 111. arXiv:astro-ph/0309457.

[21] M. Aglietta, et al., Anisotropy studies around the galactic centre at EeV energies with the Auger Observatory, Astropart. Phys. 27 (2007) 244–253. arXiv:astro-ph/0607382.

[22] K. Kawata, et al., Search for the large-scale cosmic-ray anisotropy at 10^{18} eV with the Telescope Array surface detector, in: Proceedings, 33rd ICRC (ICRC2013): Rio de Janeiro, Brazil, July 2-9, 2013, p. 0311.
URL http://www.cbpf.br/~icrc2013/papers/icrc2013-0311.pdf

[23] R. U. Abbasi, et al., Search for cross-correlations of ultrahigh-energy cosmic rays with BL Lacertae objects, Astrophys. J. 636 (2006) 680–684. arXiv:astro-ph/0507120.

[24] A. Aab, et al., Searches for anisotropies in the arrival directions of the highest energy cosmic rays detected by the Pierre Auger Observatory, Astrophys. J. 804 (1) (2015) 15. arXiv:1411.6111.

[25] T. Abu-Zayyad, et al., Correlations of the arrival directions of ultra-high energy cosmic rays with extragalactic objects as observed by the Telescope Array experiment, Astrophys. J. 777 (2013) 88. arXiv:1306.5808.

[26] O. Taborda, Dipolar anisotropy of cosmic rays above 8 EeV, in: The Pierre Auger Observatory: Contributions to the 35th ICRC (ICRC 2017), 2017, pp. 26–30.
URL http://inspirehep.net/record/1618415/files/1617990_26-30.pdf

[27] R. U. Abbasi, et al., Indications of intermediate-scale anisotropy of cosmic rays with energy greater than 57 EeV in the northern sky measured with the surface detector of the Telescope Array experiment, Astrophys. J. 790 (2014) L21. arXiv:1404.5890.

[28] K. Kawata, Ultra-high-energy cosmic-ray hotspot observed with the Telescope Array surface detectors, in: Proceedings, 34th ICRC (ICRC2015): The Hague, The Netherlands, July 30 - August 6, 2015.
URL http://pos.sissa.it/archive/conferences/236/276/ICRC2015_276.pdf

[29] H.-N. He, et al., Monte Carlo Bayesian search for the plausible source of the Telescope Array hotspot, Phys. Rev. D93 (2016) 043011. arXiv:1411.5273.

[30] D. N. Pfeffer, et al., Ultrahigh-energy cosmic ray hotspots from tidal disruption events, Mon. Not. Roy. Astron. Soc. 466 (3) (2017) 2922–2926. arXiv:1512.04959.

[31] A. Aab, et al., The Pierre Auger Observatory: Contributions to the 35th ICRC (ICRC 2017), 2017. arXiv:1708.06592.

[32] P. Abreu, et al., Update on the correlation of the highest energy cosmic rays with nearby extragalactic matter, Astropart. Phys. 34 (2010) 314–326. arXiv:1009.1855.

[33] R. Abbasi, et al., The energy spectrum of cosmic rays above $10^{17.2}$ eV measured by the fluorescence detectors of the Telescope Array experiment in seven years, Astropart. Phys. 80 (2016) 131 – 140.
URL https://arxiv.org/abs/1511.07510

[34] R. U. Abbasi, et al., The hybrid energy spectrum of Telescope Array's Middle Drum detector and surface array, Astropart. Phys. 68 (2015) 27 – 44. arXiv:1410.3151.

[35] J. R. Hörandel, et al., The end of the galactic cosmic-ray energy spectrum - a phenomenological view, J. Phys. Conf. Ser. 47 (1) (2006) 132.
URL http://stacks.iop.org/1742-6596/47/i=1/a=017

[36] T. K. Gaisser, The cosmic-ray spectrum: from the knee to the ankle, J. Phys. Conf. Ser. 47 (1) (2006) 15.
URL http://stacks.iop.org/1742-6596/47/i=1/a=002

[37] G. Giacinti, et al., Transition from galactic to extragalactic cosmic rays and cosmic ray anisotropy, in: EPJ Web of Conferences, Vol. 53 of EPJ Web of Conferences, 2013, p. 06002.
URL http://inspirehep.net/record/1251246/files/epjconf_uhecr2012_06002.pdf

[38] R. U. Abbasi, et al., Study of ultra-high energy cosmic ray composition using Telescope Array's Middle Drum detector and surface array in hybrid mode, Astropart. Phys. 64 (2014) 49–62. arXiv:1408.1726.

[39] R. U. Abbasi, et al., Indications of proton-dominated cosmic-ray composition above 1.6 EeV, Phys. Rev. Lett. 104 (16).
URL http://prl.aps.org/abstract/PRL/v104/i16/e161101

[40] P. Abreu, et al., Interpretation of the depths of maximum of extensive air showers measured by the Pierre Auger Observatory, JCAP 1302 (2013) 026. arXiv:1301.6637.

[41] A. Aab, et al., Evidence for a mixed mass composition at the ankle in the cosmic-ray spectrum, Phys. Lett. B762 (2016) 288–295. arXiv:1609.08567.

[42] R. U. Abbasi, et al., Pierre Auger Observatory and Telescope Array: Joint contributions to the 34th ICRC (ICRC 2015)arXiv:1511.02103.

[43] W. F. Hanlon, The energy spectrum of ultra high energy cosmic rays measured by the High Resolution Fly's Eye observatory in stereoscopic mode, Ph.D. thesis, University of Utah.

[44] J. R. Horandel, Cosmic rays from the knee to the second knee: 10^{14} to 10^{18} eV, Mod. Phys. Lett. A22 (2007) 1533–1552, [,63(2006)]. arXiv:astro-ph/0611387.

[45] D. C. Rodriguez, The Telescope Array Middle Drum monocular energy spectrum and a search for coincident showers using High Resolution Fly's Eye HiRes-1 monocular data, Ph.D. thesis, University of Utah (2011).
URL http://www.cosmic-ray.org/thesis/rodriguez.html

[46] D. Heck, et al., CORSIKA: A Monte Carlo code to simulate extensive air showers, Forschungszentrum Karlsruhe FZKA 6019 (1998) 1–90.
URL https://web.ikp.kit.edu/corsika/physics_description/corsika_phys.pdf

[47] N. N. Kalmykov, et al., Quark-gluon string model and EAS simulation problems at ultra-high energies, Nucl. Phys. Proc. Suppl. 52 (1997) 17–28. doi:10.1016/S0920-5632(96)00846-8.

[48] E.-J. Ahn, et al., Cosmic ray interaction event generator SIBYLL 2.1, Phys. Rev. D80 (2009) 094003. arXiv:0906.4113.

[49] T. Pierog, K. Werner, Muon production in extended air shower simulations, Phys. Rev. Lett. 101 (2008) 171101. arXiv:astro-ph/0611311.

[50] G. Battistoni, et al., The hadronic models for cosmic ray physics: The FLUKA code solutions, Nucl. Phys. Proc. Suppl. 175 (2008) 88–95. arXiv:hep-ph/0612075.

[51] W. R. Nelson, et al., The EGS4 code system.
URL http://www.slac.stanford.edu/cgi-wrap/getdoc/slac-r-265.pdf

[52] B. T. Stokes, et al., Dethinning extensive air shower simulations, Astropart. Phys. 35 (2012) 759–766. arXiv:1104.3182.

[53] D. Ivanov, Energy spectrum measured by the Telescope Array surface detector, Ph.D. thesis, Rutgers, the State University of New Jersey (2012).
URL http://telescopearray.com/images/papers/theses/thesis_ivanov_rev2016.pdf

[54] T. Abu-Zayyad, et al., The surface detector array of the Telescope Array experiment, Nucl. Instrum. Meth. A689 (2013) 87–97. arXiv:1201.4964.

[55] M. Teshima, et al., Properties of 10^9 - 10^{10} GeV extensive air showers at core distances between 100 and 3000 m, J. Phys. G12 (1986) 1097. doi:10.1088/0305-4616/12/10/017.

[56] K. Shinozaki, M. Teshima, AGASA results, Nucl. Phys. B Proc. Suppl. 136 (2004) 18 – 27.
URL http://www.sciencedirect.com/science/article/pii/S0920563204004463

[57] M. G. Allen, Ultra high energy cosmic ray energy spectrum and composition using hybrid analysis with Telescope Array, Ph.D. thesis, University of Utah (2012).
URL http://telescopearray.com/media/theses/mallen_thesis.pdf

[58] National Aeronautics and Space Administration, National Oceanic and Atmospheric Administration, & Department of the Air Force, U.S. Standard Atmosphere, 1976.
URL https://ntrs.nasa.gov/archive/nasa/casi.ntrs.nasa.gov/19770009539.pdf

[59] J. P. Lundquist, Telescope Array Collaboration, Study of UHECR composition using Telescope Array's Middle Drum detector and surface array in hybrid mode, in: 34th ICRC (ICRC2015), Vol. 34 of ICRC, 2015, p. 441.
URL http://adsabs.harvard.edu/cgi-bin/nph-data_query?bibcode=2015ICRC...34..441L&link_type=ARTICLE&db_key=AST&high=

[60] National Centers for Environmental Prediction, NCEP GDAS satellite data 2004-continuing (2009).
URL http://rda.ucar.edu/datasets/ds735.0/

[61] J. Allison, et al., Geant4 developments and applications, IEEE Trans. Nucl. Sci. 53 (2006) 270.
URL https://cds.cern.ch/record/1035669/files/cer-002694037.pdf

[62] J. Linsley, L. Scarsi, Arrival times of air shower particles at large distances from the axis, Phys. Rev. 128 (1962) 2384–2392.
URL http://link.aps.org/doi/10.1103/PhysRev.128.2384

[63] T. Abu-Zayyad, et al., The cosmic-ray energy spectrum observed with the surface detector of the Telescope Array experiment, Astrophys. J. 768 (2013) L1. arXiv:1205.5067.

[64] R. U. Abbasi, et al., A northern sky survey for point-like sources of EeV neutral particles with the Telescope Array experiment, Astrophys. J. 804 (2) (2015) 133. arXiv:1407.6145.

[65] D. A. Vallado, Fundamentals of Astrodynamics and Applications, Springer-Verlag New York, 2007.
URL https://books.google.com/books?id=PJLlWzMBKjkC

[66] D. Newton, et al., The optimum distance at which to determine the size of a giant air shower, Astropart. Phys. 26 (2007) 414–419. arXiv:astro-ph/0608118.

[67] T. Z. AbuZayyad, The energy spectrum of ultra high energy cosmic rays, Ph.D. thesis, University of Utah (2000).
URL http://telescopearray.com/media/papers/tareq_thesis.pdf

[68] R. U. Abbasi, et al., Study of ultra-high energy cosmic ray composition using Telescope Arrays Middle Drum detector and surface array in hybrid mode, Astropart. Phys. 64 (2014) 49–62. arXiv:1408.1726.

[69] R. U. Abbasi, et al., A study of the composition of ultra-high energy cosmic rays using the High Resolution Fly's Eye, Astrophys. J. 622 (2) (2005) 910–926.
URL http://iopscience.iop.org/0004-637X/622/2/910/fulltext/

[70] G. C. Archbold, A study of the composition of ultra high energy cosmic rays using the High Resolution Fly's Eye, Ph.D. thesis, University of Utah (2002).
URL http://telescopearray.com/media/papers/archbold_thesis.pdf

[71] K. Kotera, A. V. Olinto, The astrophysics of ultrahigh energy cosmic rays, Ann. Rev. Astron. Astrophys. 49 (2011) 119–153. arXiv:1101.4256.

[72] M. Ajello, et al., The 60-month all-sky BAT survey of AGN and the anisotropy of nearby AGN, Astrophys. J. 749 (2012) 21. arXiv:1202.3137.

[73] G. Golup, Search for energy-position correlated multiplets in Pierre Auger Observatory data, in: Proceedings, 32nd ICRC (ICRC2011), 2011.
URL http://inspirehep.net/record/1352300/files/v2_0337.pdf

[74] N. Hayashida, et al., The anisotropy of cosmic ray arrival directions around 10^{18} ev, Astropart. Phys. 10 (1999) 303–311. arXiv:astro-ph/9807045.

[75] N. Hayashida, et al., The anisotropy of cosmic ray arrival direction around 10^{18} ev, in: Proceedings, 26th ICRC, Salt Lake City, August 17-25, 1999. arXiv:astro-ph/9906056.
URL http://krusty.physics.utah.edu/~icrc1999/root/vol3/o1_3_04.pdf

[76] T. P. Li, Y. Q. Ma, Analysis methods for results in gamma-ray astronomy, Astrophys. J. 272 (1983) 317–324.
URL http://adsabs.harvard.edu/full/1983ApJ...272..317L

[77] S. Gillessen, H. L. Harney, Significance in gamma-ray astronomy - the Li & Ma problem in Bayesian statistics, Astron. Astrophys. 430 (2005) 355. arXiv:astro-ph/0411660.

[78] D. Ivanov, G. B. Thomson, Search for intermediate-scale anisotropy by the HiRes experiment, ICRC 4 (2008) 445–448.
URL http://indico.nucleares.unam.mx/getFile.py/access?contribId=1044&sessionId=10&resId=0&materialId=paper&confId=4

[79] N. A. Teanby, An icosahedron-based method for even binning of globally distributed remote sensing data, Computers and Geosciences 32 (2006) 1442–1450.
URL http://www1.gly.bris.ac.uk/~teanby/software_nocol.html

[80] T. W. Anderson, On the distribution of the two-sample Crameŕ-von Mises criterion, Ann. Math. Stat. 33 (3) (1962) 1148–1159.
URL https://projecteuclid.org/download/pdf_1/euclid.aoms/1177704477

[81] J. T. Linnemann, Measures of significance in HEP and astrophysics, eConf C030908 (2003) MOBT001, [,35(2003)]. arXiv:physics/0312059.

[82] E. Parzen, On estimation of a probability density function and mode, Ann. Math. Statist. 33 (3) (1962) 1065–1076.
URL http://dx.doi.org/10.1214/aoms/1177704472

[83] P. Hall, et al., Kernel density estimation with spherical data, Biometrika 74 (4) (1987) 751–762.
URL http://dx.doi.org/10.1093/biomet/74.4.751

[84] R. Fisher, Dispersion on a sphere, Proc. Royal Soc. A 217 (1953) 295–305.
URL http://rspa.royalsocietypublishing.org/content/royprsa/217/1130/295.full.pdf

[85] C. Taylor, Automatic bandwidth selection for circular density estimation, CSDA 52 (7) (2008) 3493–3500.
URL http://eprints.whiterose.ac.uk/3793/

[86] E. García-Portugués, Exact risk improvement of bandwidth selectors for kernel density estimation with directional data, ArXiv e-printsarXiv:1306.0517.

[87] S. J. Sheather, Density estimation, Statist. Sci. 19 (4) (2004) 588–597.
URL http://dx.doi.org/10.1214/088342304000000297

[88] A. Agresti, B. A. Coull, Approximate is better than "exact" for interval estimation of binomial proportions, Am. Stat. 52 (2) (1998) 119–126.
URL http://www.stat.ufl.edu/~aa/articles/agresti_coull_1998.pdf

[89] A. Agresti, Score and pseudo-score confidence intervals for categorical data analysis, Stat. Biopharm. Res. 3 (2) (2011) 163–172.
URL http://www.stat.ufl.edu/~aa/articles/agresti_2011.pdf

[90] S. N. Zhang, D. Ramsden, Statistical data analysis for gamma-ray astronomy, Exp. Astron. 1 (1990) 145–163.
URL https://doi.org/10.1007/BF00462037

[91] S. Baker, R. D. Cousins, Clarification of the use of chi-square and likelihood functions in fits to histograms, Nucl. Instr. Meth. Phys. Res. 221 (2) (1984) 437–442. doi:https://doi.org/10.1016/0167-5087(84)90016-4.
URL http://www.sciencedirect.com/science/article/pii/0167508784900164

[92] K. A. Olive, et al., Review of particle physics, Chin. Phys. C38 (2014) 090001.
URL http://pdg.lbl.gov/2015/reviews/rpp2015-rev-statistics.pdf

[93] J. G. Heinrich, The log likelihood ratio of the Poisson distribution for small μ, CDF Note 5718 (2001).
URL www-cdf.fnal.gov/physics/statistics/notes/cdf5718_loglikeratv2.ps.gz

[94] S. Csorgo, J. J. Faraway, The exact and asymptotic distributions of Crameŕ-von Mises statistics, J. Royal Stat. Soc. B 58 (1) (1996) 221–234.
URL http://www.jstor.org/stable/2346175

[95] Pierre Auger Collaboration, et al., Search for signatures of magnetically-induced alignment in the arrival directions measured by the Pierre Auger Observatory, Astropart. Phys. 35 (2012) 354–361. arXiv:1111.2472.

[96] A. Aab, et al., Search for patterns by combining cosmic-ray energy and arrival directions at the Pierre Auger Observatory, EPJ C 75 (2015) 269. arXiv:1410.0515.

[97] H. P. Bretz, Search for anisotropy in cosmic ray arrival directions using a boosted decision tree discriminator with the Pierre Auger Observatory, Ph.D. thesis,

Rheinisch-Westphalian Technical University of Aachen (2011).
URL http://wwwo.physik.rwth-aachen.de/fileadmin/user_upload/www_physik/Personen/erdmann/Diplomathesis-Bretz.pdf

[98] G. Golup, et al., Source position reconstruction and constraints on the galactic magnetic field from ultra-high energy cosmic rays, Astropart. Phys. 32 (2009) 269–277. arXiv:0902.1742.

[99] M. Zimbres, et al., Using spherical wavelets to search for magnetically-induced alignment in the arrival directions of ultra-high energy cosmic rays, Astropart. Phys. 54 (2014) 54–60. arXiv:1305.0523.

[100] W. S. Burgett, M. R. O'Malley, Hints of energy dependences in AGASA UHECR arrival directions, Phys. Rev. D67 (2003) 092002. arXiv:hep-ph/0301001.

[101] M. G. Kendall, The treatment of ties in ranking problems, Biometrika 33 (3) (1945) 239–251.
URL http://biomet.oxfordjournals.org/content/33/3/239.full.pdf+html

[102] C. Croux, C. Dehon, Influence functions of the Spearman and Kendall correlation measures, SMA 19 (4) (2010) 497–515.
URL https://feb.kuleuven.be/public/ndbae06/PDF-FILES/IFKendall-Spearman.pdf

[103] K. L. Li, et al., A double-correlation tremor-location method, Geophys. J. Int 208 (2017) 1231–1236. arXiv:1609.07314.

[104] T. K. Gaisser, A. M. Hillas, Reliability of the method of constant intensity cuts for reconstructing the average development of vertical showers, ICRC 8 (1977) 353–357.
URL http://articles.adsabs.harvard.edu/full/1977ICRC....8..353G

[105] D. R. Cox, The regression analysis of binary sequences, J. Royal Stat. Soc. B 20 (2) (1958) 215–242.
URL http://www.jstor.org/stable/2983890

[106] D. Collett, Modelling Binary Data, Second Edition, Chapman & Hall/CRC Texts in Statistical Science, Taylor & Francis, 2002.
URL https://books.google.com/books?id=LMRAIBEbdqsC

[107] A. Strandlie, R. Frühwirth, Track and vertex reconstruction: From classical to adaptive methods, Rev. Mod. Phys. 82 (2010) 1419–1458.
URL http://link.aps.org/doi/10.1103/RevModPhys.82.1419

[108] I. Guyon, et al., Feature Extraction: Foundations and Applications, Studies in Fuzziness and Soft Computing, Springer Berlin Heidelberg, 2006.
URL http://www.springer.com/us/book/9783540354871

[109] P. W. Holland, R. E. Welsch, Robust regression using iteratively reweighted least-squares, Commun. Stat. Theory Methods 6 (9) (1977) 813–827.
URL http://dx.doi.org/10.1080/03610927708827533

[110] T. Abu-Zayyad, et al., The energy spectrum of ultra-high-energy cosmic rays measured by the Telescope Array FADC fluorescence detectors in monocular mode, Astropart. Phys. 48 (0) (2013) 16–24.
URL https://arxiv.org/abs/1305.6079

[111] J. Abraham, et al., Observation of the suppression of the flux of cosmic rays above 4×10^{19} eV, Phys. Rev. Lett. 101 (2008) 061101. arXiv:0806.4302.

[112] P. Abreu, et al., Measurement of the proton-air cross section at s=57 TeV with the Pierre Auger Observatory, Phys. Rev. Lett. 109 (2012) 062002.
URL http://link.aps.org/doi/10.1103/PhysRevLett.109.062002

[113] M. A. Stephens, EDF statistics for goodness of fit and some comparisons, J. Am. Stat. Assoc 69 (347) (1974) 730–737.
URL http://www.jstor.org/stable/2286009

[114] R. U. Abbasi, G. B. Thomson, $<x_{max}>$ uncertainty from extrapolation of cosmic ray air shower parametersarXiv:1605.05241.

[115] R. Ulrich, et al., Hadronic multiparticle production at ultra-high energies and extensive air showers, Phys. Rev. D83 (2011) 054026. arXiv:1010.4310.

[116] R. D. Parsons, et al., Systematic uncertainties in air shower measurements from high-energy hadronic interaction models, Astropart. Phys. 34 (2011) 832–839. arXiv:1102.4603.

[117] R. G. O'Brien, A general ANOVA method for robust tests of additive models for variances, J. Am. Stat. Assoc 74 (368) (1979) 877–880.
URL http://www.jstor.org/stable/2286416

[118] R. G. O'Brien, A simple test for variance effects in experimental designs, Psychol. Bull. 89 (3) (1981) 570–574.
URL http://psycnet.apa.org/record/1981-20271-001

[119] S. Ostapchenko, Non-linear screening effects in high energy hadronic interactions, Phys. Rev. D74 (2006) 014026. arXiv:hep-ph/0505259.

[120] K. Dolag, et al., Magnetic field in the local universe and the propagation of UHECRs, J. Korean Astron. Soc. 37 (5) (2004) 427–431.
URL http://sirius.unist.ac.kr/kaw3/00_PDF_kaw3/v37n5p427_dolag.pdf

[121] P. G. Tinyakov, I. I. Tkachev, Tracing protons through the galactic magnetic field: A clue for charge composition of ultrahigh-energy cosmic rays, Astropart. Phys. 18 (2002) 165–172. arXiv:astro-ph/0111305.

[122] H. Takami, et al., Propagation of ultra-high-energy cosmic ray nuclei in cosmic magnetic fields and implications for anisotropy measurements, Astropart. Phys. 35 (2012) 767–780. arXiv:1202.2874.

[123] H. Sagawa, The plan of the Telescope Array experiment for the next five years, in: Proceedings, 33rd ICRC (ICRC2013): Rio de Janeiro, Brazil, July 2-9, 2013, p. 0121.
URL http://www.cbpf.br/~icrc2013/papers/icrc2013-0121.pdf

[124] J. Heinrich, Pitfalls of goodness-of-fit from likelihood, in: L. Lyons, et al. (Eds.), Statistical Problems in Particle Physics, Astrophysics, and Cosmology, 2003, p. 52. arXiv:physics/0310167.

[125] R. Cousins, Generalization of chi-square goodness-of-fit test for binned data using saturated models, with application to histograms.
URL http://www.physics.ucla.edu/~cousins/stats/cousins_saturated.pdf

[126] J. G. Heinrich, Can the likelihood-function value be used to measure goodness of fit?, CDF Note 5639 (2001).
URL https://www-cdf.fnal.gov/physics/statistics/notes/cdf5639_goodnessoffitv2.ps.gz

[127] F. J. Massey Jr., The Kolmogorov-Smirnov test for goodness of fit, J. Am. Stat. Assoc 46 (253) (1951) 68–78.
URL https://r-forge.r-project.org/scm/viewvc.php/*checkout*/pkg/literature/1951-jamsta-massey-kolmsmirntest.pdf?root=glogis

[128] A. N. Pettitt, A two-sample Anderson-Darling rank statistic, Biometrika 63 (1) (1976) 161.
URL http://www.jstor.org/stable/2335097

[129] S. S. Wilks, The large-sample distribution of the likelihood ratio for testing composite hypotheses, Ann. Math. Statist. 9 (1) (1938) 60–62.
URL http://dx.doi.org/10.1214/aoms/1177732360

[130] G. E. Forsythe, et al., Computer Methods for Mathematical Computations, Prentice Hall Professional Technical Reference, 1977.

[131] J. C. Lagarias, et al., Convergence properties of the Nelder-Mead simplex method in low dimensions, SIOPT 9 (1998) 112–147.
URL http://citeseerx.ist.psu.edu/viewdoc/download?doi=10.1.1.120.6062&rep=rep1&type=pdf